Design Optimization of Contra-rotating Axial Flow Pump with Rotational Speed Control for Effective Energy Saving

張, 徳

出版情報：Kyushu University, 2020, 博士（工学）, 課程博士
バージョン：
権利関係：

Design Optimization of Contra-rotating Axial Flow Pump with Rotational Speed Control for Effective Energy Saving

Supervisor: Professor Satoshi Watanabe

De Zhang
Mechanical Engineering
Graduate School of Engineering
Kyushu University

January 2021

Table of contents

Chapter 1

Introduction

The pump is one type of machines with rotating rotors, which is often used to deliver or pressurize liquids. Pumps have been widely applied for various purposes in our daily life as well as in various industrial fields. According to Turbomachinery Society of Japan [1], some applications of pumps have been summarized in Fig. 1-1. As we can see, pumps have been employed for many purposes: transferring clean water to homes for drinking, pressurizing the propellant for space rockets, moving liquified natural gas (LNG), delivering cold water to condense the steam in a power plant, and so on.

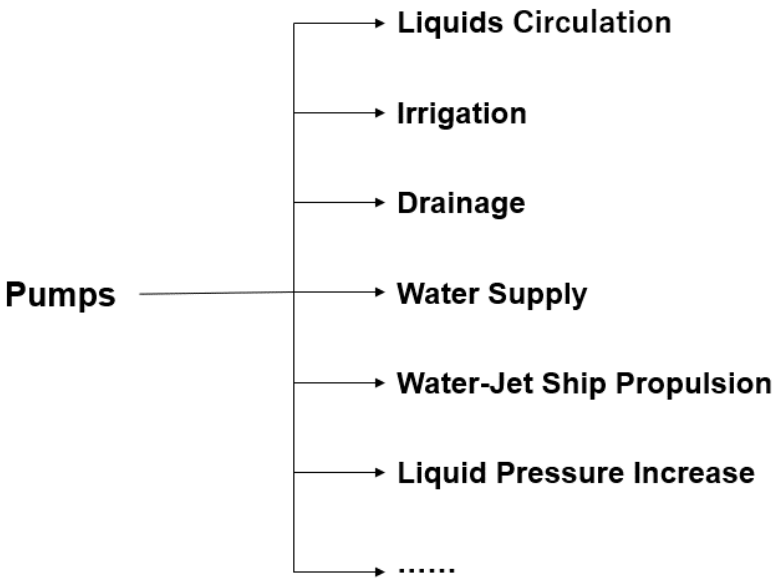

Fig. 1-1 Some applications of pumps (according to Turbomachinery Society of Japan [1])

Besides of wide applications of pumps, they also consume considerable amount of electricity in the world. De Almeida et al. [2] reported that about 14.5% of the total electricity in European

Union (EU) was used for the pumps in industrials. In Japan, the pumps consumed about 10% of the total electricity in 2005 [3]. Frenning et al. [4] also reported that nearly 20% of the electricity in the world is consumed by pumping systems. In addition, it should be noted that about 60% of the total world electricity was generated still through burning the fossil fuels in 2017 [5], which can generate lots of greenhouse gases. Therefore, it is essential and significant to improve the energy-saving performance of pumps to relieve the greenhouse effect.

1.1 Pumps

There are many types of pumps designed for various purposes in the applications. According to the flow path direction at the rotor outlet (discharge side), pumps can be mainly classified into three types: centrifugal pump, mixed flow pump and axial flow pump. A cross-sectional view of generalized pump rotor is illustrated in Fig. 1-2. The shaft axis in Fig. 1-2 represents the shaft of the rotating rotor, subscripts 1 and 2 represent parameters at the rotor's inlet and exit respectively, radii of blade tip and hub are denoted by R_T and R_H respectively, B is the height of the rotor blade, and ϑ denotes the angle between the exit flow passage and rotating axis. ϑ will be near $90°$ in centrifugal pumps and about $0°$ in axial flow pumps. The ϑ in mixed flow pumps would be like the case of $0° < \vartheta < 90°$.

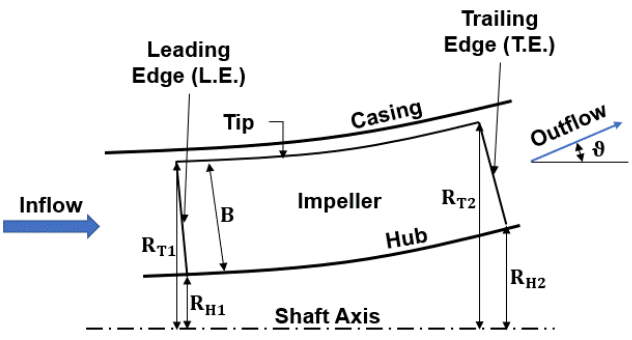

Fig. 1-2 Sketch of a pump rotor (reproduced from Brennen, C. E. [6])

In the design process of pumps, there is an important nondimensional parameter consisting of the pre-known parameters: shaft angular rotating speed ω (in rad/s), design flow rate Q_d (in m^3/s), gravity g (in m/s^2) and design head H_d (in m). Then, the nondimensional parameter called specific speed N_D can be written as:

$$N_D = \frac{\omega\sqrt{Q_d}}{(gH_d)^{3/4}} \tag{1-1}$$

The nondimensional value of specific speed in most common pumps locates in the range from 0.1 to 4.0 [6][7]. With decades' development, good designs of rotor shape can be summarized against the specific speeds; in terms of efficiency, axial flow pumps are much better for higher specific speeds (large flow rate, low head), centrifugal pumps are more efficient in the range of lower specific speeds (small flow rate, high head), and mixed flow pumps are more suitable for medium specific speeds.

Even though Eq. (1-1) is a nondimensional parameter, most countries usually calculate the specific speed with inconsistent units in industrial applications. In Japan, the dimensional specific speed N_S is determined with rotor rotating speed N (in rpm), design flow rate Q_d (in $\mathrm{m}^3/\mathrm{min}$) and design head H_d (in m):

$$N_S = \frac{N\sqrt{Q_d}}{{H_d}^{3/4}}\ [\mathrm{rpm}, \mathrm{m}^3/\mathrm{min}, \mathrm{m}] \tag{1-2}$$

The above dimensional specific speed N_S will be used in the following chapters in the present thesis.

1.2 Some problems in the design and operation of pumps

As mentioned before, the electricity consumption of worldwide pumps cannot be ignored, which has significant impact on the greenhouse gas emission. Therefore, it is essential and

important to further improve performance of pumps. The following three parts will introduce some problems in the process of the pump performance improvement.

1.2.1 Cavitation

Cavitation is one of the most unfavorable phenomena in the operation of pumps, in which vapor bubbles occur in the low-pressure regions in the liquid flow. The cavitation would cause many serious problems such as performance deterioration, erosion, noise and vibration [8][9][10].

The most fundamental non-dimensional parameter to describe the cavitation is the cavitation number σ. It is defined by:

$$\sigma = (p_1 - p_v)/\frac{1}{2}\rho U^2 \tag{1-3}$$

where p_1 means the static pressure at inlet, p_v denotes the vapor pressure, ρ is the density of flow, and U represents the reference velocity which is usually taken as the inlet blade tip velocity in rotating machines $U = R_{T1}\omega$.

Additional two nondimensional parameters are usually used to describe the performance of pump, and they are head coefficient ψ and flow coefficient at rotor outlet ϕ_2:

$$\psi = gH/(R_{T1}\omega)^2 \tag{1-4}$$

$$\phi_2 = Q/A_2 R_{T2}\omega \tag{1-5}$$

where H is the total pressure rise between inlet and outlet of the rotor, Q denotes the volumetric flow rate, R_{T2} means the exit tip radius, and A_2 means the area at rotor outlet.

In Fig. 1-3, a typical image of cavitation performance (ψ vs σ) of pumps is illustrated. As we can see, with the reduction of cavitation number, the head of pump could be also gradually decreased. When the cavitation number reaches a small enough value, the head of pump could breakdown, which is very unfavorable.

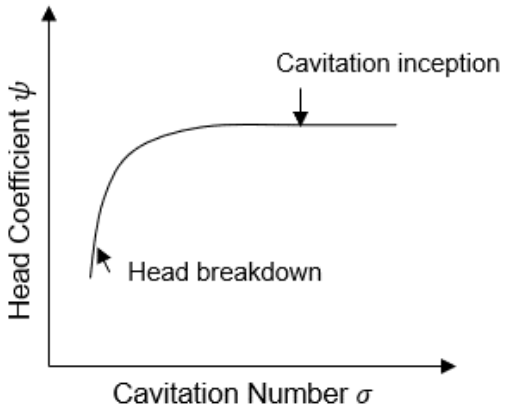

Fig. 1-3 Typical head breakdown curve of pumps caused by cavitation

Severe cavitation in pumps often causes the serious damage of impeller [11]. Such damage may result from the impeller fatigue failure, and this is costly and dangerous in the operation of pumps. Moreover, deep cavitation is known to also cause the cavitation instabilities such as rotating cavitation and cavitation surge. As an example, Morii.et al. [12] have presented cavitation surge phenomenon in an inducer inducing the huge amplitude of fluctuation with low frequency, which may cause the severe vibration and noise in the pumping system.

1.2.2 Off-design performance and loss quantification

Most pumps can achieve good performance at the design point. However, the performance of them could also be rapidly decreased at the off-design conditions. Especially, the positive slope of head performance curve plotted against the flow rate, which is often observed at partial flow rates, is known to be the cause of the flow instabilities such as surge and rotating stall. Since the pumps are operated in a wide flow range sometimes from the deep partial to the over flow rates, the positive slope of head performance curve should be avoided. Since the positive slope is considered to be caused by the sudden increase of the loss, it should be important to clarify the loss generation mechanism in the pumps to improve the deteriorated off-design performance.

The entropy generation is believed to be helpful to understand losses in turbomachines [13]. With the development of computational fluid dynamics (CFD), the flows in various turbomachines have been well predicted in more details and accurately [14][15]. Recently, Kock and Herwig [16] proposed a loss evaluation method for incompressible fluid based on the local entropy production rate, which can be easily applied for the RANS (Reynolds-Averaged Navier-Stokes simulation) in most CFD codes. Schmandt et al. [17] have well visualized the loss by using such method. This method has also been well applied to localize the losses in many hydro turbomachines [18][19]. However, it is also reported that quantitative balance of powers could not be achieved with the method of entropy production rate [18][20]. The quantitative error seems to come from the near-wall treatment of two equations turbulence model as pointed out in [16], and Hou et al. [21] and Li et al. [22] recently considered the entropy production in the near-wall region by the viscous work using wall shear stress, which worked well for the improvement of loss evaluation.

On the other hand, it is known that the rothalpy is kept constant along a relative streamline in adiabatic steady flows [23]. In incompressible flow, the rothalpy I can be written as:

$$I = e + \frac{p}{\rho} + \frac{1}{2}[W^2 - (r\omega)^2] \tag{1-6}$$

where e, p, ρ, W, r and ω denote the specific internal energy, the static pressure, the flow density, the relative velocity, the radius from the rotating axis and the angular rotational speed respectively.

The change of rothalpy along the flow stream has been used to identify the locations of losses in a fluid coupling [24] and torque converter [25]. However, the quantities of local losses are still not available to be predicted. The change rate of rothalpy, that is the material-derivative of rothalpy, in turbomachine aerodynamics has been firstly introduced by Sehra et al. [26]. The findings of Lyman [27] indicate the relation between the change rate of rothalpy without internal energy and the local entropy generation rate for incompressible steady adiabatic flow in

turbomachinery with constant rotor rotational speed. Therefore, the change rate of rothalpy without considering internal energy is also possible to be used to analyze the local flow losses for hydraulic fluid machinery in CFD simulations.

1.2.3 Cost of energy and labor

In the life cycle of a pump, energy consumption is usually the dominant cost [4]. Most pumps have to be operated at both of design and off-design flow rates. Niigata Agricultural Land Department reported that a pumping station in Niigata was usually operated at flow rates from $100\mathrm{m}^3/\mathrm{h}$ to $2200\mathrm{m}^3/\mathrm{h}$ [28], which is very broad. However, the performance of most pumps would deteriorate significantly at off-design flow rates, which usually means much more electricity consumption. One possible solution is to control the rotating speed of rotor to optimize the pump performance at off-design flow rates [29], in which the deteriorated performance can be enhanced with the rotational speed control (RSC). As a result, the RSC method could well reduce the energy consumption of pumps in the off-design conditions.

It should be also noted that the operation of the pump is costly in labor. Furthermore, most countries in the world are facing the aging problem and the pace of aging is getting faster in more developed countries, which indicates the lack of labor in the future. Wan et al. [30] predicted that the percentage of population over 65 years old in most developed countries will be over 20% in 2050. On the other hand, the rotational speed control (RSC) can usually be constructed in an unmanned automatic system, which could also reduce the cost of labor.

1.3 Contra-rotating axial flow pump

Recently, compact pumps with higher rotating speed are demanded for economical and environmental reasons [31]. In addition, in many industrial fields, the pumps are required to be

operated in the wide flow rate range from the very partial to the over flow rates, which requires the pumps to have a stable head performance curve without positive slope. However, pumps with higher rotational speed usually suffers from the unfavorable cavitation. One possible solution to relieve the cavitation problem is to employ counter-rotating rotors distributing the blade loading to the two rotors. The counter-rotating rotors have been applied in various types of turbopumps [32][33]. Moreover, because of the flexibilities of combination of rotating speeds of the two rotors, the head performance curves may be further improved by the rotational speed control.

1.3.1 Axial flow pump

As introduced before, axial flow pump is more efficient for higher specific speeds, which is more appropriate for the conditions with large flow rates and low head rise. Therefore, axial flow pumps play important roles in drainage and irrigation for agriculture, civil and industrials worldwide. In China, a total amount of about $14.8km^3$ water is diverted from the south to the north in the eastern route of South-to-North water diversion project every year. Such large amount of water is totally raised to about 40 meters through 13 pumping stations [34], where most of pumps are axial flow pumps [35]. Many types of axial flow pumps have also been employed in drainage pumping stations to keep rivers in Niigata from overflow caused by the Guerrilla rainstorm [28].

1.3.2 Improvement of performance of axial flow pump by contra-rotating rotors

Furukawa et al. [36] have successfully achieved better cavitation performance and compact size by applying contra-rotating rotors in an axial flow pump with high specific speed. Furthermore, Cao et al. [37][38] have improved the performance of contra-rotating axial flow pump with a different speed design method. As displayed in Fig. 1-4, compared with the previous

design (RR2) [39], the contra-rotating axial flow pump with different speed design (RR3) shows higher efficiency and more sufficient head near the design flow rate.

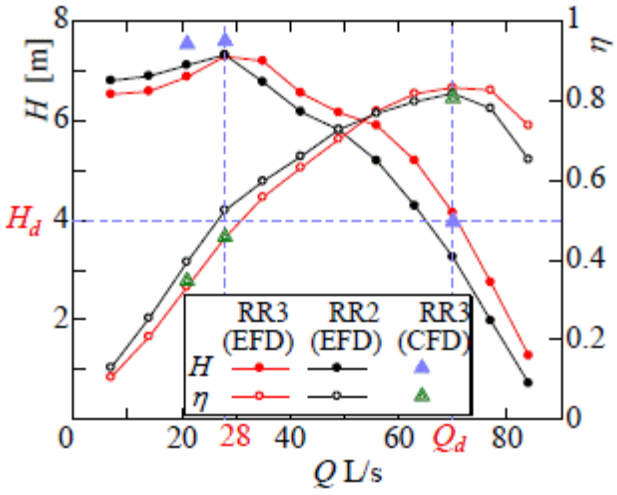

Fig. 1-4 Improvement of pump performance curve by applying counter-rotating rotors designed with different speeds of front and rear rotors (RR3) [38]

1.3.3 Rotational speed control (RSC) of contra-rotating axial flow pump

Most pumps suffer from significantly deteriorated performance at off-design flow rates, and the performance of the contra-rotating axial flow pump is also decreased considerably under the off-design conditions (shown in Fig. 1-4). In order to enhance the performance at off-design flow rates, rotational speed control (RSC) has been applied for the front and rear rotors of contra-rotating axial flow pump in experiments [40]. Figure 1-5 (a) shows the rotational speed information of front and rear rotors. Red symbols at higher flow rates mean that only the rear rotor rotational speed is modified with keeping front rotor rotating speed constant, while blue symbols at lower flow rates indicate that only the rotational speed of front rotor is controlled with constant rear rotor speed. We can see the efficiency improvement at off-design conditions with

the RSC in Fig. 1-5 (b) and (c), where black symbols show the performance of a contra-rotating axial flow pump without RSC.

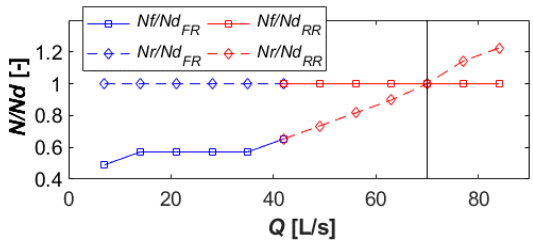

(a) Rotational speed information of RSC

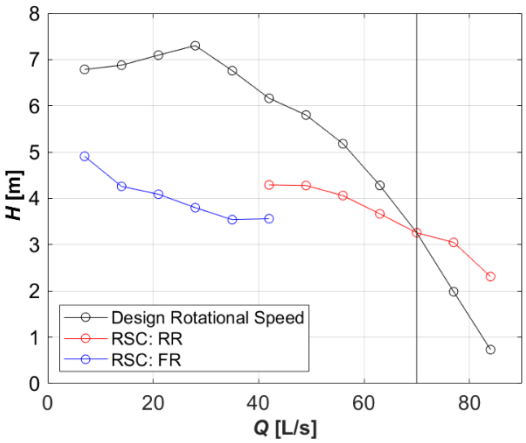

(b) Head curves

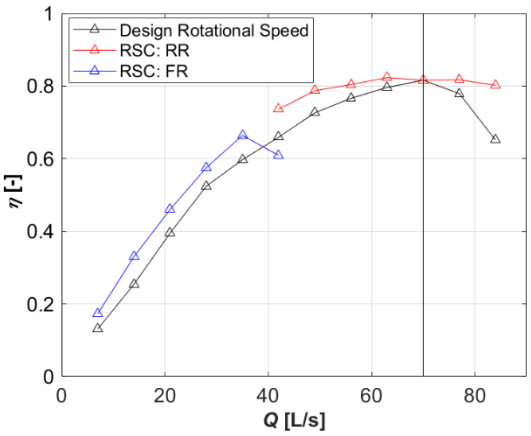

(c) Efficiency curves

Fig. 1-5 Performances of a contra-rotating axial flow pump for RR2 rotors with rotational speed control (according to experimental data from Momosaki et al. [40])

However, to maximize the advantage of RSC in contra-rotating pumps, that may be realized by a simultaneous RSC of front and rear rotors, thorough investigations are necessary to find a good simultaneous control method for both of front and rear rotors. Since it could consume unaffordable time to conduct experiments or CFD simulations, a performance prediction model toward RSC in contra-rotating axial flow pump is significantly important.

1.4 Performance prediction model for RSC in contra-rotating axial flow pump

As mentioned above, a performance prediction model is significantly essential in the automatic rotational speed control (RSC) of front and rear rotors in contra-rotating axial flow pump, which could be very helpful in quick determination of optimum rotational speeds at various flow rates.

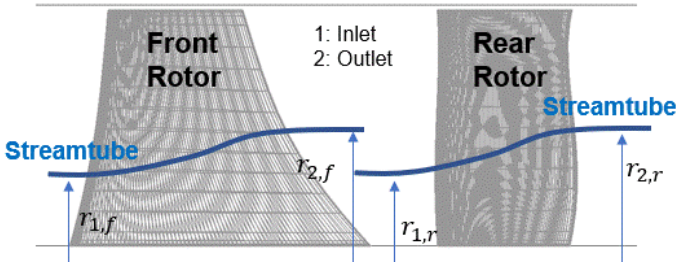

Fig. 1-6 Streamtubes assumed in contra-rotating axial flow rotors

In order to calculate the flow velocities in the contra-rotating axial flow rotors (shown in Fig. 1-6), steady, axisymmetric, non-reverse and non-viscous flows in the rotors may be assumed for simplicity. Therefore, the rothalpy I (Eq. 1-6) should be constant along a streamtube (blue lines in Fig. 1-6). Since the radial equilibrium condition is also well used at the inlet and outlet of rotor in the design of axial flow pump [6], it would be possible to determine the flow velocities and theoretical head by considering the above assumed conditions, mass conservation equation and empirical deviation angle equation [41].

Furthermore, the empirical cascade loss equation [42] is also helpful in the performance evaluation of axial flow turbomachines. Besides the cascade loss, the loss due to tip clearance effect is also very significant [43], which may be modelled on the basis of blade tip lift coefficient. In principle, the above calculations are applicable for contra-rotating axial flow pumps and seem to be useful to determine the pump performance in a very simple way.

1.5 Design optimization of rotors for energy saving

Through the above investigations, it is known that the contra-rotating axial flow pump could achieve better performance at off-design flow rates using rotational speed control (RSC) of front and rear rotors. However, the rotors (especially the rear rotor) are generally designed to satisfy the design requirements and cavitation performance only at the design flow rate. It is not clear whether the rotors are the best shape for energy saving under different operation conditions. Therefore, a design optimization of the rotors would be necessary to be conducted with considering the energy-saving performance at both of design and off-design flow rates with rotational speed control (RSC).

1.5.1 Design optimization methods

The objective of the optimization is to find the design to consume the least energy at design flow rate as well as at various off-design flow rates with RSC. Since there is no sufficient experience in designing front and rear rotors of contra-rotating axial flow pump to reach such an objective, it should be very difficult to directly design the best rotors. Therefore, in the present thesis, a design optimization method will be employed to help us solve the problem.

There are two main types of optimization methods: gradient-based methods and stochastic methods. Compared with the gradient-based methods, stochastic methods are able to capture the global optimization. Therefore, various stochastic optimization algorithms have been applied in the design of pumps. Oyama et al. [44] have used evolutionary algorithm (EA) to achieve better performance of a rocket engine pump. Wahba et al. [45] obtained satisfactory designs of centrifugal pump impellers by employing a genetic algorithm (GA). Better design of a centrifugal pump has also been achieved by using particle swarm optimization (PSO) algorithm [46]. Among these optimization methods, GA is very popular in the design optimization of turbomachinery

because of its robustness in global optimization [47]. For this reason, a genetic algorithm (GA) is employed in the present thesis to conduct design optimization of rotors in contra-rotating axial flow pump.

According to Li et al. [47], a brief flowchart of design optimization in turbomachinery is plotted in Fig. 1-7 (a). As we can see, the approximation model (metamodel) is employed to approximate the CFD based performances and then predict reasonable performances, which can considerably reduce the computational cost of the optimization [48][49]. However, as illustrated in Fig. 1-7 (b), there can exist two optimization processes in the design optimization for RSC in contra-rotating axial flow pump: one is the optimization in shapes of rotors (Loop 1); the other one is the optimization in operational rotational speed of rotors at various flow rates (Loop 2). This indicates that, besides of the rotor shape parameters, three more parameters (flow rates, rotational speeds of front and rear rotors) should also be included to construct the approximation models. It could be very difficult to establish an appropriate model using CFD simulations, whose accuracy may not be good enough at off-design flow rates with off-design rotational speeds. Moreover, the approximation model (metamodel) need to be trained with computationally expensive database, whose size is depending on the number of design parameters. Mostly, the more the design parameters are, the larger the database is. Therefore, a performance prediction model is still necessary in the design optimization for energy saving with RSC of contra-rotating axial flow pump.

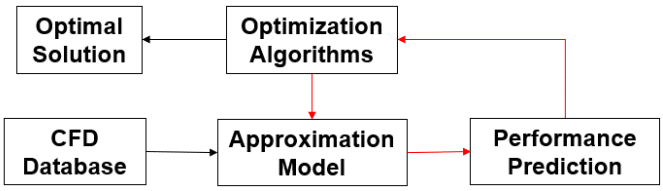

(a) Design optimization flow in turbomachines

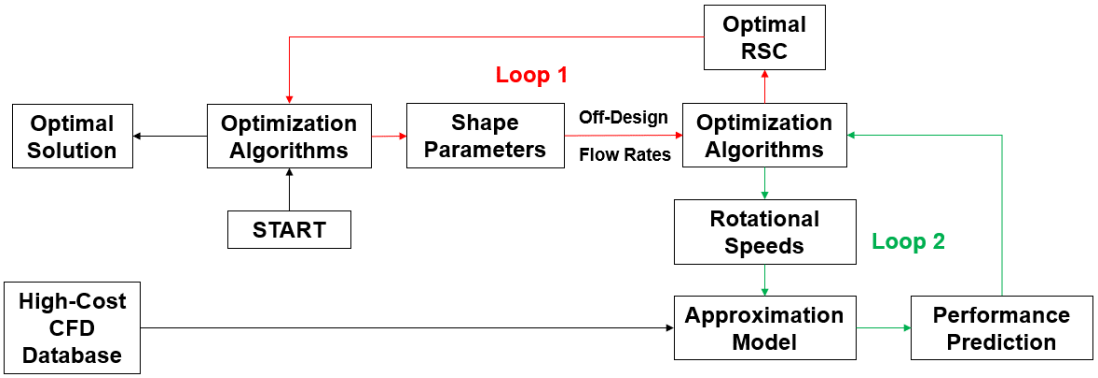

(b) A framework of design optimization for RSC in contra-rotating axial flow pump

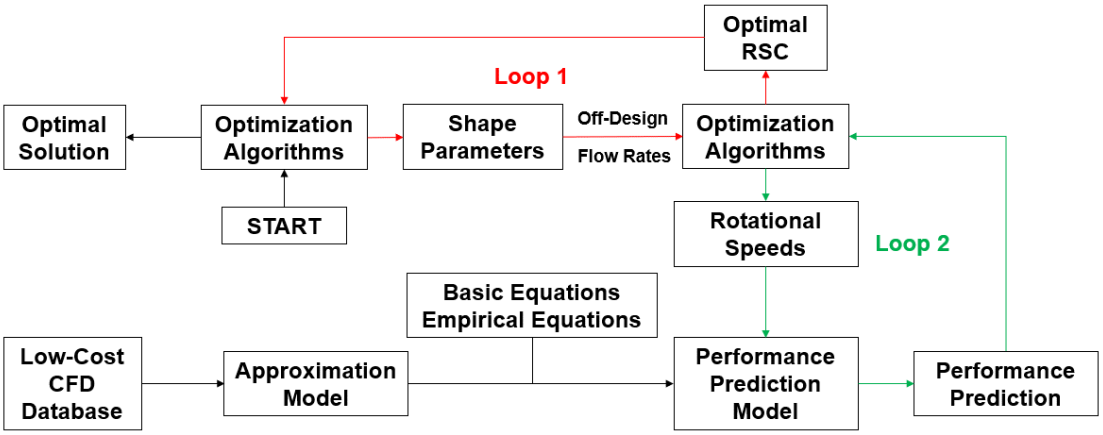

(c) A flowchart of design optimization for RSC in contra-rotating axial flow pump using a performance prediction model

Fig. 1-7 Frameworks of optimizations

1.5.2 Performance prediction model with a low-cost metamodel

In the construction of performance prediction model for rotational speed control in contra-rotating axial flow pump (introduced in Sec. 1.4), it is understood that the performance prediction

model agrees well with the CFD simulations (indicated in Chapter 3). It is also found that some empirical equations (other loss prediction and theoretical head modification) in the performance prediction model could be established with CFD simulations at near-design flow rates with design rotating speed. Then it is expected to well predict the performances using the above empirical equations at various flow rates with various rotating speed.

Therefore, it seems possible to establish a database only using CFD results at some near-design flow rates with the design rotating speed, which can achieve more convincible CFD simulations and lower computational cost of the database for metamodel. Such advantage of metamodel in the computational cost could be more significant when considering design parameters for both of front and rear rotors in contra-rotating axial flow pump. Through the construction of empirical equations, and combining with the rothalpy conservation equation, mass conservation equation, radial equilibrium assumption, empirical deviation angle, and empirical cascade loss, the performance could be evaluated for various design parameters of rotors in contra-rotating axial flow pump at different flow rates with varied rotational speed. Figure 1-7 (c) displays a possible framework of design optimization for energy saving with RSC in contra-rotating axial flow pump.

1.6 Objective and outline of the present thesis

1.6.1 Objective of the present study

The main objective in this study is to design a contra-rotating axial flow pump with better energy saving performance. In order to reach this objective, the following issues are investigated:

(a) To understand the loss generation mechanism in rear rotor of contra-rotating axial flow pump by the appropriate method for the evaluation of the location and quantity of losses;

(b) To construct a performance prediction model toward rotational speed control (RSC) in contra-rotating axial flow pump and to apply the proposed model for energy saving

operations;

(c) To conduct design optimization of rotors in contra-rotating axial flow pump with a performance prediction model and a genetic algorithm (GA) to obtain the best energy-saving solution with rotational speed control (RSC).

1.6.2 Outline of the present thesis

The present thesis consists of totally five chapters. Chapter 1 is to introduce the background and objective of the present research. The following three chapters are to describe the solutions and results of the above three issues (a)~(c).

In Chapter 2, two loss evaluation methods based on the entropy generation rate and the material-derivative of rothalpy will be firstly introduced. Then, according to the prediction results of loss quantity in CFD simulations of three different rear rotors for contra-rotating axial flow pump, an appropriate loss evaluation method will be determined. Finally, more detailed loss distributions and flow structures will be carefully compared to discuss the loss generation mechanism in the three designs of rear rotors.

In Chapter 3, a fast and effective performance prediction model will be established by considering radial equilibrium condition, conservation of mass and rothalpy, empirical deviation angle, blade-rows interaction and empirical losses. Then, CFD based simulations are also conducted to validate the proposed performance prediction model. Finally, the proposed model will be applied in practical problems on energy-saving operations.

In Chapter 4, the performance prediction models including an approximation model will be firstly described for two conditions: optimization of only rear rotor and optimization of both front and rear rotors. Simulations of CFD will also be carried out to help establish and validate the performance prediction models. A genetic algorithm method (GA) will also be introduced. Then,

design optimizations will be separately conducted in two cases; one is for the only rear rotor using the same front rotor, and another is for the both of front and rear rotors, which are made using the proposed models and the GA. Finally, discussions will be given to the original and optimal designs toward energy savings with rotational speed control in contra-rotating axial flow pump.

Chapter 5 is the conclusions of the present thesis.

Chapter 2

Loss mechanism in rear rotor of contra-rotating axial flow pump

Good design of rotors could be achieved if we can understand the location and quantity of losses as well as the loss generation mechanism. In the previous study, Honda et al. [50] found that the low speed design of rear rotor is effective to improve the efficiency by applying one-dimensional streamtube theory accompanying with the lift/drag characteristics of blade profile. Such an improvement of efficiency with low speed rear rotor design has been confirmed with the computational fluid dynamics (CFD) simulations, but the corner separation at the suction-hub corner of the rear rotor is also found to be more remarkable in the low speed design of rear rotor. It has been not yet clear why the efficiency can be still improved even with the pronounced corner separation by the reduced speed design of the rear rotor. Therefore, in this chapter, the loss generation mechanism in rear rotor of contra-rotating axial flow pump is investigated using three rear rotor models designed with the various speed.

2.1 Objective of the present chapter

The main objective of this chapter is to find an appropriate loss evaluation method to analyze loss generation mechanism in three designs of rear rotor in contra-rotating axial flow pump. To do so, three contra-rotating rotors models with different specific speeds are designed by employing conventional axial flow pump design method. Numerical simulations are carried out using a commercial CFD code ANSYS CFX-16.2/18.0 to examine the validity of the design. Furthermore, two loss evaluation methods, local entropy production rate and local rothalpy

Main body of this chapter has been published in International Journal of Fluid Machinery and Systems, Vol. 13, No.1, pp. 241-252 (2020).

change rate (material-derivative of rothalpy) are employed to identify the quantities and locations of loss generation. Since the local rothalpy change rate method shows more accurate prediction of loss quantities, the distribution of loss coefficient based on the local rothalpy change rate in the all three designed rear rotors are compared. The mechanisms for such losses are discussed based on time averaged (one relative revolution of front and rear rotors) results.

2.2 Methodology

2.2.1 Test rotors

All three types of test rotors for contra-rotating axial flow pump have been designed to satisfy the following specifications: the design flow rate of Q_d=70L/s, and the total head of $H_{d,t}$=4m. Both of the front and rear rotors are separately designed by a traditional two-dimensional design method, which has been widely used to design the blades of axial flow turbomachinery. The dimensional specific speeds of front and rear rotors $N_{s,i}$ ($i = f, r$, f: front rotor, r: rear rotor) generally used in Japan are defined as follows using rotational speed of each rotor N_i in min^{-1}, the design flow rate Q_d in m^3/min and the design head of each rotor $H_{d,i}$ in m.

$$N_{s,i} = \frac{N_i\sqrt{Q_d}}{{H_{d,i}}^{3/4}} \quad [\mathrm{min}^{-1}, \mathrm{m}^3/\mathrm{min}, \mathrm{m}] \tag{2-1}$$

Under the requirement of no swirl downstream of the rear rotor with no pre-swirl upstream of the front rotor, by considering the velocity triangle at meridional span of front and rear rotors, the Euler's theoretical head of front $H_{th,f}$ and rear $H_{th,r}$ rotors can be written as:

$$H_{th,f} = \frac{r\omega_f v_\theta}{g} \tag{2-2}$$

$$H_{th,r} = \frac{r\omega_r v_\theta}{g} \tag{2-3}$$

where r denotes meridional radius, ω_f and ω_r are the shaft angular speed (rad/s) of front and rear rotors respectively, v_θ represents the swirling velocity at the front rotor outlet (rear rotor

inlet), and g is the gravity.

By assuming the same hydraulic efficiency of the front and rear rotors ($\eta_f = \eta_r$), and according to the Eq. (2-1) combined with Eqs. (2-2) and (2-3), the head division between front ($H_{d,f} = \eta_f H_{th,f}$) and rear ($H_{d,r} = \eta_r H_{th,r}$) rotors will satisfy the following condition in terms of the specific speeds of the front $N_{s,f}$ and rear rotors $N_{s,r}$.

$$\frac{H_{d,f}}{H_{d,r}} = \left(\frac{N_{s,f}}{N_{s,r}}\right)^4 \tag{2-4}$$

From $H_{d,t} = H_{d,f} + H_{d,r}$, we can determine the heads of individual rotors, then the rotational speeds of rotors from the given specific speeds.

In the present study, all the front rotors are designed with a constant specific speed of $N_{s,f}$=1500[min^{-1},m^3/min, m] under the given head determined from Eq. (2-4), and the rear rotors are designed with the different specific speeds of $N_{s,r}$=1200, 1300 and 1400[min^{-1}, m^3/min, m]. Table 2-1 summarizes the main specifications of rear rotors in all three combinations. The three combinations are named after the specific speed of rotors like N055 1500-1200, N055 1500-1300 and N055 1500-1400. Figure 2-1 shows the shapes of rotors for the three designs. As we can see from blade shapes of rear rotor colored by green in the figure, the length of rear rotor is decreased with the increase of the specific speed for rear rotor. The NACA44 series are chosen for the blade profile, the thickness and chord ratio are decreased from hub to tip in both front and rear rotors. The tip and hub diameters are fixed with D_t=198mm and D_h=110mm (D_h/D_t=0.55) respectively. The casing diameter is D_c=200mm, resulting in the tip clearance of τ =1mm. The blade numbers of front and rear rotors are 4 and 5 respectively. It should be noted that, in each combination, the front rotor has been designed separately despite of the constant $N_{s,f}$, since the head division $H_{d,f}$ as well as the rotational speed is different. It can be seen that with the small reduction of the design specific speed of rear rotor, the rotational speed of rear rotor is significantly reduced with the increase of the front rotor speed. In the present study, we will focus only on the hydraulic

efficiency. If the suction performance is also important, some optimized combination of rotor specific speeds should be discovered.

Table 2-1 Main specifications of rear rotors in test rotors

Rear Rotor	N055 1500-1200	N055 1500-1300	N055 1500-1400
Design specific speed $N_{s,r}$ [min^{-1},m^3/min,m]	1200	1300	1400
Design head $H_{d,r}$ [m]	1.16	1.44	1.73
Rotational speed N_r [min^{-1}]	655	835	1029
Solidity σ_r [-]	1.06-0.93-0.81	0.94-0.84-0.73	0.86-0.76-0.66
Stagger angle γ_r [º]	50.4-58.0-64.0	55.8-63.8-69.5	59.8-67.9-73.3
Hydrofoil	[Hub]NACA 4408-[Mid span]NACA 4406-[Tip]NACA 4404		

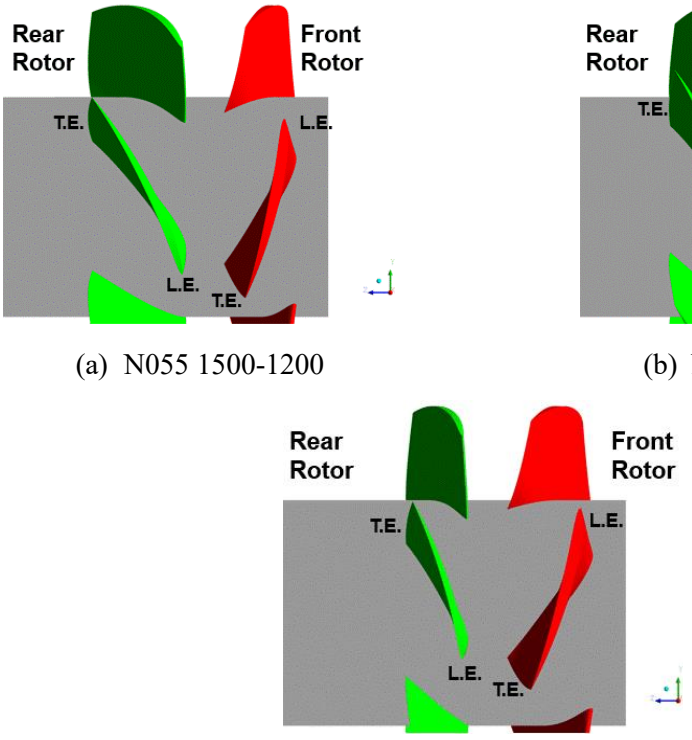

(a) N055 1500-1200 (b) N055 1500-1300

(c) N055 1500-1400

Fig. 2-1 Shape of test rotors

2.2.2 Numerical setup

To evaluate the hydraulic performance of the three combinations of counter rotating rotors, numerical simulations using the commercial CFD code, ANSYS CFX-16.2/18.0, are conducted. Figure 2-2 (a) shows the numerical model for whole rotors of N055 1500-1200. For the all combinations, the inlet boundary is located at $4D_c$ upstream of the leading edge of front rotor, while the outlet boundary is located at $1.3D_c$ downstream of the trailing edge of rear rotor. It is known that there are limitations of simulations for only one passage [51]. Moreover, for the contra-rotating axial flow pump, it has been found that the unsteady simulation of the whole rotors is necessary for the accurate predictions of overall performance due to rotor-rotor interactions [52].

Momosaki et al. [52] have well predicted the pump performance and internal flow field by conducting unsteady Reynolds-Averaged Navier-Stokes (RANS) based simulations. The comparisons of head evaluated by numerical simulations and experiments for the equal speeds contra-rotating rotors are shown in Table 2-2. For the steady simulation, only the one flow passage is solved for the both front and rear rotors with the mixing plane approximation applied at the interface between the front and rear rotor passage domains. On the other hand, the full passages are considered for the unsteady simulation to properly solve the rotor-rotor interaction. It is clearly seen that the good agreement can be obtained between results of RANS based unsteady simulations and experiments not only for the design flow rate of Q=70L/s but also for the deep part load of Q=21L/s.

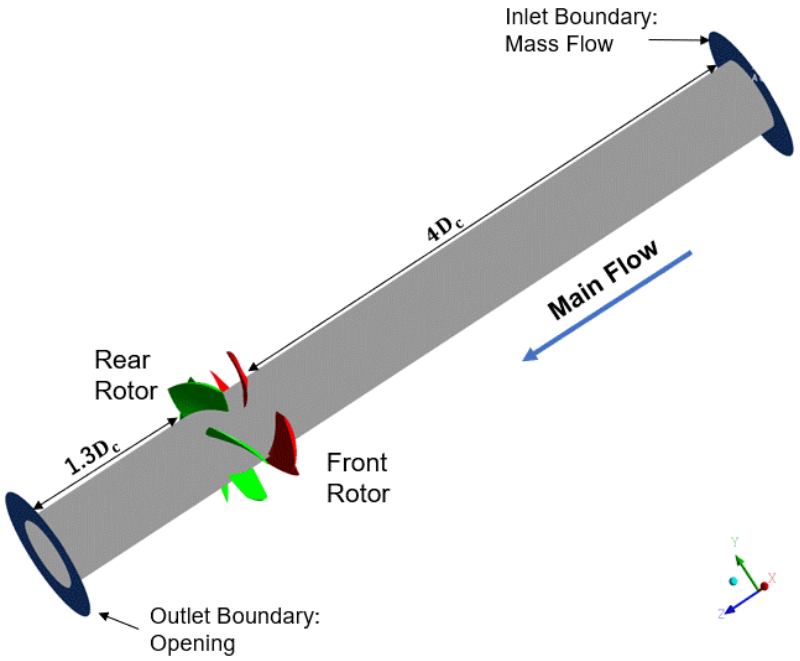

(a) Numerical model (about 7 million nodes) for whole rotors of N055 1500-1200

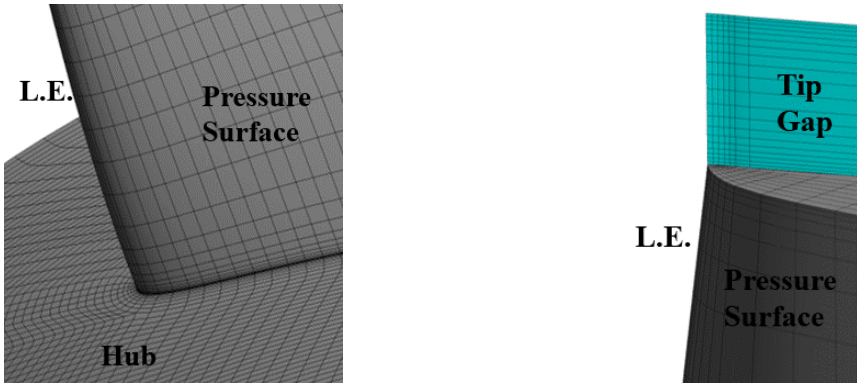

(b) Grids at hub and tip regions of N055 1500-1200 front rotor

Fig. 2-2 N055 1500-1200 numerical model

Table 2-2 Comparisons of pump head between numerical simulations and experiments in [52]

	Q=70L/s ($100\%Q_d$)			Q=21L/s ($30\%Q_d$)		
	H_f [m]	H_r [m]	H_t [m]	H_f [m]	H_r [m]	H_t [m]
Unsteady simulation	1.53	1.59	3.12	2.37	4.77	7.14
Steady simulation	1.41	1.00	2.41	2.61	4.19	6.80
Experiments	1.64	1.67	3.31	3.06	4.13	7.18

Therefore, in the present study, the unsteady RANS based simulations are again carried out for the three combinations of test rotors. In order to well capture the flow separation, *k-ω* based Shear Stress Transfer (SST) turbulence model is employed. Since no experimental data are available for new designs, experimental validations are not conducted. Instead, thorough grid dependency checks are conducted for the three models as will be seen later. Since the changes of numerical results are small enough, the total nodes number for whole the front and rear rotors of all three models are finally chosen to be about 7 million. Furthermore, in order to well capture the tip leakage flow, 20 layers of elements are radially located in the 1mm blade tip clearances as shown in Fig. 2-2 (b).

As for the boundary conditions, the inlet boundary type is chosen for the inlet boundary with defining the mass flow rate, while opening boundary type is chosen for the outlet boundary with the constant static pressure. No-slip wall condition has been selected for the blade surfaces, hub and the casing. Since *k-ω* based turbulence model requires high grid resolution near wall, numerical models with good grid resolution near the blade are constructed, where the minimum y^+ is about 0.5 and area averaged y^+ is about 5.0. Here y^+ is the dimensionless distance from the wall, and it is written as: $y^+ = \sqrt{\tau_\omega/\rho} \cdot \Delta n/\nu$, where τ_ω is the wall shear stress, Δn denotes the distance between the first and second mesh points off the wall, and ν is the flow kinematic viscosity. As high resolution of grids near wall cannot be guaranteed at all walls, an automatic near-wall treatment is employed for the *k-ω* based SST turbulence model, which allows for a smooth shift from low-Reynolds number formulation to a logarithmic wall function.

The high-resolution scheme is chosen for calculating the advection terms in the discrete volume equations. The second-order-backward-Euler advection scheme is used for the turbulence model. The shape functions are employed to calculate spatial derivatives for all the diffusion terms.

The time-step is determined as the following equation, which means that the front and rear

rotors rotate relatively in 0.5º during one time-step (720 steps for one relative revolution of front and rear rotors):

$$\Delta t = \frac{0.5°}{360°} \times \frac{60\ [\mathrm{s/min}]}{N_f + N_r} \tag{2-5}$$

The result of steady RANS simulation for front and rear rotors with a fixed relative position (Frozen Rotor) is employed to be the initial value for the unsteady calculations. In order to minimize the effect of initial values chosen for the unsteady simulations, numerical simulations for all three models are conducted for front and rear rotor rotating in 8 relative revolutions (5760 steps), where the stable flow variations have been observed. The time-averaged values during final revolution are used for the evaluation of performance and losses, by which the effect of unsteadiness can be decreased.

2.2.3 Loss evaluation methods

2.2.3.1 Local entropy production rate

Recently, Kock and Herwig [16] have proposed a loss evaluation method based on the local entropy generation rate for incompressible fluids. In the single-phase flow with incompressible fluid and Fourier heat conduction, the transport equation for entropy *s* can be written as:

$$\rho\left(\frac{\partial s}{\partial t} + u\frac{\partial s}{\partial x} + v\frac{\partial s}{\partial y} + w\frac{\partial s}{\partial z}\right) = -div\left(\frac{\vec{q}}{T}\right) + \frac{\Phi}{T} + \frac{\Phi_\theta}{T^2} \tag{2-6}$$

where ρ denotes the fluid density, *u*, *v* and *w* are velocities in *x, y, z* directions respectively, $\vec{q}$ means heat flux density vector, *T* represents the temperature, Φ/T describes the entropy production by viscous dissipation, and Φ_θ/T^2 describes the entropy production by heat transfer.

Assuming that the heat transfer terms are negligible in Eq. (2-6), the Reynolds-averaged local entropy production rate $\bar{\dot{S}}$ can be directly related to the dissipation function Φ as:

$$\bar{\dot{S}} = \overline{\left(\frac{\Phi}{T}\right)} = \dot{S}_D + \dot{S}_T \tag{2-7}$$

$$\dot{S}_D = \frac{\mu}{\bar{T}}\left\{2\left[\left(\frac{\partial \bar{u}}{\partial x}\right)^2 + \left(\frac{\partial \bar{v}}{\partial y}\right)^2 + \left(\frac{\partial \bar{w}}{\partial z}\right)^2\right] + \left(\frac{\partial \bar{v}}{\partial x} + \frac{\partial \bar{u}}{\partial y}\right)^2 + \left(\frac{\partial \bar{w}}{\partial y} + \frac{\partial \bar{v}}{\partial z}\right)^2 + \left(\frac{\partial \bar{u}}{\partial z} + \frac{\partial \bar{w}}{\partial x}\right)^2\right\} \tag{2-8}$$

$$\dot{S}_T = \frac{\mu}{\bar{T}}\left\{2\left[\overline{\left(\frac{\partial u'}{\partial x}\right)^2} + \overline{\left(\frac{\partial v'}{\partial y}\right)^2} + \overline{\left(\frac{\partial w'}{\partial z}\right)^2}\right] + \overline{\left(\frac{\partial v'}{\partial x} + \frac{\partial u'}{\partial y}\right)^2} + \overline{\left(\frac{\partial w'}{\partial y} + \frac{\partial v'}{\partial z}\right)^2} + \overline{\left(\frac{\partial u'}{\partial z} + \frac{\partial w'}{\partial x}\right)^2}\right\} \tag{2-9}$$

where μ is the dynamic viscosity of fluid. $\partial u_i/\partial x_i$ means velocity gradient components, $\bar{}$ and $'$ respectively denote mean and fluctuating components which are separated through the Reynolds-Averaged Navier-Stokes equation.

The entropy production rate by the direct dissipation $\dot{S}_D$ which includes the mean velocity gradients can be directly calculated in the RANS based simulations, while the entropy production rate by the turbulent dissipation $\dot{S}_T$ that contains the fluctuating velocity gradients can be approximated by using the turbulence dissipation rate ε of the turbulence model [16]. Therefore, Eq. (2-9) can be approximated as:

$$\dot{S}_T = \frac{\rho\varepsilon}{\bar{T}} \tag{2-10}$$

2.2.3.2 Local rothalpy change rate

It has been known that the rothalpy [23] stays conserved in the steady and adiabatic flow along a relative streamline. Lyman [27] indicates the relation between the change rate of rothalpy without internal energy and the local entropy production rate in incompressible steady adiabatic flows with the constant rotor speed. Therefore, it seems possible to utilize the change rate of the local rothalpy without internal energy to locate the local losses in the hydraulic fluid machinery. In incompressible flow, the rothalpy *I* can be written as:

$$I = e + \frac{p}{\rho} + \frac{1}{2}[W^2 - (r\omega)^2] \tag{2-11}$$

where *e, p, ρ, W, r* and ω denote the specific internal energy, the static pressure, the density, the relative velocity, the radius from the rotating axis and the angular rotational speed of rotor respectively. Since the unsteadiness in the rotor-fixed frame could be small enough at the design flow rate, the flow is treated as in steady condition. In the incompressible flow analysis under the steady flow condition, mechanical energy terms, i.e. $I - e$, should be conserved if no loss occurs along the streamline. In other words, if there is flow loss, the material derivative of this term as follows should exist and represent the local loss production rate, that is the local power loss per unit volume.

$$\rho \frac{D(I-e)}{Dt'} = \rho \frac{D(\frac{p}{\rho} + \frac{1}{2}W^2 - \frac{1}{2}U^2)}{Dt'} \tag{2-12}$$

where D/Dt' represents the material derivative in the rotating frame which is fixed to the rotor. Since only Reynolds-averaged variables are available in RANS based simulations, only the Reynolds-averaged Equation (2-12) will be considered in the present paper. In order to simplify the Reynolds-averaging problem, the homogeneous turbulence has been assumed. It has been found that the unsteadiness in rotor-fixed frame due to rotor-rotor interaction is very small at the design flow rate condition, therefore, $\partial/\partial t' \approx 0$. Then, the Reynolds-averaged local rothalpy change rate can be calculated by the following equation:

$$\overline{\rho \frac{D(I-e)}{Dt'}} \approx \bar{W}_i \frac{\partial \bar{p}}{\partial x_i'} + \rho \bar{W}_j \bar{W}_i \frac{\partial \bar{W}_j}{\partial x_i'} - \rho\omega^2(\bar{u}x' + \bar{v}y') \tag{2-13}$$

where $\bar{}$ means the Reynolds-averaged value, and $'$ denotes the coordinate fixed to the relative frame rotating with each rotor. However, it should be noted that fluctuating terms (i.e. $\rho \bar{W}_i \, \partial \overline{W_j' W_j'} / \partial x_i'$) have not been considered in Eq. (2-13). We have also calculated the fluctuating terms by using the turbulence dissipation rate ε, and find its time-averaged value is very small. Therefore, in order to reduce the effect of fluctuating terms, the Reynolds-averaged local rothalpy

change rate is averaged in one relative revolution (720 steps) of front and rear rotors to evaluate the loss quantities and locations in rear rotor.

2.2.4 Loss quantity evaluation

The amount of loss power in the rear rotor domain will be calculated with the local entropy production rate and local rothalpy change rate, which will be compared with the actual energy loss based on the total pressure change through the rear rotor domain.

The actual loss power in the rear rotor domain $P_{loss,r}$ is:

$$P_{loss,r} = P_{shaft,r} - P_{output,r} \tag{2-14}$$

where

$$P_{shaft,r} = (T_{blades,r} + T_{hub,r})\omega_r \tag{2-15}$$

$$P_{output,r} = \iint_{surfaces} p_t \vec{V} \cdot \vec{n}\, dS \tag{2-16}$$

$P_{shaft,r}$ is the rear rotor shaft power which is determined by the torque on the blades $T_{blades,r}$, and the hub $T_{hub,r}$ multiplied by the angular shaft speed of rear rotor ω_r. $P_{output,r}$ is the rear rotor output power which is obtained with the total pressure p_t, absolute velocity vector $\vec{V}$ and unit normal vector $\vec{n}$ on the surfaces of rear rotor domain.

On the other hand, the local loss power in unit volume can be separately estimated based on the local entropy production Φ_E and the local rothalpy change rate Φ_R as follows:

$$\Phi_E = \bar{T}\dot{S}_D + \bar{T}\dot{S}_T \tag{2-17}$$

$$\Phi_R = -\rho \overline{\frac{D(I-e)}{Dt'}} \tag{2-18}$$

Integrating the above two over the volume of the considered domain, the total amount of loss powers in the rear rotor domain $P_{loss,r,E}$ and $P_{loss,r,R}$ can be calculated as follows;

$$P_{loss,r,E} = \iiint_{rear\ rotor} \Phi_E\, dV \tag{2-19}$$

$$P_{loss,r,R} = \iiint_{rear\ rotor} \Phi_R \, dV \tag{2-20}$$

Hydraulic losses evaluated by total pressure, $H_{loss,r}$, local entropy production rate, $H_{loss,r,E}$ and local rothalpy change rate, $H_{loss,r,R}$, can be determined by:

$$H_{loss,r} = \frac{P_{loss,r}}{\rho g Q_d} \tag{2-21}$$

$$H_{loss,r,E} = \frac{P_{loss,r,E}}{\rho g Q_d} \tag{2-22}$$

$$H_{loss,r,R} = \frac{P_{loss,r,R}}{\rho g Q_d} \tag{2-23}$$

where ρ is the density of the fluid, g denotes the gravity and Q_d represents the flow rate at the design condition.

It should also be noted that, the above hydraulic losses in rear rotor domain will also be averaged in one relative revolution of the rotors (720 steps). Ideally, the hydraulic losses based on local entropy production rate and local rothalpy change rate should be equal to the actual hydraulic loss $H_{loss,r}$ in Eq. (2-21). This condition can be also used for the grid dependency check of the present analysis.

2.2.5 Local loss coefficient

In order to understand the loss mechanism in the three different combinations of rotors, non-dimensional loss coefficient is introduced. As will be shown in Table 2-3 and 2-4, the hydraulic loss evaluated by the local entropy production rate shows remarkable discrepancy with the actual hydraulic loss, and such a large discrepancy seems to come from the near-wall treatment of two-equations turbulence model [16]. The logarithmic wall function has been applied in the wide area of blade surfaces; it is known that the special treatment should be made in this region to quantitatively estimate the loss quantity (e.g. [21][22]). On the other hand, it can be also found that the loss quantity based on local rothalpy change rate agrees well. Therefore, the loss

coefficient is calculated on the basis of the local rothalpy change rate as follows. The time averaged value will be used to localize the losses in rear rotor.

$$C_R = \frac{\Phi_R}{\rho\omega^2 Q_d / D_c} \tag{2-24}$$

2.3 Results and discussion

2.3.1 Grid independency

Various grids with different nodes number and y^+ (minimum y^+ on blades: y^+_{min}, area averaged y^+ on blades: $\overline{y^+}$) have been generated by using ANSYS TurboGrid 16.2/18.0. The grid independency of three models has been checked by conducting unsteady RANS based simulations. The efficiency of rear rotor η_r is evaluated based on time averaged (720 steps) shaft power $\bar{P}_{shaft,r}$ and output power $\bar{P}_{output,r}$ of rear rotor:

$$\eta_r = \frac{\bar{P}_{output,r}}{\bar{P}_{shaft,r}} \tag{2-25}$$

The time averaged loss quantities (actual hydraulic loss $\bar{H}_{loss,r}$, hydraulic loss based on rothalpy $\bar{H}_{loss,r,R}$ and hydraulic loss based on entropy $\bar{H}_{loss,r,E}$) in rear rotor domain are also calculated, and they are summarized in Table 2-3. As we can see, with the change of grids for three models, numerical results also vary a little, especially grid with fine resolution and small y^+, and therefore the grids with the better resolution (about 7 million nodes in front and rear rotor domains) and better y^+ are chosen for all three models. We believe such numerical errors are small enough to compare the losses in three models.

Table 2-3 Numerical results in rear rotors of three models with various grids

Model	Total nodes [-]	y^+_{min} [-]	$\overline{y^+}$ [-]	η_r [%]	$\overline{H}_{loss,r}$ [m]	$\overline{H}_{loss,r,R}$ [m]	$\overline{H}_{loss,r,E}$ [m]
N055 1500-1200	1176937	0.61	7.8	80.0	0.30	0.29	0.14
	4608464	0.47	4.9	80.6	0.29	0.30	0.16
	7131572	0.52	4.8	80.5	0.30	0.31	0.17
N055 1500-1300	1194187	0.53	8.0	79.6	0.38	0.36	0.18
	4673228	0.45	5.0	80.8	0.36	0.37	0.19
	7228732	0.43	5.0	81.0	0.36	0.38	0.20
N055 1500-1400	1211521	0.51	8.2	78.6	0.50	0.46	0.23
	4737404	0.43	5.2	79.3	0.49	0.48	0.25
	7325052	0.43	5.2	79.7	0.48	0.47	0.26

2.3.2 Performance evaluations and corner separation

The performances of all three models are evaluated by conducting unsteady simulations for the whole front and rear rotors which include the unsteadiness due to rotor-rotor interaction. The efficiencies are evaluated with time-averaged powers by utilizing similar method described in Eq. (2-25). In Fig. 2-3, it can be found that the better efficiency of rear rotor can be achieved in relatively low specific speed rear rotor design. As a result, total efficiency takes the maximum value with the medium specific speed of rear rotor $N_{s,r}$=1300[min^{-1}, m^3/min, m].

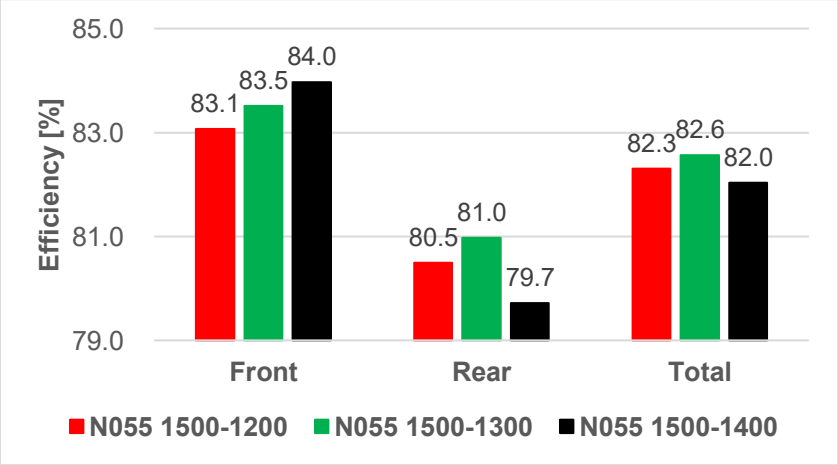

Fig. 2-3 Efficiencies based on unsteady simulations of three models

Figure 2-4 illustrates the distributions of limiting streamlines on the suction surface of rear rotors in all three models, from which we can find that the corner separation at the root of the blade becomes significant with the decrease of the specific speed of rear rotor. This agrees well with the findings in the previous study [50].

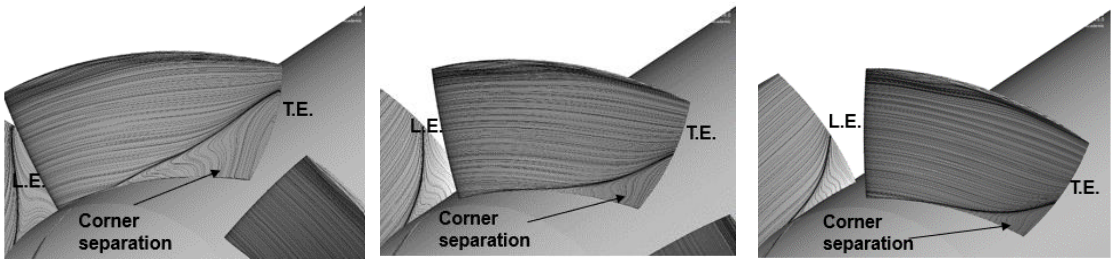

(a) N055 1500-1200 (b) N055 1500-1300 (c) N055 1500-1400

Fig. 2-4 Limiting streamlines on suction side of rear rotor

2.3.3 Loss quantities in rear rotor domain

Hydraulic losses in rear rotor domain of three models have been time averaged (720 steps) on the basis of unsteady simulations for whole front and rear rotors. The results are summarized in Table 2-4. It can be found that hydraulic loss evaluated by local rothalpy change rate shows better agreement with the actual loss quantity (around 100%) in all three models, while that calculated by local entropy production rate has remarkable discrepancy with the actual loss quantity (below 60%). The modification in the near-wall region as made in [21] [22] is not considered here, since it has been found that the improvement is not satisfactory in the present case [20], indicating the necessity of further investigation of near-wall mesh quality. Therefore, the local rothalpy change rate method will be used to analyze the locations and contributions of losses in rear rotor of three models.

Table 2-4 Summary of loss quantities in rear rotors of three models

	N055 1500-1200	**N055 1500-1300**	**N055 1500-1400**
$\overline{H}_{loss,r}$ [m]	0.30	0.36	0.48
$\overline{H}_{loss,r,E}$ [m]	0.17 (58.6% of $\overline{H}_{loss,r}$)	0.20 (55.7% of $\overline{H}_{loss,r}$)	0.26 (53.5% of $\overline{H}_{loss,r}$)
$\overline{H}_{loss,r,R}$ [m]	0.31 (103.1% of $\overline{H}_{loss,r}$)	0.38 (103.9% of $\overline{H}_{loss,r}$)	0.47 (97.6% of $\overline{H}_{loss,r}$)

2.3.4 Distributions of loss coefficient

Figure 2-5 shows the distributions of loss coefficient C_R based on local rothalpy change rate at the three axial locations with leading edge, mid-chord and trailing edge of rear rotor for three models. Linear range from 0.1 to 1 is used to emphasize the region with high loss coefficient.

From this figure, it is clearly seen that in the all three models, large dissipation occurs in the regions near the walls, especially in the tip region near the leading edge of rotor. Near the blade surfaces in T.E. cross sections, it can be found that the region with high loss coefficient is wider for the lower specific speed rear rotor. This agrees well with the corner separation size indicated by limiting streamlines on the suction surface of rear rotors in Fig. 2-4.

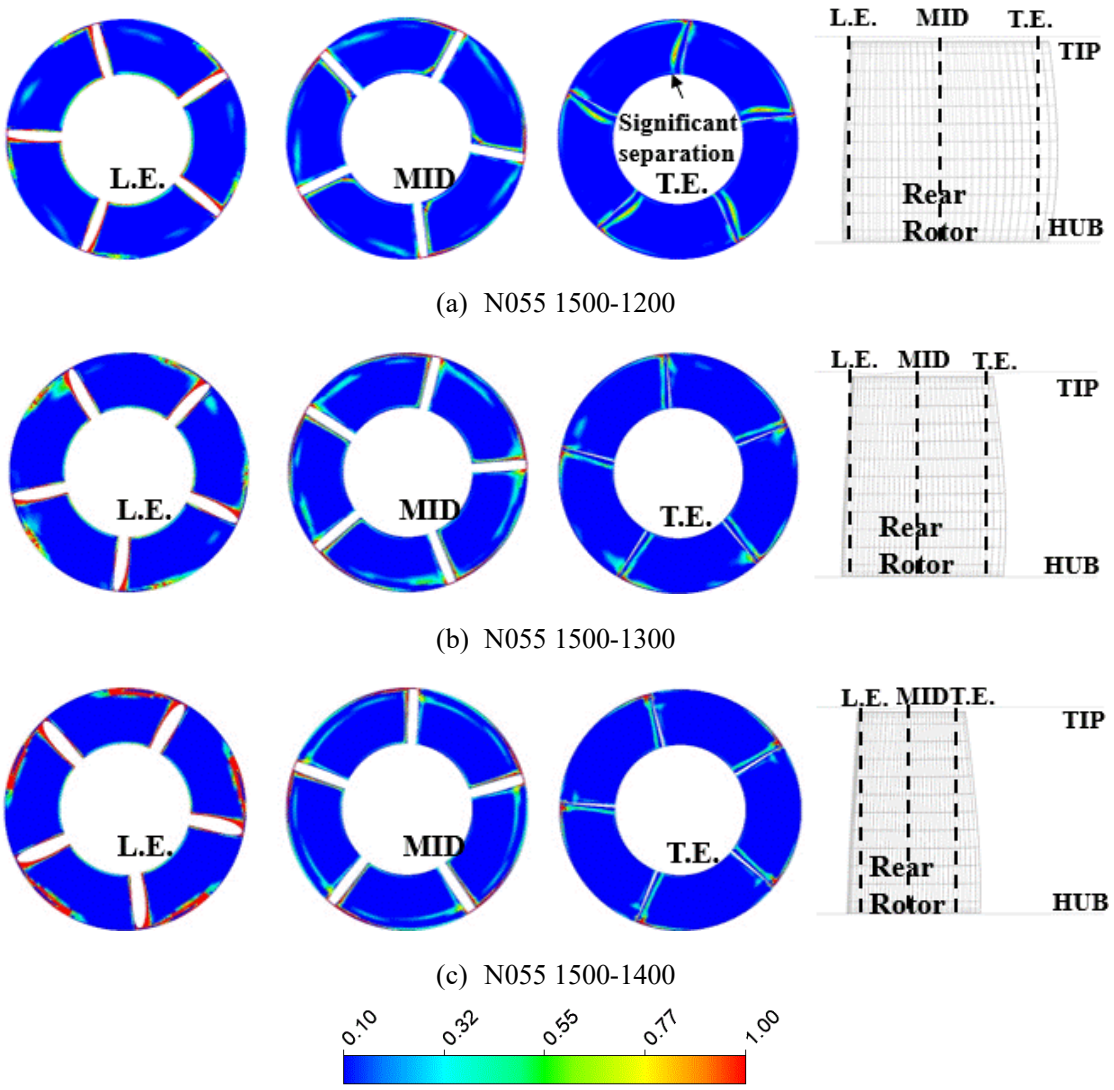

Fig. 2-5 Loss coefficient C_R distributions at leading edge (L.E.), mid-chord (MID) and trailing edge (T.E.) sections of rear rotors in three models

2.3.5 Loss contribution

As mentioned above, large losses have been observed near the casing, blade surfaces and hub, and the local rothalpy change rate method can well predict the quantities and locations of losses. Therefore, in all three models, we divided the domain into 3 regions ('Tip', 'Mid' and 'Hub' shown in Fig. 2-6 (d)) with the same sectional area from casing to hub, at the same time. Each region is equally divided into 26 parts from the inlet of rear rotor domain to the downstream of

rear rotor in the axial direction. Every divided part has the identical volume: $2.3 \times 10^{-5}\mathrm{m}^3$, then the loss contribution η_{loss} of each part can be obtained by:

$$\eta_{loss} = \iiint_{each\ part} \Phi_R dV \Big/ P_{shaft,r} \tag{2-26}$$

Figure 2-6 illustrates the axial distribution of loss contribution η_{loss} in 'Tip' (green line), 'Mid' (red line) and 'Hub' (black line) regions of three models. The horizontal axis represents the axial position normalized by the chord length of rear rotor in model N055 1500-1200. The vertical dashed lines with 'L.E.' and 'T.E.' display the positions of leading edge and trailing edge of rear rotors in each model.

In Fig. 2-6, it can be easily found that the magnitude of loss contribution in 'Tip' region is the highest in the three regions, especially around the leading edge of rear rotor in each model, indicating that dominant loss occurs in the 'Tip' region near leading edge. Even though the large high-loss-coefficient area caused by corner separation can be observed in the 'Hub' region near the T.E. of low specific speed rear rotor, its loss contribution is small enough compared with that in 'Tip' region. It can also be found that the magnitude of loss contribution peak in the 'Tip' region of N055 1500-1400 is the highest, which may explain its deteriorated efficiency. It is also noticed that the peak of the loss in tip region is closer to the leading edge in the highest specific speed rear rotor design, which seems to be the result of the tip leakage vortex (TLV) structures. This will be discussed in the following section.

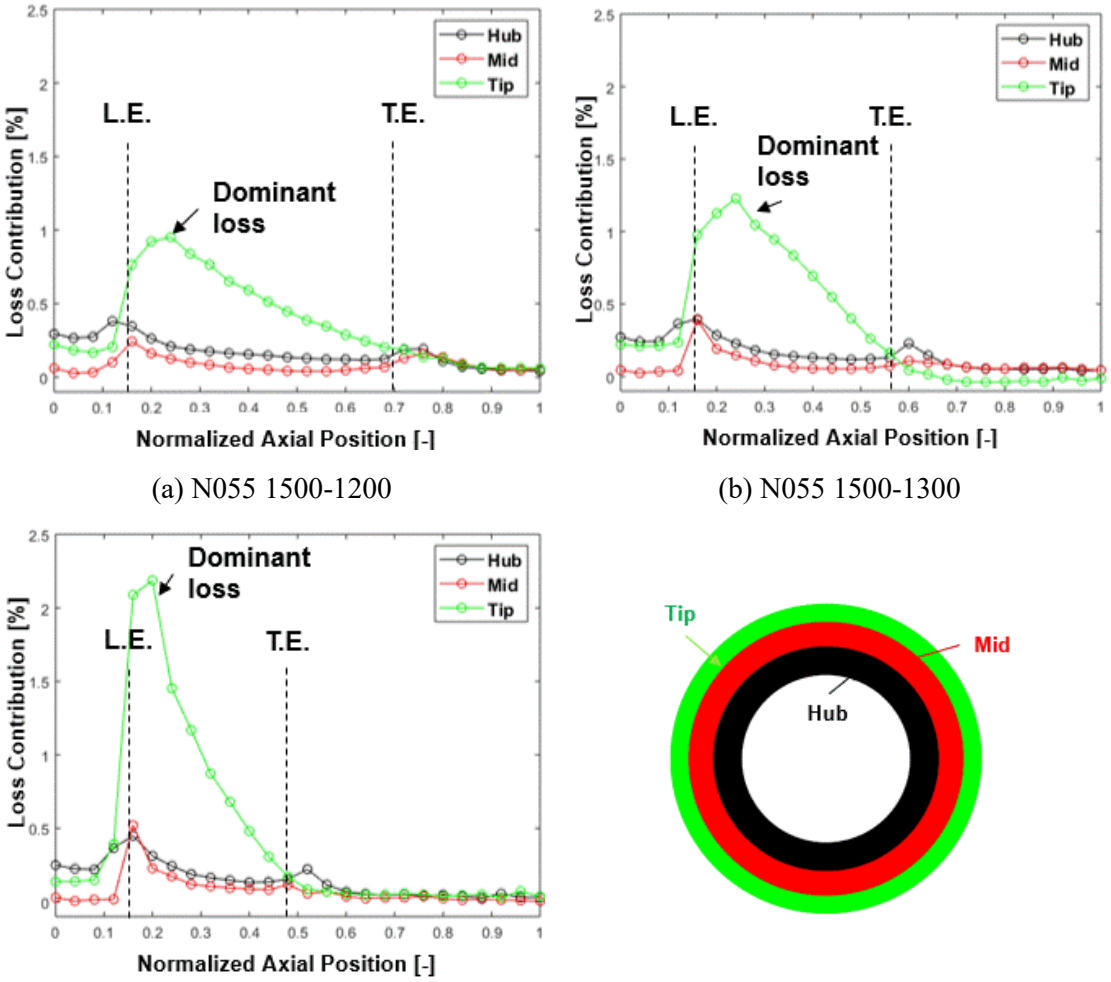

(a) N055 1500-1200 (b) N055 1500-1300

(c) N055 1500-1400 (d) Three regions

Fig. 2-6 Axial distribution of loss contribution in three regions with equally divided volume of $2.3 \times 10^{-5}\mathrm{m}^3$ for three rear rotor models

2.3.6 Tip leakage vortex structures

The large loss contribution has been observed in the 'Tip' region, where as a result of unsteady shear layer of interface between tip leakage flow and the mainstream, tip leakage vortex (TLV) forms. A normalized relative velocity ξ_W based on tip radius r_t and rear rotor angular speed ω_r has been specified to display the tip leakage vortex structure. It should be noted that the relative velocity W is also time averaged in one relative revolution (720 steps) of front and rear rotors.

$$\xi_W = \frac{W}{r_t \cdot \omega_r} \tag{2-27}$$

As shown in Fig. 2-7, six *r-z* planes are equally located between two blades (from the leading edge of one blade to adjacent blade). In Fig. 2-8, the normalized relative velocity ξ_W is plotted in these six *r-z* planes. As the black dashed arrows indicate, the tip leakage vortex core is characterized by the low relative velocity, meaning that the tip leakage vortex is a kind of wake type.

In Fig. 2-8, it can also be seen that the tip leakage vortex core in the rear rotor with the highest specific speed (N055 1500-1400) reaches the leading edge of the adjacent blade, which should result in the strong interaction of tip leakage vortex structure with the adjacent blade. In rear rotor with low specific speeds, the tip leakage vortex just goes through the flow passage, which should weaken such interaction.

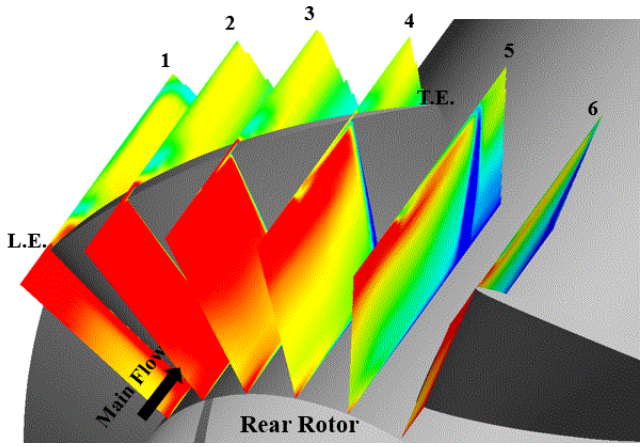

Fig. 2-7 Distribution of *r-z* planes in rear rotor

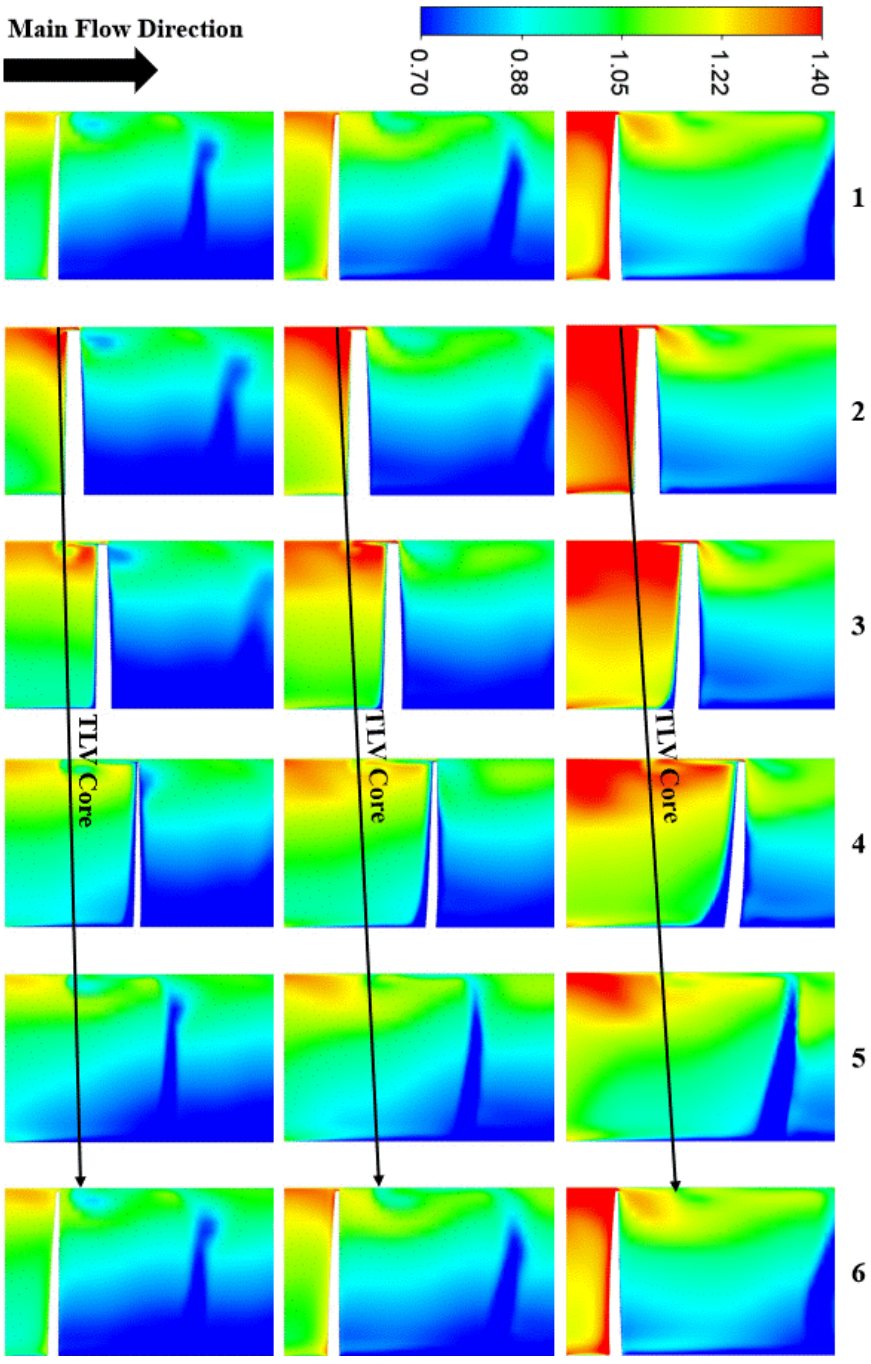

Fig. 2-8 Normalized relative velocity ξ_W distributions in *r*-*z* planes in rear rotor

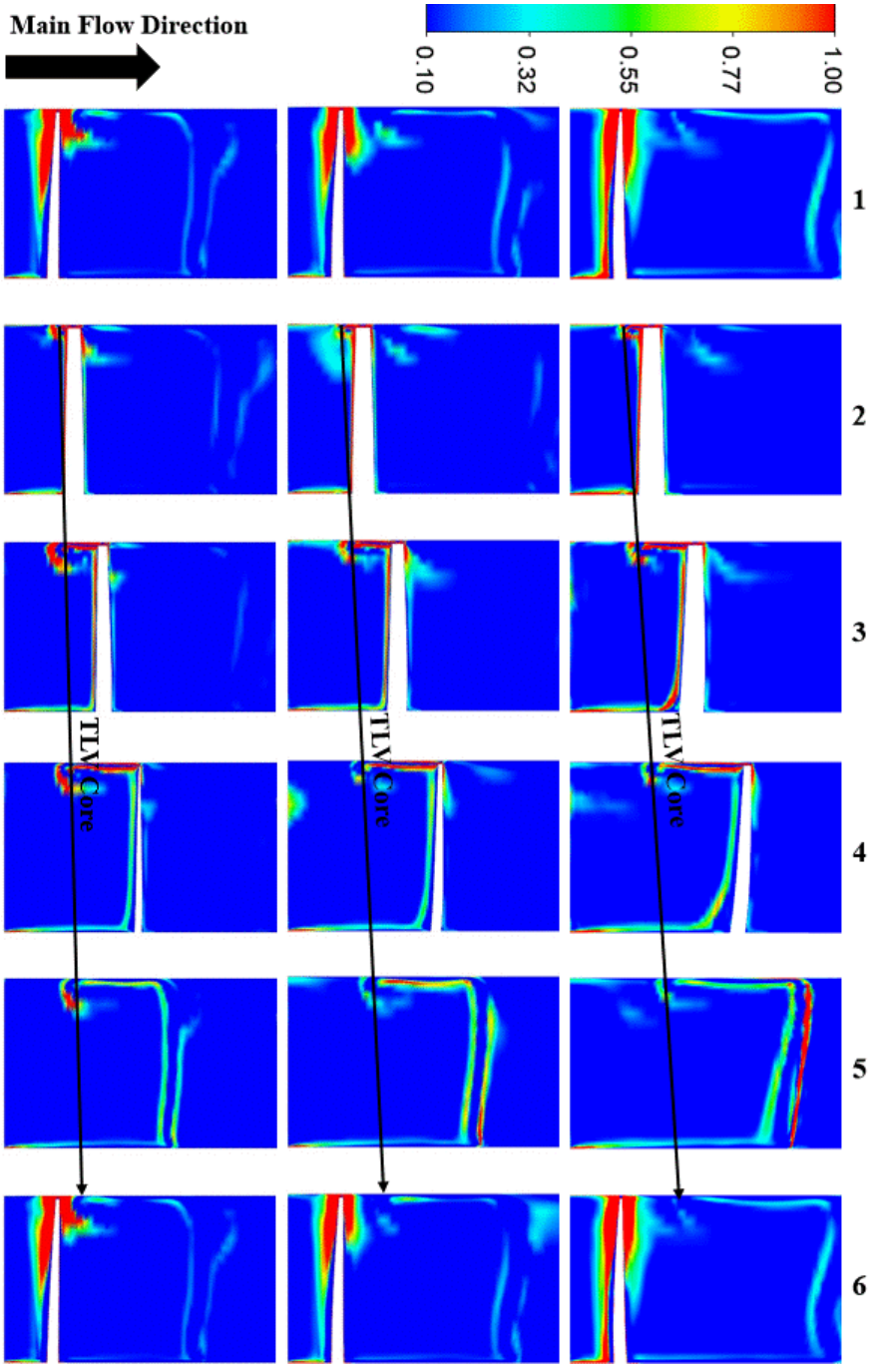

Fig. 2-9 Loss coefficient C_R distributions in *r-z* planes in rear rotor

Distributions of loss coefficient on the same *r-z* planes are also displayed in Fig. 2-9. Regions with high loss coefficient (red color) represent large loss region. As we can see, high loss coefficient regions occur near the tip leading edges (shown in *r-z* planes 1 and 6) as well as along the leakage vortex cores (extending from plane 2 to 6). Loss near the tip leading edges may be the result of interaction of casing boundary layer, blade rows and other complex flow phenomena [53], and it seems to be common in the all combination of rotors. Figure 2-10 shows the distribution of limiting streamlines on the pressure surface (P.S.) of rear rotors. Combining with Fig. 2-4, no flow separations are observed in both sides of the blade leading edge (L.E.). It can be found that flow near the tip side of P.S. moves to the suction side through the tip clearance. Therefore the loss near the TLV cores shown in Fig. 2-9 seems to be the result of mixing process caused by the TLV blockage effect [53]. Larger area with higher loss coefficient can be observed near TLV cores in the highest specific speed rear rotor (N055 1500-1400), and this may indicate that the strong interaction between tip leakage vortex and adjacent blade in the highest specific speed rear rotor strengthens such blockage effect, which results in much higher losses due to the stronger mixing process. As it has been observed, the angle of the tip leakage vortex core against the circumferential direction varies with the specific speed, and high losses also occur around the TLV cores, which explains why the peak of loss contribution curve in tip region of N055 1500-1400 (shown in Fig. 2-5) is closer to the leading edge of rear rotor.

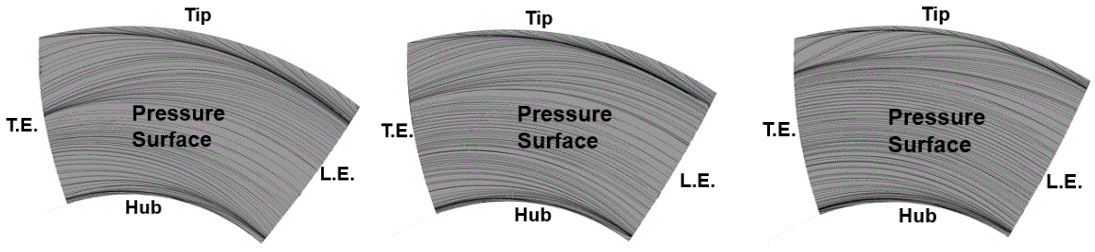

(a) N055 1500-1200 (b) N055 1500-1300 (c) N055 1500-1400

Fig. 2-10 Limiting streamlines on pressure side of rear rotor

2.4 Summary

In this chapter, in order to understand the loss mechanism in rear rotor of contra-rotating axial flow pump, unsteady numerical simulations for whole front and rear rotors have been conducted for the three types of rear rotor designed with the different specific speeds. An appropriate loss evaluation method has been chosen to predict the location and quantity of losses. Main findings are summarized as follows:

1) The loss evaluation method based on local rothalpy change rate enables us to evaluate local loss generation quantitatively.
2) Even though remarkable corner separation is observed in the low specific speed rear rotor, its loss contribution is very small compared with that in the tip region. The loss in the tip regions seems to be highly associated with the tip leakage vortex (TLV) probably through the blockage effect of TLV.
3) In the low specific speed rear rotor, the interaction of TLV and adjacent blade is weakened which seems to relieve the blockage effect of TLV. The contribution of mixing loss due to such effect is also reduced, resulting in the improved efficiency with lower specific speed design of rear rotor.

Chapter 3

Performance prediction model of contra-rotating axial flow pump with separate rotational speed of front and rear rotors

Pumps are usually operated at both of design and off-design flow rates for various purposes. However, most pumps suffer from significantly deteriorated performance at the off-design flow rates, and the performance of contra-rotating axial flow pump is also decreased considerably under the off-design conditions. In the past study, rotational speed control (RSC) has been applied separately for the front or rear rotor of contra-rotating axial flow pump to improve the performances at off-design flow rates [40]. However, thorough investigations are still necessary for further improvement by applying a simultaneous control of both of front and rear rotors in contra-rotating axial flow pump. Because of the unaffordable time of conducting experiments or computational fluid dynamics (CFD) simulations, a performance prediction model in contra-rotating axial flow pump is significantly important toward the establishment of effective method of RSC. Furthermore, the construction of performance prediction model would be also very meaningful for the design of rotors making the best use of the advantage of RSC in contra-rotating axial flow pump. Example of such design will be described in the next chapter.

3.1 Objective of the present chapter

The main objective of this chapter is to establish and verify the performance prediction model for contra-rotating axial flow pump to determine the optimum rotational speeds of rotors under RSC. In this chapter, the construction of the performance prediction model is firstly demonstrated.

Main body of this chapter has been published in JSME Journal of Fluid Science and Technology, Vol. 15, No. 3 (2020).

CFD simulations are conducted to establish and validate the performance prediction model. Experimental results are also employed to validate the proposed model as well as the referred CFD simulations. Finally, an energy saving application of the proposed model is illustrated for two typical system resistances imitating some applications.

3.2. Performance prediction model

3.2.1 Overall strategy

Before the detailed description of the performance prediction model, the overall strategy of the performance prediction model is introduced firstly. It has three steps in the performance prediction model as shown in Fig. 3-1. The 1st step is to determine the theoretical head; the 2nd step is to evaluate the loss quantities; the 3rd step is to predict the head and efficiency.

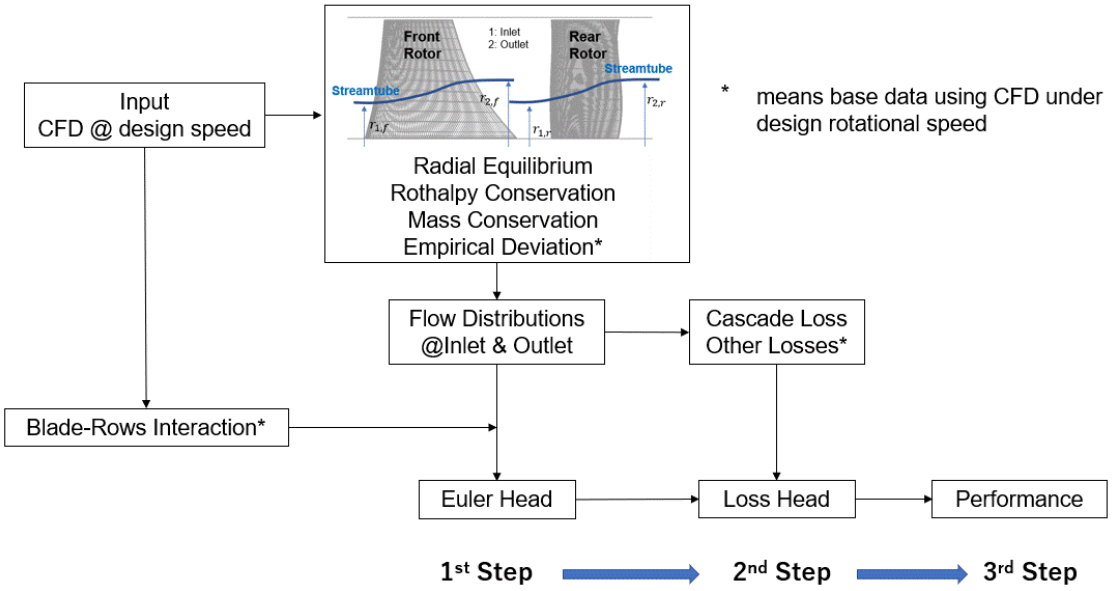

Fig. 3-1 Main components of the performance prediction model

To construct the performance prediction model along the above procedure, base flow data of test contra-rotating axial flow pump are necessary. In this study, they will be obtained by CFD

simulations. It should be emphasized that CFD simulations are conducted only for the design rotational speed conditions; such simulations are not additional tasks since they are generally carried out during the usual pump design. Using the base data for the * marked components illustrated in Fig. 3-1, models of empirical deviation, blade-rows interaction and other losses are constructed. Then, the proposed prediction model is used to predict the performances under various rotational speed conditions without conducting further CFD simulations.

3.2.2 Test rotors

Two previous-designed contra-rotating axial rotors are employed in this study: RR2 type [39] and RR3 type [38]. The experimental results of RR2-type rotors will be used to verify the CFD and the proposed performance prediction model, while the RR3-type rotors are employed to demonstrate the energy saving application of the proposed model. Both types of rotors have been designed for the following specifications: total head $H_{t,d} = 4\mathrm{m}$, flow rate $Q_d = 70\mathrm{L/s}$, and specific speed of front and rear rotors $N_{s,f} = N_{s,r} = 1500[\mathrm{min}^{-1}, \mathrm{m}^3/\mathrm{min}, \mathrm{m}]$. The RR2-type rotors are designed with equal speed, in which strong blade-rows interactions and significant cavitation have been observed [39]. RR3-type rotors have improved the weaknesses (i.e. strong interaction and remarkable cavitation) of RR2-type rotors by using different-speed design method [38]. The main profile information of RR2-type and RR3-type rotors are summarized in Table 3-1, and the shapes of the test rotors are illustrated in Fig. 3-2. The casing inner diameter is D_c=200mm, which results in the tip clearance of 1mm.

Table 3-1 Main profile specifications of RR2-type and RR3-type rotors

		Hub	Mid-span	Tip
Diameter [mm]		100	149	198
Front Rotor	Blade Number	4		
	Hydrofoil	NACA4410	NACA4408	NACA4406
	Solidity σ [-]	1.290	0.898	0.700
	Stagger Angle γ [°]	51.72	68.48	75.85
RR2-type Rear Rotor	Blade Number	5		
	Hydrofoil	NACA4410	NACA4408	NACA4406
	Solidity σ [-]	0.840	0.720	0.600
	Stagger Angle γ [°]	64.24	72.54	77.56
RR3-type Rear Rotor	Blade Number	5		
	Hydrofoil	Special shapes [38]		
	Solidity σ [-]	1.008	0.864	0.720
	Stagger Angle γ [°]	64.95	69.73	71.88

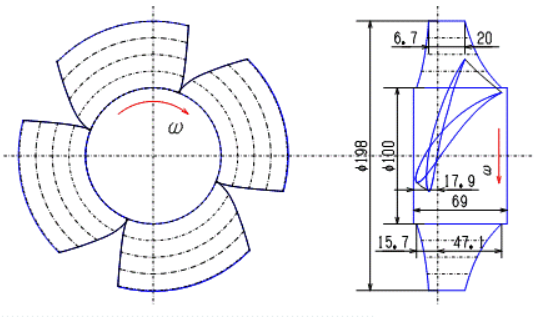

(a) Front rotor of RR2 and RR3

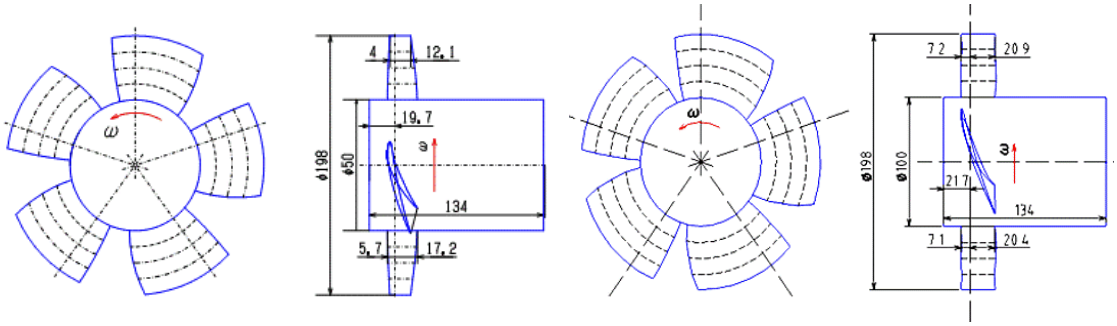

(b) RR2-type rear rotor (c) RR3-type rear rotor

Fig. 3-2 Shapes of test rotors

3.2.3 CFD analysis for base data

CFD simulations are firstly conducted for the design speed operations to provide the base flow data which are used to construct the performance prediction model. Then, CFD simulations are also conducted to validate the model under the rotational speed control (RSC). The both simulations are made by a commercial CFD code: ANSYS CFX 18.0/2019 R3.

Figure 3-3 illustrates CFD models for the numerical simulations. The inlet boundary is located at $4D_c$ upstream of the leading edge of front rotor. The outlet boundary is located at $1.3D_c$ downstream of the trailing edge of rear rotor or $1.7D_c$ downstream of the trailing edge of front rotor. Even though Momosaki et al. [52] have well predicted the performance and internal flow in contra-rotating axial flow pump at both of design and off-design conditions by conducting unsteady Reynolds-Averaged Navier-Stokes (RANS) simulations, such computation is too expensive to validate all the results calculated by the performance prediction model. On the other hand, we are focusing on establishing a performance prediction model to evaluate performance under operations with high performance where unfavorable flows may be well relieved with the aid of appropriate method of RSC. Therefore, in this study, the steady RANS equations are solved in only one passage of front and rear rotors in contra-rotating axial flow pump, which has so far a good enough accuracy with reasonable time consumption. The unsteady RANS simulation for the whole front and rear rotors will be a future alternative when sufficient computational resources would be available, which is expected to contribute to the improved accuracy of performance prediction model.

The Shear Stress Transport (SST) model are employed as a turbulence model in the RANS simulations. The mixing plane is also located between front and rear rotors' flow domain to help calculate the steady flow through the front and rear rotors. The flow data at the mixing plane are

averaged in circumferential direction on both the outlet of front rotor and inlet of rear rotor, which is like a real mixing process.

The advection terms in the discrete volume equations are determined with the high-resolution scheme. The upwind advection scheme is set for the turbulence model equations. Diffusion terms are evaluated with shape functions. The inlet boundary condition is defined with mass flow rate. The outlet boundary condition is set as opening type with relative pressure of 0Pa. No-slip wall is chosen for the surfaces of rotors, shroud and hub. The automatic near-wall treatment has been employed for the SST turbulence model. Root mean square (RMS) residual of 10^{-4} for each conservation law is chosen as the conservation criteria, with which stable flow results are expected to be achieved.

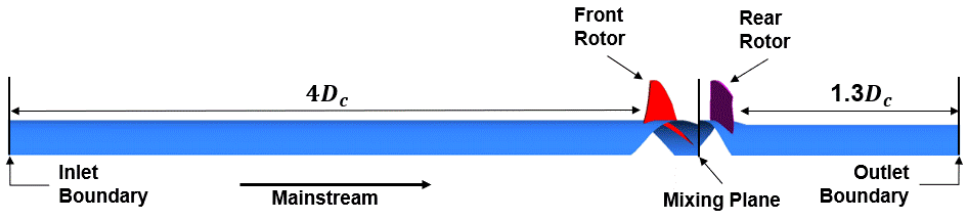

(a) CFD model for front and rear rotors

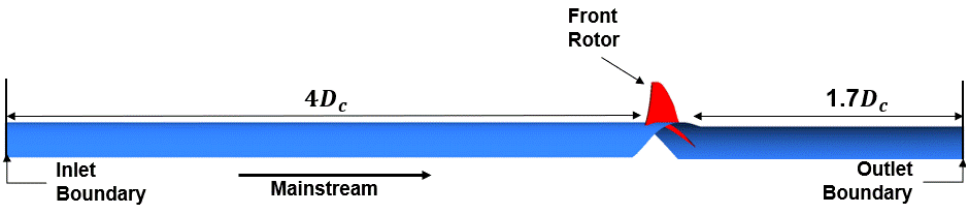

(b) CFD model for only front rotor

Fig. 3-3 CFD models for simulations

3.2.3.1 CFD numerical models

Computational meshes are generated by using ANSYS TurboGrid 18.0. In order to capture the tip leakage flow, 8 elements are distributed in the blade tip clearance. Since the grid size and

normalized distance y^+ between the first grid layer and the boundary have remarkable influence on the CFD based numerical results [54][55], the grid independency check of numerical models has also been performed. As shown in Table 3-2 which summarizes the grid-dependency of the calculated head and efficiency of the RR3-type rotors. It is found that the cases with nodes over about 1 million and average $y+$ below about 12.9, from Case 2 to Case 4, show the similar numerical performance results. Therefore, the meshes for all the CFD models are constructed to have similar resolution to that of the Case 2.

Table 3-2 Grid independency check in CFD simulation

Case	Nodes	Minimum y^+ on blades [-]	Average y^+ on blades [-]	Total Head H_t [m]	Total Efficiency η_t [-]
1	344,734	0.69	12.79	3.86	0.790
2	1,036,672	0.56	12.93	3.95	0.801
3	1,227,700	0.20	6.65	3.96	0.800
4	2,792,830	0.57	12.96	3.98	0.802

In the past study, the significant flow interaction has been experimentally observed between the front and rear rotors of a contra-rotating axial flow pump [56]. Because of the complexity of blade-rows interaction, in the present study, we have tried to remove the effect of blade-rows interaction in the front rotor performance prediction model, while we have included all such interactions in the rear rotor performance prediction model. As will be seen in the results in Section 3.3, this strategy is effective and can well help the proposed model predict the total performances. Therefore, as shown in Fig. 3-3, two types of CFD model are constructed: only front rotor, and the both front and rear rotors. Results of the only-front-rotor CFD model are employed to construct the performance prediction model for front rotor, while those of the both of CFD models (only front rotor, and the both front and rear rotors) are used to establish the

performance prediction model for rear rotor.

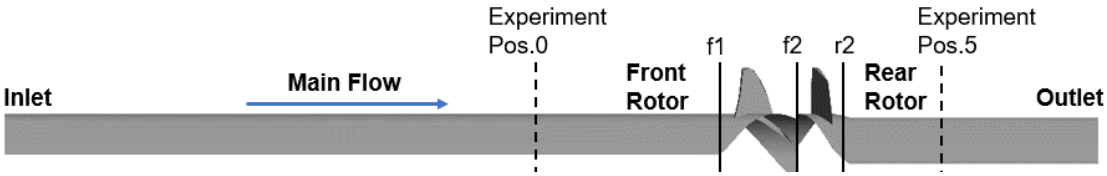

Fig. 3-4 Positions of performance evaluation

3.2.3.2 Accuracy of CFD simulations

Experiments of contra-rotating axial flow pump have been conducted in the past studies [38][39], and the detailed information on the experimental test rig can be found in [36][57]. It should be noted that, in the experiments, the performances are evaluated from the casing-average static pressure at Pos. 0 and Pos. 5 (shown in Fig. 3-4) and the torques of the rotors. For the direct comparison of the performance with experiment, the head in CFD analysis is also evaluated using the casing-average static pressure at the same positions as in the experiment.

Figure 3-5 displays the performances of experiments and CFD simulations for RR2-type and RR3-type rotors operated with the design rotational speeds. It can be easily found that, significant discrepancies occur in the head evaluations at very low flow rates which may arise from errors of the steady calculation. Small discrepancies near the design flow rates seem to be the result of over evaluated losses due to the mixing plane applied between the front and rear rotor domains. Actually, it has been shown that the unsteady simulation of full rotors which can properly take account of rotor-rotor interaction improve the accuracy of performance prediction, realizing much better agreement with experiment [51]. Since the discrepancy between CFD and experiment is still small enough and their tendencies in performance change agree well near the design flow rate, CFD results at the near-design flow rates with design rotational speed will be chosen as the base data for the construction of performance prediction model.

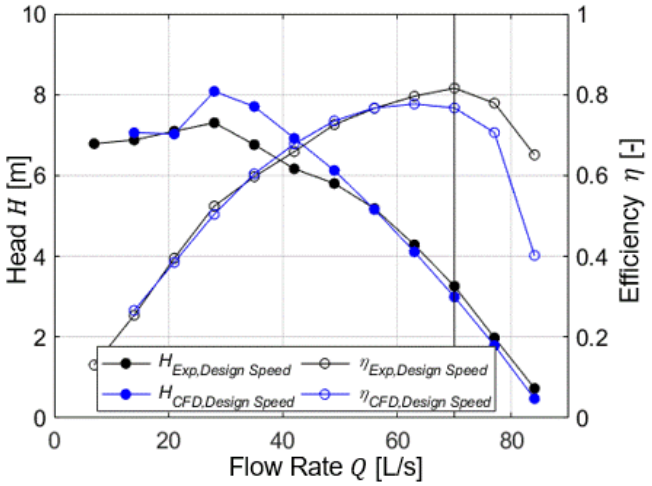

(a) RR2-type rotors

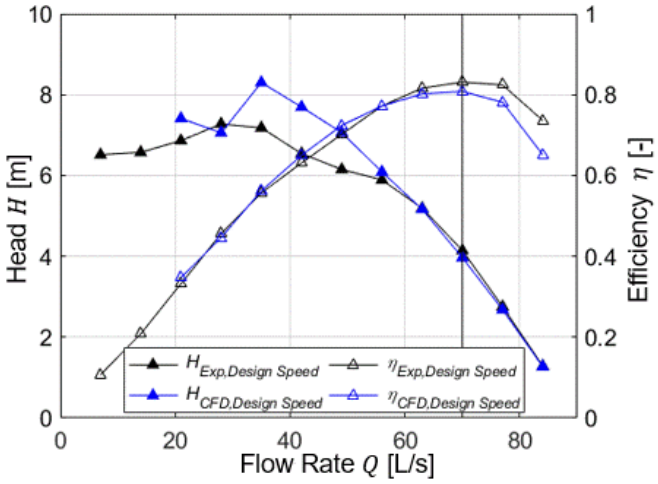

(b) RR3-type rotors

Fig. 3-5 Performances evaluated by experiments and CFD simulations under design rotational speed

3.2.4 Theoretical head prediction

3.2.4.1 Basic equations

In order to simplify the flow in the performance prediction model, the following assumptions are employed: steady flow, negligible viscous losses along the streamtube, axisymmetric flow, no reverse flow, and uniform flow with no swirl at front rotor inlet. Figure 3-6 illustrates the

meridional plane and typical streamtubes in contra-rotating axial flow rotors. At the inlet and outlet of the rotors, a radial equilibrium condition [6] is applied as follows:

$$\frac{dp}{dr} = \rho \frac{v_\theta^2}{r} \tag{3-1}$$

where p denotes the static pressure, r the local radius, ρ the fluid density and v_θ the circumferential component of flow absolute velocity. Since negligible loss is assumed along the streamtube, a rothalpy conservation equation [23] along each streamtube will be:

$$\frac{p_1}{\rho} + \frac{1}{2}w_1^2 - \frac{1}{2}(r_1\omega)^2 = \frac{p_2}{\rho} + \frac{1}{2}w_2^2 - \frac{1}{2}(r_2\omega)^2 \tag{3-2}$$

where subscripts 1 and 2 denote the inlet and outlet of rotors respectively, *w* represents the relative velocity and ω is the angular rotational speed of the considered rotor. The local mass conservation in the streamtube can be written as follows:

$$v_{a1} r_1 dr_1 = v_{a2} r_2 dr_2 \tag{3-3}$$

where v_a means the axial velocity. Furthermore, in order to determine the velocities, the exit flow angle β_2 is also necessary and can be expressed as $\beta_2 = \beta_{b,2} + \delta$, where $\beta_{b,2}$ and δ are the blade exit angle and the deviation angle respectively.

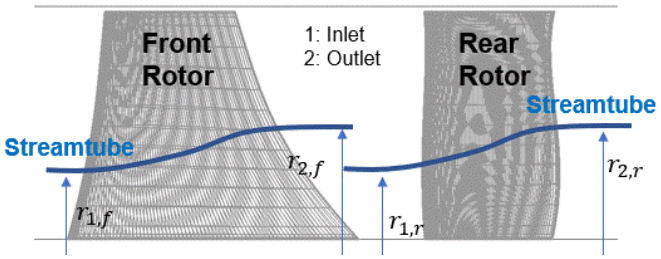

Fig. 3-6 Streamtubes assumed in contra-rotating axial flow rotors

An empirical deviation angle equation [41] is introduced here:

$$\delta = \delta_{ref} + k(i - i_{ref}) \tag{3-4}$$

where i denotes the incidence angle, and δ_{ref} and i_{ref} mean the reference deviation angle and reference incidence angle respectively. The empirical coefficient *k* is related to the inlet flow

angle β_1 and solidity σ, the detail of which can be found in Fig. 3-7. The reference angles δ_{ref} and i_{ref} are selected as the angles at the design flow rate with the design rotational speed which can be derived from the flow database obtained by CFD.

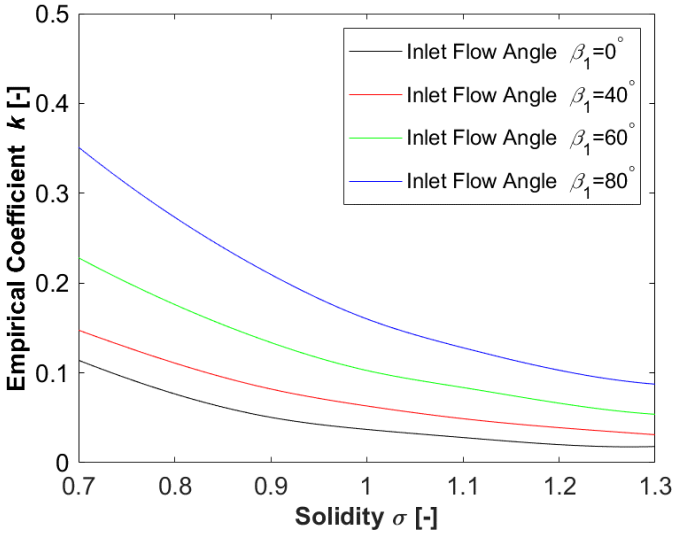

Fig. 3-7 Empirical coefficient for deviation angle (reproduced from Lieblein [41])

Together with Eqs. (3-1)-(3-4), by using velocity triangles of front and rear rotors, the following differential equation on axial velocity at rotor outlet dv_{a2}/dr_2 is derived:

$$\frac{dv_{a2}}{dr_2} = \cos^2\beta_2\left\{2\omega\tan\beta_2 - \frac{\tan\beta_2}{\cos^2\beta_2}\frac{d\beta_2}{dr_2}v_{a2} + \frac{1}{r_1}\frac{dv_{a1}}{dr_1}r_2 - \tan^2\beta_2\frac{v_{a2}}{r_2} + \frac{r_2}{v_{a1}r_1}\left[\frac{dp_1}{\rho dr_1} + (v_{\theta 2} + \omega r_1)\frac{dv_{\theta 1}}{dr_1} + \omega v_{\theta 1}\right]\right\} \tag{3-5}$$

This equation is the ordinary differential equation and can be easily solved numerically with sufficient accuracy. The axial velocity is calculated in the 2nd order precision using Taylor's series, and the other velocities are determined with the velocity triangles at the inlet and outlet of front and rear rotors. Finally, the theoretical head of each rotor can be calculated by the following equation:

$$H_{th} = \frac{T\omega}{\rho g Q} = \frac{\omega}{gQ}\int (r_2 v_{\theta 2} - r_1 v_{\theta 1})\, dQ \cong \frac{\omega}{gQ}\int_{r_{hub}}^{r_{tip}} (r_2 v_{\theta 2} - r_1 v_{\theta 1}) 2\pi r_1 v_{a1} dr \qquad (3\text{-}6)$$

where T denotes the torque of rotors, g is the gravitational acceleration, r_{tip} and r_{hub} mean the radius at blade tip and the hub respectively. Equation (3-6) can be integrated numerically using the velocities in the streamtubes from hub to tip at outlet of rotor.

3.2.4.2 Blade-rows interaction modification

To validate the prediction of theoretical head described above, the theoretical head is evaluated from the mass-averaged total pressure at the rotor-adjacent cross sections f1, f2 and r2 (shown in Fig. 3-4) using the base flow data provided by CFD. Figure 3-8 (a) illustrates the theoretical head evaluated by CFD and the calculation with above equations near the design flow rates with the design rotational speed. In addition to RR2 type, the prediction of theoretical head (Euler head) of RR3 type is also compared with CFD. In the both two types, good agreement is basically seen in the predictions of all rotors, while, if we look closely at the rear rotor especially for RR2, un-ignorable discrepancies still exist. It should be noted that, the CFD results of front rotors are obtained using the numerical model of only front rotor, while those of rear rotors are obtained using the model considering the both front and rear rotors. Furthermore, significant blade rows interactions have been experimentally observed between the front and rear rotors of contra-rotating axial flow pump in the past study, especially in the RR2-type rotors [56]. Therefore, such discrepancy in the theoretical head prediction of rear rotor seems to be due to the remarkable blade-rows interactions; actually they are not considered in the theoretical head prediction as can be seen in its formulation described above.

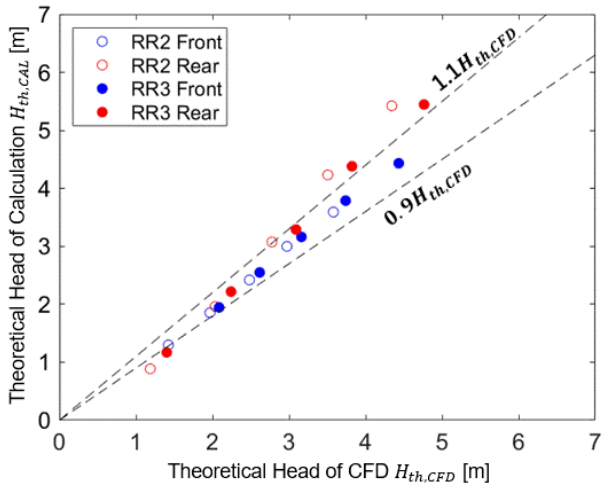

(a) Theoretical head prediction

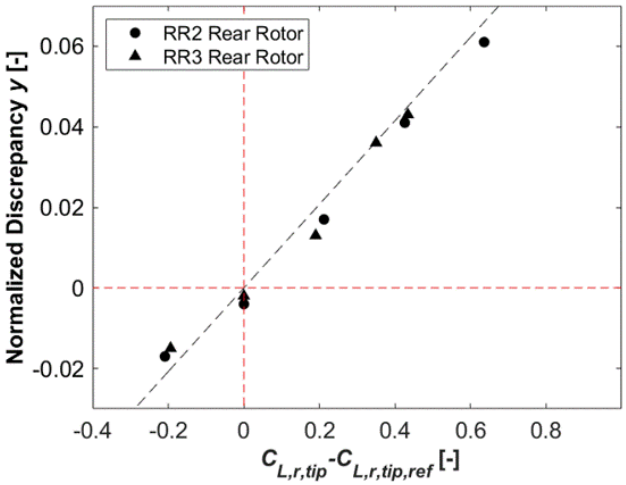

(b) Normalized discrepancy in theoretical head of rear rotor

Fig. 3-8 Theoretical head predictions and their normalized discrepancy in rear rotor

Cao et al. [56] have found that the flow field generated by the rear rotor has a significant influence on the flow around the front rotor because of the large stagger angle of rear rotor which comes from the rotor design considering the exiting swirling flow from the front rotor. The low-pressure region on the suction surface of rear rotor extends into the blade passage of front rotor, which becomes more significant at lower flow rates than at the design one. Furthermore, Zhang

et al. [58] have observed the unsteady vortex behaviors in tip region between front and rear rotors at low flow rates, which is caused by the interaction of backflow from the rear rotor tip with mainstream from the front rotor. Therefore, it seems possible to correlate the lift coefficient of rear rotor blade at tip with the discrepancy of theoretical head prediction, which is expected to help us to improve the theoretical head prediction.

The lift coefficient C_L can be simply derived from the momentum and energy conservation laws of the flows in the cascade, considering the axial velocity change from the inlet to the outlet [59]:

$$C_L = \frac{2}{\sigma}\left\{\left(1-\frac{\xi}{2}\right)\tan\beta_1 - \left(1+\frac{\xi}{2}\right)\tan\beta_2\right\}\cos\beta_m - C_D\tan\beta_m \tag{3-7}$$

where ξ denotes the axial velocity change ratio defined with the inlet and outlet axial velocities as $\xi = 2\,(v_{a2}-v_{a1})/(v_{a2}+v_{a1})$, β_m is the average flow angle determined from $2\tan\beta_m = (1-\xi/2)\tan\beta_1 + (1+\xi/2)\tan\beta_2$, and C_D is the drag coefficient. The drag coefficient is expressed as follows, using the cascade loss coefficient ζ_c (introduced by Eq. (3-9) in Section 3.2.5.1).

$$C_D = \frac{1}{\sigma}(1-\frac{\xi}{2})^2\zeta_c\frac{\cos^3\beta_m}{\cos^2\beta_1}$$

Figure 3-8 (b) shows the normalized discrepancy of the theoretical head prediction plotted against the difference of tip lift coefficient from that at the reference, i.e. at the design flow rate with design rotational speed. The normalized discrepancy *y* is defined as:

$$y = g\frac{H_{th,r,model} - H_{th,r,CFD}}{(\omega_r r_{tip})^2}$$

where $H_{th,r,model}$ denotes the rear rotor theoretical head calculated by the performance prediction model without considering the blade-rows interactions, $H_{th,r,CFD}$ is the rear rotor theoretical head calculated by CFD, and r_{tip} means the radius of blade tip. As displayed in Fig. 3-8 (b), an approximated linear relation can be clearly observed between the normalized

discrepancy y and the difference of rear rotor tip lift coefficient $C_{L,r,tip} - C_{L,r,tip,ref}$ as $y = 0.1037(C_{L,r,tip} - C_{L,r,tip,ref})$ for the both RR2 and RR3 rear rotors. In this equation, $C_{L,r,tip,ref}$ is the reference tip lift coefficient of rear rotor at design flow rate under design rotational speed, and it is also calculated with Eq. (3-7). Finally, the predicted theoretical head of rear rotor $H_{th,r}$ with considering the blade rows interaction modification will be:

$$H_{th,r} = H_{th,r,model} - 0.1037(C_{L,r,tip} - C_{L,r,tip,ref})\frac{(\omega_r r_{tip})^2}{g} \tag{3-8}$$

3.2.5 Loss models

In the present study, the flow losses in the performance prediction model is divided simply into two parts: cascade loss and other losses. The cascade loss is directly evaluated by employing an empirical cascade loss model [42]. On the other hand, the other losses are modelled with referring to the blade tip lift coefficient.

3.2.5.1 Empirical cascade loss

According to Lieblein's paper [42], the empirical cascade loss coefficient ζ_c is given by:

$$\zeta_c = 2(\frac{\delta_{m2}}{l})\sigma\frac{\cos^2\beta_1}{\cos^3\beta_2}\left\{\frac{2.16}{2.24}/[1-(\frac{\delta_{m2}}{l})\frac{1.08\sigma}{\cos\beta_2}]^3\right\} \tag{3-9}$$

where the loss coefficient ζ_c is defined with total pressure loss $p_{t,loss}$ and inlet relative velocity w_1 as $\zeta_c = 2p_{t,loss}/(\rho w_1^2)$. (δ_{m2}/l) denotes momentum thickness coefficient which is calculated by

$$\left(\frac{\delta_{m2}}{l}\right) = \begin{cases} 0.004/\left(1 - 1.17lnD_{eq}\right) & D_{eq} \le 2 \\ 0.004/(1 - 1.17ln2) + 0.11\left(D_{eq} - 2\right) & D_{eq} > 2 \end{cases}$$

where D_{eq} is the equivalent diffusion factor. It should be noted that the equation with $D_{eq} > 2$ has been added to well achieve the loss calculation convergence.

The cascade loss can be locally calculated at every radial location, and then the mass-averaged

cascade loss head $H_{loss,cascade}$ is determined by:

$$H_{loss,cascade} = \frac{1}{2gQ}\int w_1^2 \zeta_c dQ = \frac{1}{2gQ}\int_{r_{hub}}^{r_{tip}} w_1^2 \zeta_c 2\pi r_1 v_{a1} dr \qquad (3\text{-}10)$$

In order to compare with cascade loss model, local losses in CFD simulations are also evaluated by subtracting the local head rise from the local theoretical head at each radial location. Figure 3-9 shows the local loss distribution of the front rotor predicted by the cascade loss model and the CFD at 90% and 110% of the design flow rate. It is easily found that the loss model well predicts the local loss in the region from the hub to mid-span while the significant discrepancy occurs in the tip region, which may be the result of tip clearance effect.

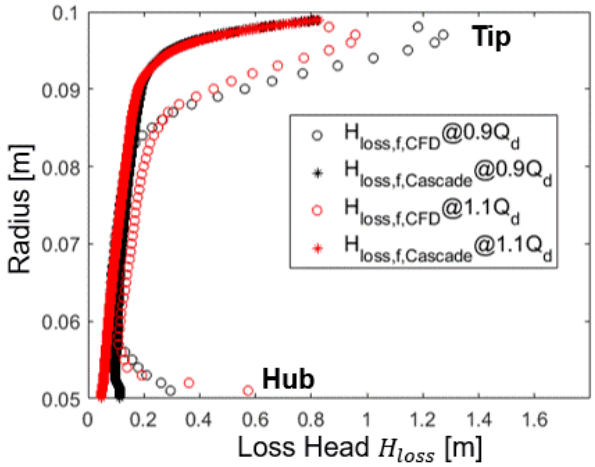

Fig. 3-9 Cascade loss distribution of front rotor evaluated by performance prediction model compared with local flow losses calculated by CFD simulations

3.2.5.2 Empirical other losses

Lakshminarayana [43] has found that the tip lift coefficient has a strong relation with the losses due to tip clearance effect. It is known that the pressure difference between the pressure and suction surfaces in the blade tip usually causes the leakage flow through the tip clearance. The interactions of tip leakage flow and the mainstream could generate the tip leakage vortex (TLV).

As a result, the blockage effect of TLV contributes significantly to loss generation [53][60]. It should be noted that the pressure difference in the blade tip can be related to the blade tip lift coefficient. Therefore, in this section, assuming that tip clearance effect is a dominant cause in the other losses, the losses is herein modelled on the basis of blade tip lift coefficient.

In order to derive the empirical equation for losses except the cascade loss, the total head loss in CFD simulation is evaluated for the both RR2- and RR3-types under the conditions with the design rotational speed near the design flow rate, considering the control volumes defined with f1, f2 and r2 cross sections illustrated in Fig. 3-4. The total head and the head loss can be obtained by the following equations.

$$H_{CFD} = \frac{1}{\rho g Q}\left(\int_{f2\ or\ r2} p_t dQ - \int_{f1\ or\ f2} p_t dQ\right) \tag{3-11}$$

$$H_{loss,CFD} = H_{th,CFD} - H_{CFD} \tag{3-12}$$

The quantity of other losses mainly due to the tip clearance effect is evaluated from CFD loss $H_{loss,CFD}$ by subtracting the cascade loss $H_{loss,cascade}$ evaluated by Eq. (3-10). The other loss coefficient $\psi_{loss,other}$ is defined:

$$\psi_{loss,other} = \frac{2g}{w_{m,tip}^2}(H_{loss,CFD} - H_{loss,cascade}) \tag{3-13}$$

where the tip average relative velocity $w_{m,tip}$ is determined with the relative velocities at inlet $w_{1,tip}$ and outlet $w_{2,tip}$ of the blade tip by $w_{m,tip} = (w_{1,tip} + w_{2,tip})/2$.

Figure 3-10 (a) shows the other loss coefficient calculated by Eq. (3-13) against the tip lift coefficient near the design flow rate with the design rotational speed. It is found that the loss variation is small in the low lift coefficient range, while the rapid change of the loss is found in the range of high lift coefficient. We can also find that the other losses in RR2-type rear rotor has much steeper slope compared with RR3-type rear rotor. Therefore, according to the results under the designed rotational speed, the approximated functions for the other loss coefficient in the front

rotor of RR2-type and in the front and rear rotors of RR3-type are written as:

$$\psi_{loss,other} = \begin{cases} 0.0176C_{L,tip} + 0.0152 & C_{L,tip} \leq 0.45 \\ 0.16C_{L,tip} - 0.0489 & C_{L,tip} > 0.45 \end{cases} \quad (3\text{-}14)$$

For RR2-type rear rotor, the approximated function is written as:

$$\psi_{loss,other} = \begin{cases} 0.0536C_{L,tip} + 0.0187 & C_{L,tip} \leq 0.75 \\ 0.223C_{L,tip} - 0.1084 & C_{L,tip} > 0.75 \end{cases} \quad (3\text{-}15)$$

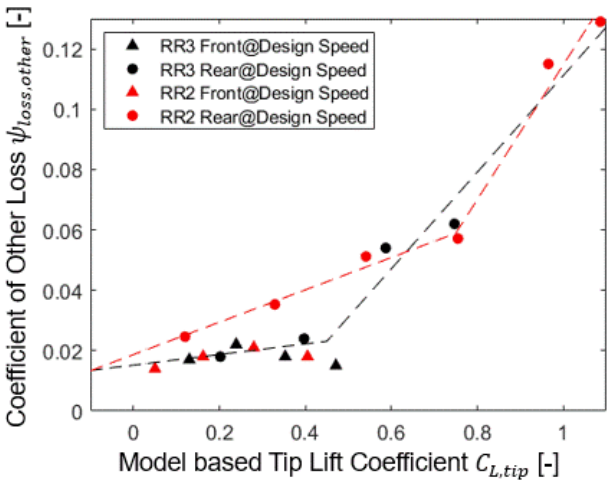

(a) Design rotational speed

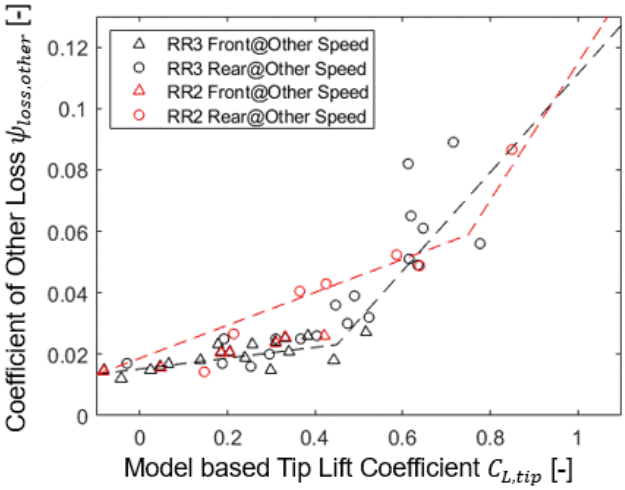

(b) Other rotational speed

Fig. 3-10 Model derivation of other losses including tip clearance loss

In Fig. 3-10 (b), the other loss coefficient in many conditions with the off-design rotational speeds are also plotted against the tip lift coefficient. It can be found that Eqs. (3-14) and (3-15) still well hold in the all examined off-design speed cases. Finally, the total loss quantity H_{loss} is determined with the empirical cascade loss coefficient ζ_c and the empirical other loss coefficient $\psi_{loss,other}$:

$$H_{loss} = \frac{1}{2gQ}\int w_1^2 \zeta_c dQ + \frac{1}{2g} w_{m,tip}^2 \psi_{loss,other} \tag{3-16}$$

3.2.6 Scheme of the calculation

A MATLAB code is constructed to solve the above set of equations. Figure 3-11 illustrates an overall flowchart of the performance prediction model proposed in this study. In the front rotor calculation, the uniform axial velocity without pre-swirl is assumed at the inlet, and therefore the inlet axial flow velocity is determined from the volumetric flow rate $Q_{f1.}$ After the determination of deviation angle δ_f and exit flow angle β_{f2}, according to Eq. (3-5), the radial gradient of exit axial velocity $dv_{a,f2}/dr$ can be calculated. Since the iterative procedure is needed to find the solution satisfying the above equations, some initial condition for exit axial velocity at the tip $v_{a,f2,tip}$ is necessary. Here, it is assumed to be 2 times of the area averaged axial velocity. Then, the flow rate at front rotor outlet Q_{f2} become available. Then, the given tip axial velocity at front outlet is modified until the mass conservation at front rotor inlet and exit, i.e. $Q_{f2} = Q_{f1}$, will be achieved. Assuming that the interaction between front and rear rotors is negligible under good rotational speed control condition, the calculation of rear rotor can be conducted similarly to that in front rotor by using front rotor exiting flow as inlet boundary condition. Flow velocities can be determined using velocity triangles in front and rear rotors. Finally, the empirical losses and modifications are also calculated and are used to evaluate total performances in contra-rotating axial flow pump. It should be noted that the blockage effect due to casing wall boundary layer

which may have some impact on rotor performances is not considered in this calculation for the sake of simplicity.

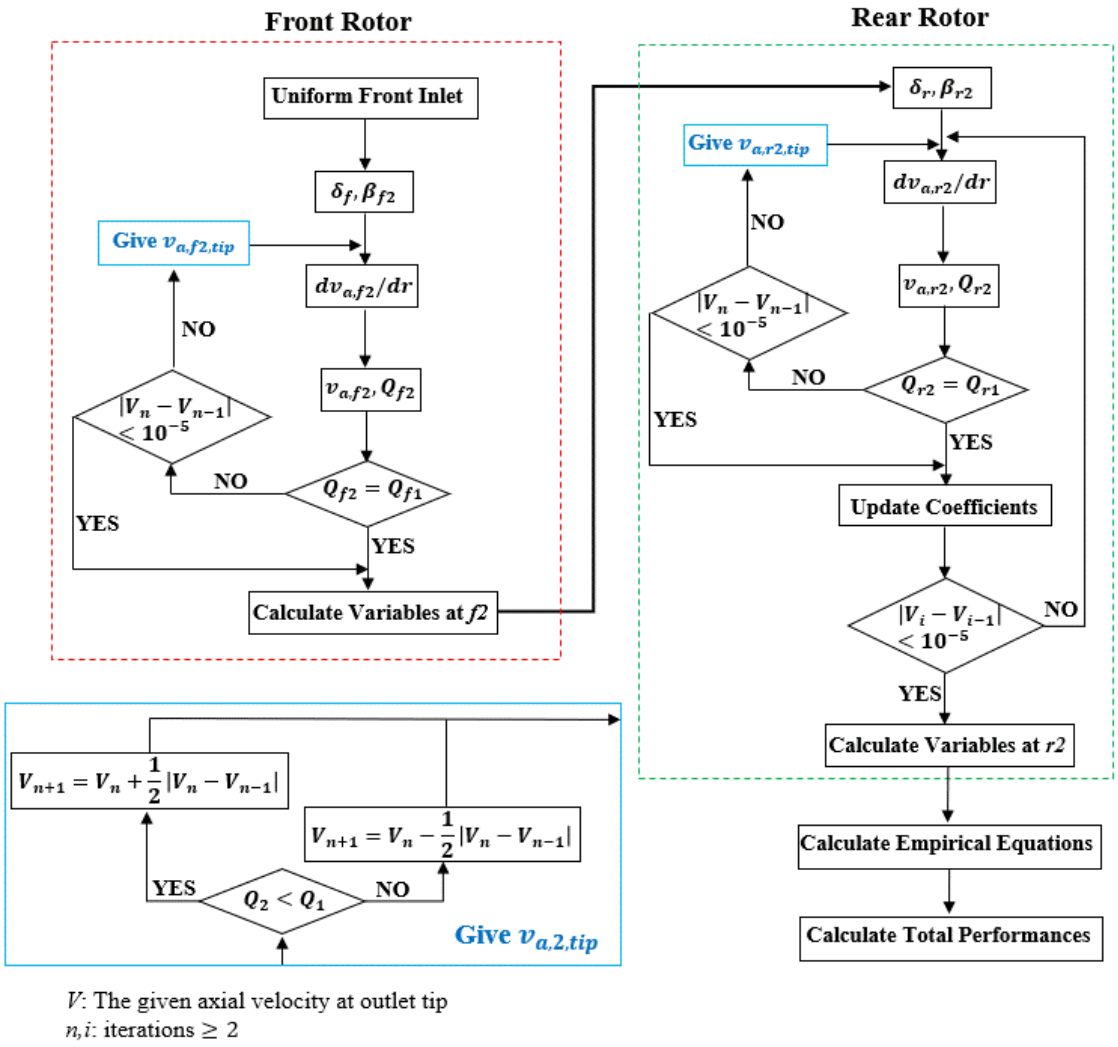

Fig. 3-11 Calculation flow in the model

3.2.7 Performance predictions

Using the above equations, the theoretical head H_{th} and the loss quantity H_{loss} can be determined. The head H and the efficiency η are finally predicted by the following equations.

$$H = H_{th} - H_{loss} \tag{3-17}$$

$$\eta = H/H_{th} \tag{3-18}$$

In order to examine the accuracy of performance prediction model, CFD simulations are conducted at various flow rates with off-design rotational speeds. Figure 3-12 displays the predicted head and efficiency of whole rotors as well as those calculated by CFD. It is found that the almost all predictions are located in the range from 90% to 110% of CFD results, indicating the good enough accuracy of performance prediction model.

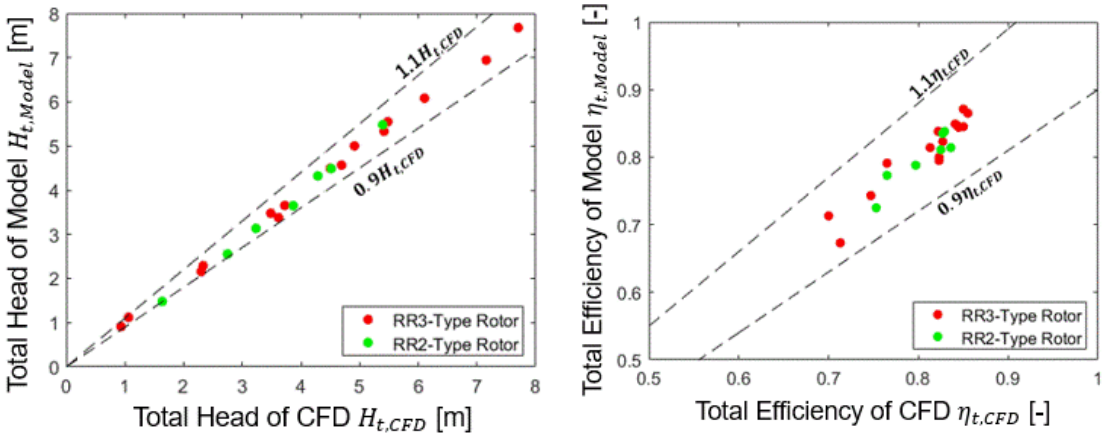

(a) Total head (b) Total efficiency

Fig. 3-12 Performances evaluated by performance prediction model and CFD at various flow rates with off-design speeds

3.3. Results and discussion

3.3.1 Rotational speed control of each rotor

In the past study [40], rotational speed control (RSC) has been experimentally applied in the front and rear rotors of a contra-rotating axial flow pump with RR2-type rotors. The control information of rotational speed of rotors is illustrated in Fig. 3-13 (a), where the rotational speed of each rotor is normalized by the designed one, i.e. $N_d(= N_{d,f}, N_{d,r})$ =1225 min^{-1}. The FR method means only controlling the rotational speed of front rotor, while RR method means only

controlling that of rear rotor. At higher flow rates including the designed one (Q_d =70L/s), the internal flow of the front rotor is usually smooth similar to the conventional rotor in rotor-stator type axial flow pump, and therefore only RR method is still effective for the performance improvement. On the other hand, at the low flow rates where the flow recirculation forms at the inlet tip and/or the outlet hub of the front rotor, the performance of the front rotor is significantly deteriorated so that the front rotor speed control (FR) is necessary for the improvement. The results of performance prediction model under rotational speed controls (FR and RR) are compared with those obtained by experiments and CFD simulations in Fig. 3-13. In the experiments, the pump performance is evaluated from the measurements of casing-average static pressure and torques of rotors, while the performance prediction model considers the input and output energy of the flow into rotors by using mass-averaged total pressure and mass-averaged theoretical head. The CFD simulation can evaluate the performance in the both experimental and model's methods. Therefore, the performances evaluated by the experiment and the model prediction are compared in the following way. Figure 3-13 (b) displays the performances evaluated by the experiments and CFD using the experimental method, while Fig. 3-13 (c) illustrates the performances evaluated by CFD and predicted by the proposed model in the model's method. In Fig. 3-13 (b), fairly good agreement is confirmed in the head and efficiency evaluated by experiment and CFD, suggesting us that the results of CFD are acceptable to be used for the validation of the proposed prediction model. The small discrepancy seems to be due to the limitations of steady one-pitch simulation (mixing plane and steady assumption), which is expected to be minimized by conducting the unsteady simulation considering the full pitch (the whole flow passages) of the both front and rear rotors. In Fig. 3-13 (c), we can find the negligible discrepancy between the results of CFD and model near the design flow rate, and the small discrepancy is observed only at extreme off-design flow rates, which means that the proposed

model offers good prediction accuracy. However, it should be noted that the proposed model cannot calculate the flows at very low flow rates (Q <21L/s in this case), where the unfavorable back flow phenomena may be unavoidable even with the rotational speed control (RSC).

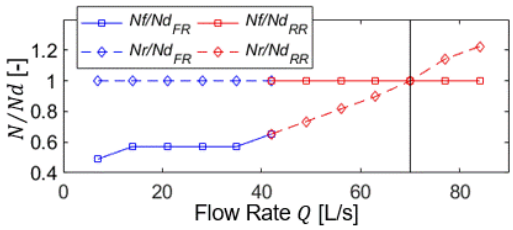

(a) Rotational speeds of front and rear rotors under RR and FR control methods

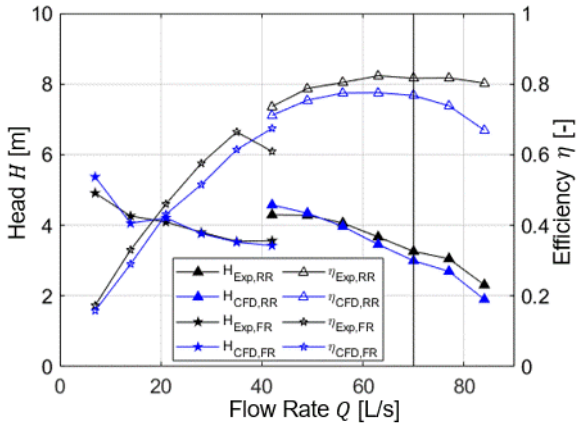

(b) Experiment and CFD (using experimental performance evaluation method)

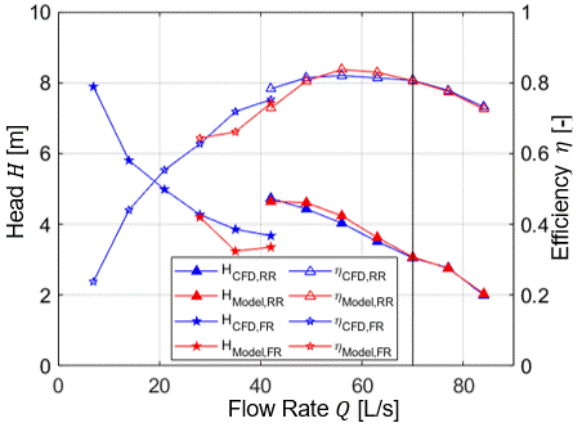

(c) CFD and model (using model performance evaluation method)

Fig. 3-13 Performance evaluations of experiments, CFD simulations and model predictions for RR2-type rotor

3.3.2 Energy saving application

3.3.2.1 System resistance consideration: problem setting

In Fig. 3-13, the rotational speed control (RSC) was applied in the RR2-type front and rear rotors without considering the resistance of pump system. Since the pump operation point is determined by the pump head curve and system resistance curve, it is necessary to consider the system resistance curves in actual operations [61]. The system resistance characteristics H_R is generally expressed by the following equation.

$$H_R = H_0 + \zeta_s Q^2 \tag{3-19}$$

where H_0 is the necessary head of pump which should be specified depending upon the application, ζ_s denotes the system resistance coefficient, and Q means the volumetric flow rate in $[\mathrm{m}^3/\mathrm{s}]$. In the present paper, two pump system resistances H_R are assumed as follows:

System resistance 1: $H_0 = 0\mathrm{m}$ and $\zeta_s = 1200\,\mathrm{s}^2/\mathrm{m}^5$

System resistance 2: $H_0 = 3\mathrm{m}$ and $\zeta_s = 166\,\mathrm{s}^2/\mathrm{m}^5$

Figure 3-14 shows the simplified image of assumed pump systems and their resistance curves. Figure 3-14 (a) corresponds to the case in which the pump is operated in a closed circuit, while Figure 3-14 (b) does to the case in which the pressurized liquid is necessary, which can be often seen in practical applications. It should be noted that the tanks in Fig. 3-14 are large enough so that water surface levels in them are kept constant regardless of the flow rate.

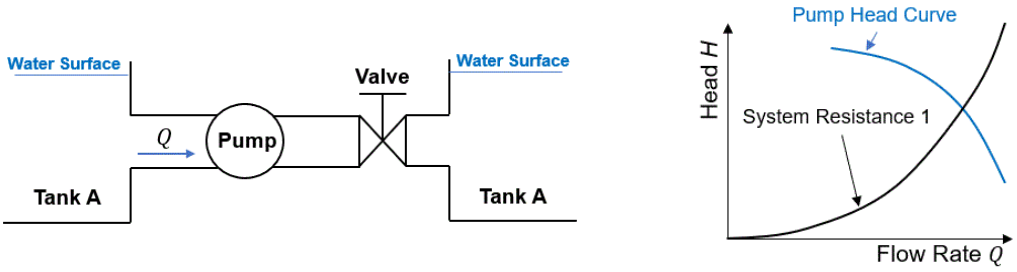

(a) System 1: a closed circuit

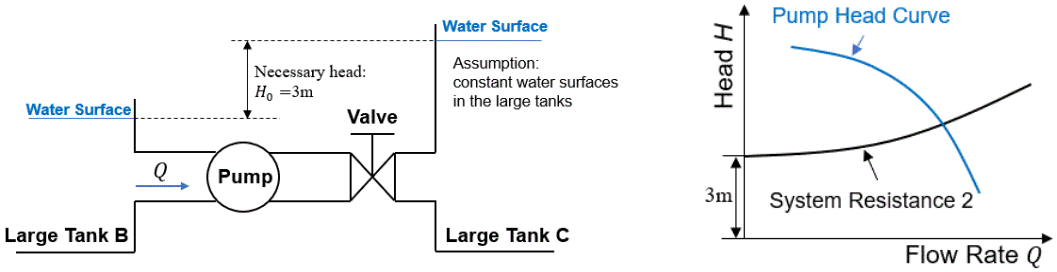

(b) System 2: pressurized liquid

Fig. 3-14 Sketches of pump systems and their resistance curves

3.3.2.2 Optimum operation determination

To maximize the global energy saving for the given system resistances, the input power to the pump should be minimized for the specified flow rate, while keeping the pump head larger than the system resistance head. The input power means the shaft power ($L = \rho g Q H_{th}$), therefore the problem is now to minimize the theoretical head H_{th} under the condition of $H \geq H_R$. The optimum rotational speeds of the front and rear rotors should be determined to satisfy this condition. Since the proposed performance prediction model under rotational speed control (RSC) of rotors is very simple, we can find the optimum speeds easily in the following way.

Firstly, the proposed model is applied to predict the performances within a wide rotational speed range of front and rear rotors in every 20min^{-1} step. Then, according to the system resistances, we select all combinations of the front and rear rotor speeds with high efficiency among the speed combinations with which the pump head satisfies the required resistance head.

Finally, the performances are locally approximated with the 2nd order of Taylor's series by using the model predicted data. The optimum operation points are the conditions satisfying the resistance head with minimum theoretical head at each flow rate in the approximated performances. Figure 3-15 shows the rotational speed information of the front and rear rotors, which are normalized by the design rotational speed of each rotor. Since the prediction errors may exist in the proposed model, more operations near the optimum performance ($H_{opt} \pm 0.5\%$ and $H_{th,opt} \pm 0.5\%$) are also predicted. Their upper and lower limits of the rotational speeds are plotted with the '+' symbols in Fig. 3-15. As shown in Fig. 3-15 (a), the optimal rotational speeds of front and rear rotors linearly decrease with the decrease of flow rate for System resistance 1. The speed ratio of the front and rear rotors is almost constant regardless of flow rate, which implies the flow similarity in the front and rear rotors at each flow rate. It is not surprising since the necessary head rise is $H_0 = 0\mathrm{m}$ in System resistance 1 and the resistance head is purely proportional to the flow rate squared; in such case, the control theory should be the same as that of conventional rotor-stator type axial flow pump, and the head coefficients of the both rotors are constant with the maximum total efficiency. In Fig. 3-15 (b) for System resistance 2, the optimum rotational speeds of front and rear rotors linearly decrease with the increase of flow rate near the design flow rate, whereas the speed ratio of the front and rear rotors is not constant. In addition, at low flow rates, some complex control is necessary to obtain the good energy performance. Therefore, it can be mentioned that the proposed model will be very necessary and useful to determine the optimum operation points in those conditions.

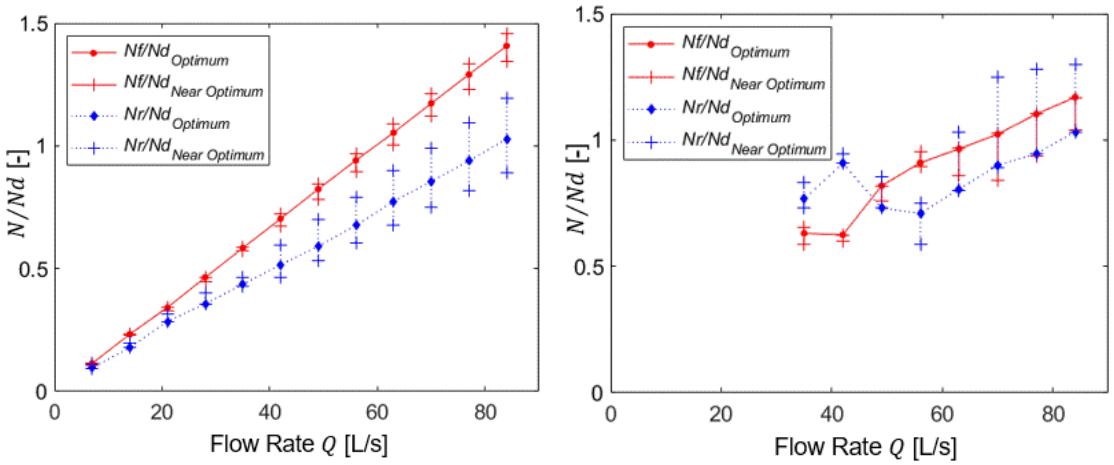

(a) System resistance 1 (b) System resistance 2

Fig. 3-15 Rotational speed information for optimum and near-optimum performances for two system resistances

In summary, it is found that the favorable operations (including optimum and near-optimum) can be determined by the proposed model in very broad flow rate range for System resistance curve 1, while the favorable operations can only be decided by the proposed model in a limited flow rate range for System resistance curve 2. As mentioned above, the performance prediction model can only be used in the conditions where no reverse flow occurs. The reverse flow may be unavoidable in the conditions with high pressure rise at very low flow rates. Actually, in Fig. 3-15 (b), there are no plots at the flow rates lower than 35L/s, since it was not possible to determine the optimum rotational speeds by the proposed prediction method. At such flow rates, the low energy performance is unavoidable with the low efficiency operation of the pump and/or the large loss generated by adjusting the valve opening.

3.3.2.3 Performance prediction and their validations

Figure 3-16 summarizes the performances evaluated by the proposed model with the optimum rotational speed of rotors achieved by rotational speed control (RSC). CFD simulations have been also conducted to validate the predictions of the model. RSC is applied with maximizing the valve opening as much as possible to reduce the consumed energy there. The system resistance curve is presented by the dashed curves in the figure, and the equality of pump head with the system resistance indicates that the maximum valve opening is reached. The performances under the design rotational speed (traditional valve control) which are obtained by experiment and CFD are also illustrated to compare with the performances with RSC method. The traditional valve control means that the operational flow rate is adjusted not by RSC but only by the opening of valve installed on the pipeline.

In the both system resistance curves 1 and 2, we can observe very small discrepancies in the head and efficiency curves between the CFD and the proposed model under RSC method (red plots), meaning the good prediction accuracy of the proposed model. It is also found that RSC method could well modify the head to satisfy the resistance curve in the wide flow rate range with significantly improved efficiency in the both system resistance cases. This implies that the large amount of energy could be well saved by using the RSC method.

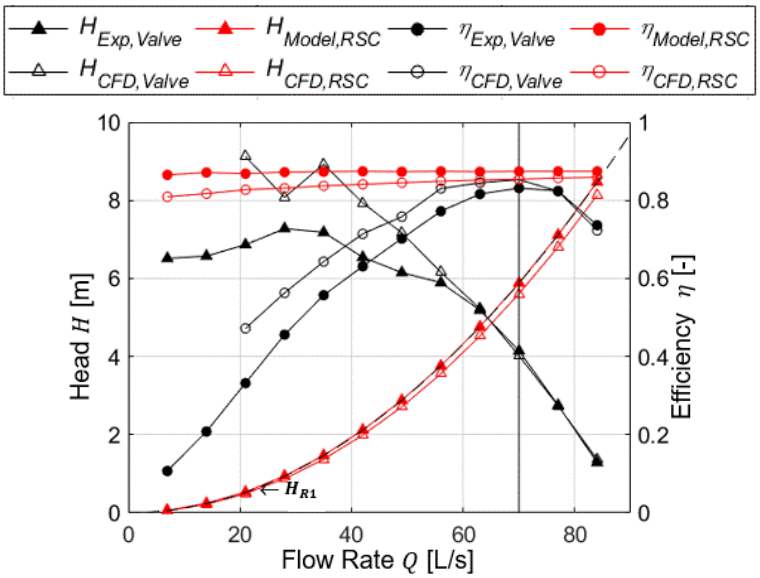

(a) System resistance 1

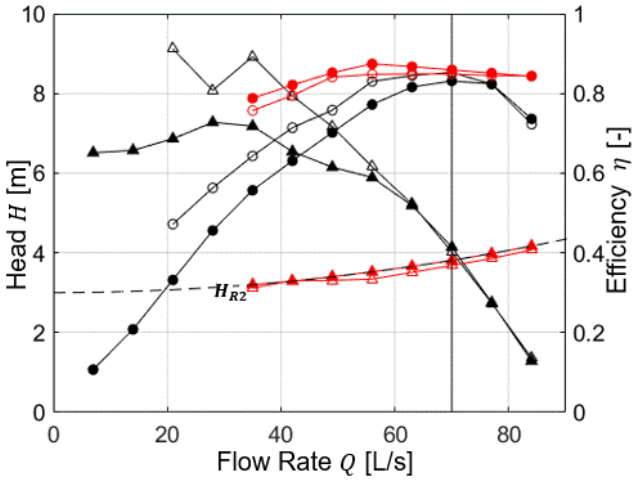

(b) System resistance 2

Fig. 3-16 RR3-type rotor performance curves using valve control (flow rate adjusted by the valve in pipe system under constant rotational speed) and RSC methods

In order to compare the effectiveness of the traditional valve control and RSC methods in terms of energy saving, the system efficiency η_S is defined with the system resistance head H_R and theoretical head H_{th} as

$$\eta_S = \frac{H_R}{H_{th}} \tag{3-20}$$

The system efficiency represents the ratio of system required power and system input power.

Therefore, the larger the system efficiency is, the better energy saving will be achieved. Figure 3-17 shows the system efficiencies under the traditional valve control and RSC methods for the two system resistance curves. As we can see, significantly higher system efficiency can be achieved by RSC method in the wide flow rate range. The traditional valve control shows very low system efficiency at the low flow rates, while the traditional valve control cannot supply enough head to overcome the system resistances at higher flow rates. Such weaknesses of the traditional valve control method can be improved by applying RSC method. Therefore, the RSC offers significant effectiveness in the energy savings at lower flow rates and can extend operation range at higher flow rates.

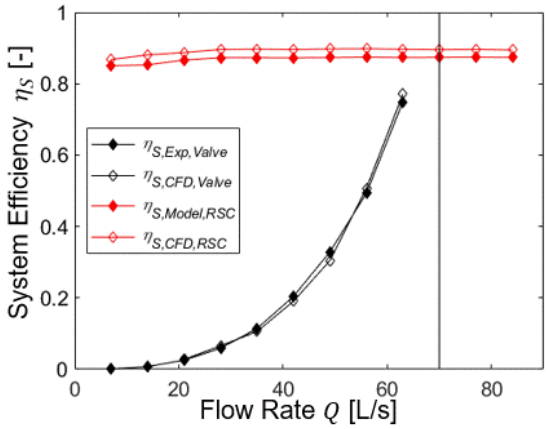

(a) System resistance 1

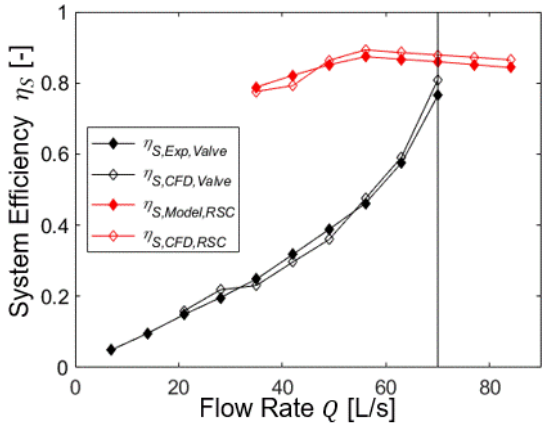

(b) System resistance 2

Fig. 3-17 RR3-type rotor system efficiencies using valve control and RSC methods

3.4 Summary

In the present chapter, a simple and fast performance prediction model for contra-rotating axial flow pump under rotational speed control (RSC) has been established. The results evaluated by the proposed model has been compared with experiments and CFD simulations. Then, energy saving applications of the proposed model has also been illustrated. Main findings are summarized as follows:

1) By considering the radial equilibrium condition, the conservations of rothalpy and mass through streamtubes, the empirical deviation angle, the blade-rows-interaction and the empirical loss equations, a simple performance prediction model has been constructed for the contra-rotating axial flow pump to find the effective RSC method;
2) Through the comparisons with experimental and CFD results, the proposed model has been found to have good enough accuracy in predicting performances of contra-rotating axial flow pump under RSC in a broad flow rate range. On the other hand, the proposed model also shows limitations in the conditions with high-pressure rise at very low flow rates. The occurrence of reversed flow may be unavoidable at such flow rates even with RSC.
3) In the energy saving applications of the proposed model, compared with the traditional valve control method, the RSC method optimized by the proposed performance prediction model can well adjust the pump head to satisfy the system resistance curves at wide flow rate range with significant improvement of system efficiency. Good agreements are obtained between the proposed model and the CFD simulations, showing the effectiveness of the proposed performance prediction model.

Chapter 4

Design optimization of rotors for energy saving with RSC in contra-rotating axial flow pump using performance prediction models and a genetic algorithm

In the previous chapter, the rotational speed control (RSC) has been successfully applied for the previously designed front and rear rotors in contra-rotating axial flow pump using a proposed performance prediction model to satisfy the system resistances at various flow rates with higher efficiencies. However, it is still not known that these rotors of contra-rotating axial flow pump are the best design to achieve the highest energy-saving performance with RSC. Therefore, in this study, the design optimization of rotors in contra-rotating axial flow pump is attempted to achieve the best energy saving design of contra-rotating axial flow pump with the RSC.

In most design optimizations of rotating machines, an approximation model (metamodel) is usually constructed using CFD simulations, and then the optimal design could be determined with an optimization algorithm and the metamodel [45][46]. However, in the design optimization for energy saving with RSC in contra-rotating axial flow pump, there are too many design parameters including blade shape parameters of front and rear rotors and their rotational speeds. It should be noted that the metamodel needs to be established with computationally expensive CFD database, whose numerical precision could be not good enough at far off-design flow rates with off-design rotational speeds. During the construction of performance prediction model of the existing contra-rotating axial flow pumps in the previous chapter, it has been found that some empirical equations established with CFD simulations under design-speed conditions could well predict the performance at various flow rates with various rotational speeds. Therefore, it seems to be

generally possible to construct a performance prediction model using an approximation model with computationally low cost. This means that a fast and effective design optimization of rotors for energy saving with RSC in contra-rotating axial flow pump could be realized.

4.1 Objective of the present chapter

The main objective of this chapter is to re-construct the performance prediction model of contra-rotating axial flow pump and to utilize it to conduct the design optimization of rotors for energy saving with RSC in contra-rotating axial flow pump. Figure 4-1 illustrates a flowchart of this work. To realize this work, the following issues will be solved: construction of performance prediction model, design optimization and rotational speed prediction. In the present chapter, the establishment of performance prediction models will be firstly introduced. Artificial neural network (ANN) is employed to construct the metamodel for the prediction of theoretical head and head loss under the design rotational speeds of rotors. CFD simulations are also employed to train the metamodel and also to validate the performance prediction model combined with the trained metamodel. Then, a genetic algorithm (GA) method is employed to help select the optimal design. Finally, a specific application is considered to conduct the design optimization of rotors (only rear rotor, both of front and rear rotors) in contra-rotating axial flow pump.

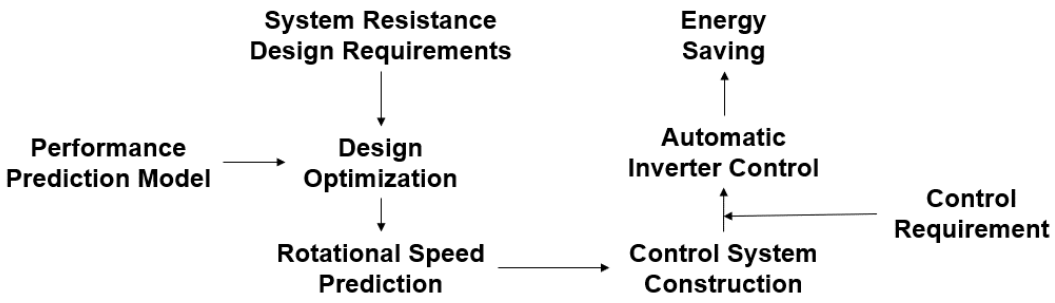

Fig. 4-1 A brief framework of design optimization to reach energy saving

4.2 Performance prediction models including artificial neural network (ANN)

Because of the significantly expensive database to train an appropriate metamodel toward the design optimization of rotors for energy saving with RSC in contra-rotating axial flow pump, a performance prediction model with a low-cost metamodel is very necessary.

4.2.1 Overall strategy

As illustrated in Fig. 4-2, our main strategy is to use the CFD results under conditions with design rotational speed for the prediction of performances under conditions with off-design rotational speeds. CFD simulations with various blade shapes will be only conducted at near-design flow rates ($0.8Q_d$~$1.1Q_d$) with design rotational speed to construct a metamodel. It should be emphasized that the metamodel is trained with less computational expensive database whose numerical accuracy is also good enough. Then, combining with flow velocities determined by basic equations (radial equilibrium equation, rothalpy conservation equation, mass conservation equation and empirical deviation angle equation), empirical equations related to theoretical head (Euler head) and other losses will be constructed using the design-speed performance predicted by the metamodel. Finally, performance at various flow rates with various rotational speeds could be determined by using theoretical head and loss head. The following parts will give the detailed description of the performance prediction model.

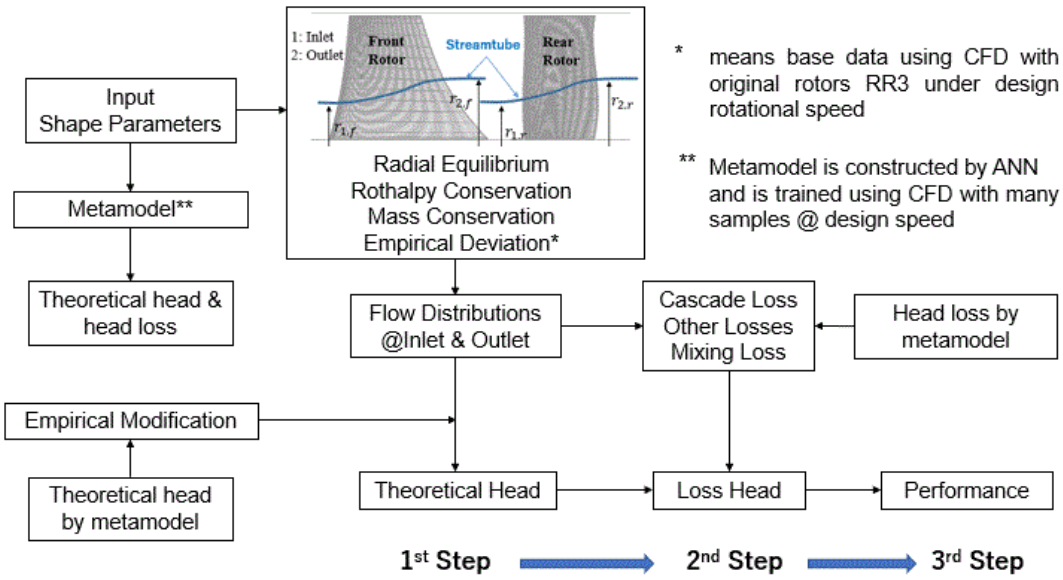

Fig. 4-2 A strategy to predict performance

4.2.2 Original rotors

The RR3-type rotors designed in the past study [38] are employed for the baseline to conduct the design optimization. Figure 4-3 shows the geometries of front and rear rotors of RR3. The design flow rate is 70L/s, and the design total head is 4m. The front and rear rotors are designed with same specific speed: $N_{s,f} = N_{s,r} = 1500[\mathrm{min}^{-1}, \mathrm{m}^3/\mathrm{min}, \mathrm{m}]$. The blade number of front and rear rotors are 4 and 5 separately, and their design rotational speeds are $1311[\mathrm{min}^{-1}]$ and $1123[\mathrm{min}^{-1}]$ respectively. The diameter of casing is 200mm, while the blade diameter is 198mm. As a result, the tip clearance is 1mm. The detailed design parameters of the original rotors are summarized in Table 4-1.

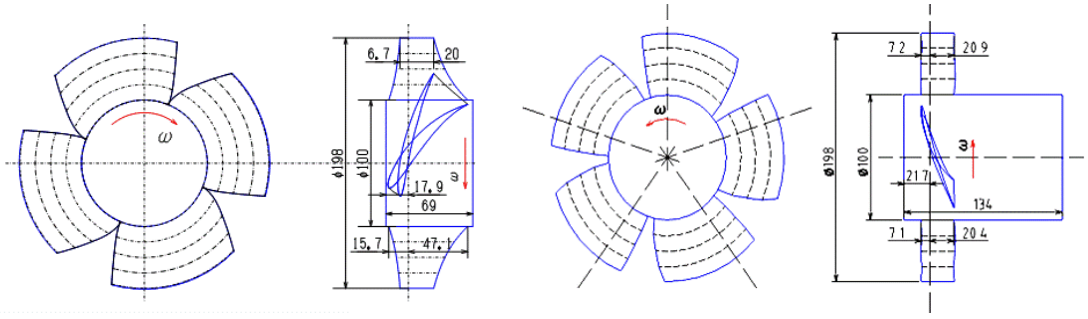

(a) RR3-type front rotor (b) RR3-type rear rotor

Fig. 4-3 Shapes of original rotors

Table 4-1 Design specifications of RR3-type rotors

Casing Diameter D_c [mm]		200		
Blade Diameter [mm]		198		
Hub Diameter D_h [mm]		100		
Hub Ratio D_h/D_c [-]		0.5		
Tip Clearance [mm]		1		
Design Flow Rate Q_d [L/s]		70		
Design Total Head $H_{t,d}$ [m]		4		
		Hub	Mid-span	Tip
	Diameter [mm]	100	149	198
Front Rotor	Rotational Speed [min^{-1}]	1311		
	Specific Speed $N_{S,f}$	1500 [min^{-1}, $\mathrm{m}^3/\mathrm{min}$, m]		
	Blade Number	4		
	Hydrofoil	NACA4410	NACA4408	NACA4406
	Solidity σ [-]	1.290	0.898	0.700
	Stagger Angle γ [°]	51.72	68.48	75.85
Rear Rotor	Rotational Speed [min^{-1}]	1123		
	Specific Speed $N_{S,r}$	1500 [min^{-1}, $\mathrm{m}^3/\mathrm{min}$, m]		
	Blade Number	5		
	Hydrofoil	Special shapes [38]		
	Solidity σ [-]	1.008	0.864	0.720
	Stagger Angle γ [°]	64.95	69.73	71.88

4.2.3 CFD analysis for base data

In this chapter, CFD simulations are conducted under conditions with design rotational speed to obtain the base data for the establishment of metamodel which will be used to predict the theoretical head and head loss of newly designed front and rear rotors operated at the design speed. The CFD simulations are also used to validate the performance prediction model in conditions with rotational speed control (RSC). A commercial CFD code, ANSYS CFX 2019 R3, is employed.

Even though the performance and internal flow in a contra-rotating axial flow pump have been well calculated at very broad range of flow rate by solving unsteady Reynolds-Averaged Navier-Stokes (RANS) equations in whole passages of front and rear rotors [52], the computation cost is too expensive to construct a database for the metamodel. On the other hand, steady RANS based simulations of only one passage of front and rear rotors in contra-rotating axial flow pump show good enough accuracy in conditions under design rotational speed near design flow rate with reasonable time consumption (as shown in Chapter 3). Therefore, the steady CFD analysis is again conducted in the present chapter. The shear stress transport (SST) turbulence model is employed to help solve the steady RANS equations, which could well predict the flow separations [63]. The high-resolution scheme is used to determine the advection terms in the discrete volume equations, the upwind advection scheme is chosen for the turbulence model equations, and the shape functions are employed to evaluate spatial derivatives for all the diffusion terms. The convergence criteria are set as root mean square residual of 10^{-4} for each conservation law; with satisfying these criteria, the stable flow results are expected to be obtained.

4.2.3.1 CFD numerical models

Two types of CFD models are used for the numerical simulations: CFD model including both

of front and rear rotors and CFD model only including front rotor. In the past study [56], the remarkable flow interaction has been observed between front and rear rotors of a contra-rotating axial flow pump in experiments. However, it is very difficult to evaluate the effect caused by the blade-rows interaction. Therefore, we have considered the front rotor performance without the interaction between front and rear rotors, which can be obtained using the CFD model for only front rotor. Meanwhile, the rear rotor performance has been evaluated considering all such interactions, which can be achieved using the both CFD models. As will be seen in the results in Section 4.2.7, this strategy is effective and can well help the proposed model predict the total performances.

Figure 4-4 illustrates the two types of CFD models for the numerical simulations in the present study. The inlet boundary is placed at about $4D_c$ upstream of the leading edge (L.E.) of front rotor. The outlet boundary is located at about $1.3D_c$ downstream of the trailing edge (T.E.) of rear rotor or about $1.7D_c$ downstream of the T.E. of front rotor. The inlet boundary condition is set as mass flow rate with medium turbulence intensity. Since the flow direction is locally unknown at the outlet of rear rotor domain, the outlet boundary condition is defined as opening type with relative pressure with 0Pa under fully developed turbulence condition. The surfaces of rotors, shroud and hubs are set as a no-slip wall. The automatic near-wall treatment is used for the SST turbulence model. As shown in Fig. 4-4 (a), the interface between front and rear rotor domains is defined with a mixing plane (stage type), where the flow data is averaged in circumferential direction on both side of the mixing plane.

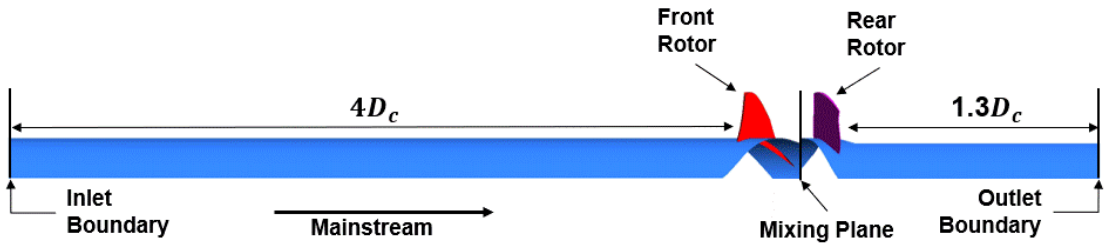

(a) CFD model for front and rear rotors

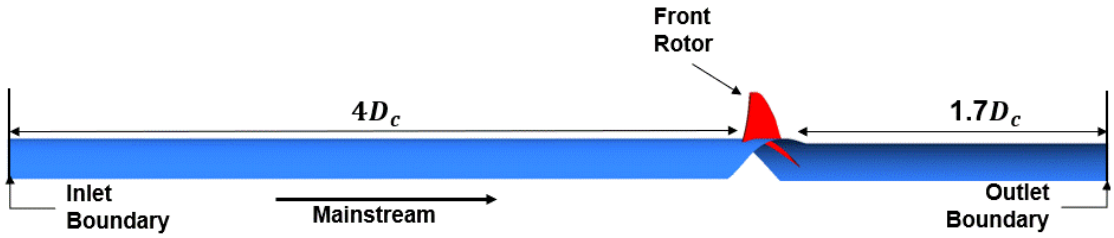

(b) CFD model for only front rotor

Fig. 4-4 CFD models for simulations

The meshes of CFD models are generated with the ANSYS TurboGrid 18.0. In this study, 8 elements are radially located in the blade tip clearance to capture the tip leakage flow of front and rear rotors in contra-rotating axial flow pump. Because the grid number and y^+ may have significant effect on the CFD numerical results, the numerical results of various grids have also been summarized in Table 4-2. The numerical performances (total head H_t and total efficiency η_t) have been evaluated for three types of rotors: the original rotors ($\mathrm{Grid_{RR3}}$), the design optimization of rear rotor ($\mathrm{Grid_{R,Opt}}$), the design optimization of front and rear rotors ($\mathrm{Grid_{FR,Opt}}$). There are four cases of grids for each rotor. It can be found that the cases with nodes over about 1 million and average *y*+ below about 12.9, from Case 2 to Case 4, show the similar numerical performance results (only about 1% discrepancy). Therefore, it is concluded that the mesh setting of Case 2 will give numerical results with sufficient accuracy for the present purpose.

Table 4-2 Grid independency check in CFD simulations

Case	Nodes	Minimum y^+ on blades [-]	Average y^+ on blades [-]	Total Head H_t [m]	Total Efficiency η_t [-]
$\mathrm{Grid1_{RR3}}$	344,734	0.69	12.79	3.949	0.826
$\mathrm{Grid2_{RR3}}$	1,036,672	0.56	12.93	3.969	0.838
$\mathrm{Grid3_{RR3}}$	1,227,700	0.20	6.65	3.975	0.841
$\mathrm{Grid4_{RR3}}$	2,792,830	0.57	12.96	3.998	0.848
$\mathrm{Grid1_{R,Opt}}$	551,736	0.49	12.46	4.025	0.840
$\mathrm{Grid2_{R,Opt}}$	1,041,834	0.49	12.54	4.053	0.849
$\mathrm{Grid3_{R,Opt}}$	1,233,820	0.29	6.46	4.088	0.852
$\mathrm{Grid4_{R,Opt}}$	1,949,548	0.48	12.60	4.094	0.856
$\mathrm{Grid1_{FR,Opt}}$	553,572	0.53	10.96	4.262	0.831
$\mathrm{Grid2_{FR,Opt}}$	1,044,786	0.41	11.06	4.280	0.839
$\mathrm{Grid3_{FR,Opt}}$	1,233,884	0.27	5.67	4.283	0.834
$\mathrm{Grid4_{FR,Opt}}$	1,953,616	0.50	11.10	4.298	0.840

4.2.3.2 Accuracy of CFD simulations

In the past study [38], experiments for the original RR3 rotors in contra-rotating axial flow pump have been conducted. The detailed information of the experimental test rig can be found in the study of Furukawa et al. [36]. It should be noted that the experimental performance is determined using the torque of rotors as well as the time-averaged casing static pressure at upstream of front rotor and downstream of rear rotor.

Figure 4-5 shows the performances for the original RR3 rotors in experiments and CFD simulations. As can be seen, remarkable discrepancies exist in the head evaluations at very low flow rates, which may be the result of the steady calculation's limits in predicting unsteady phenomenon at very low flow rates. Small discrepancies near the design flow rate seem to be the result of over evaluated losses due to the mixing plane applied between the front and rear rotor domains. The unsteady RANS simulation of full rotors which can properly take account of rotor-rotor interaction may improve the accuracy of performance prediction, realizing much better

agreement with experiment [51]. However, since the discrepancy between the steady CFD and experiment is still small enough and their tendencies in performance change agree well at near-design flow rates, CFD results at the near-design flow rates ($0.8Q_d, 0.9Q_d, 1.0Q_d, 1.1Q_d$) with design rotational speed are useful and will be chosen as the base data for the construction of metamodel.

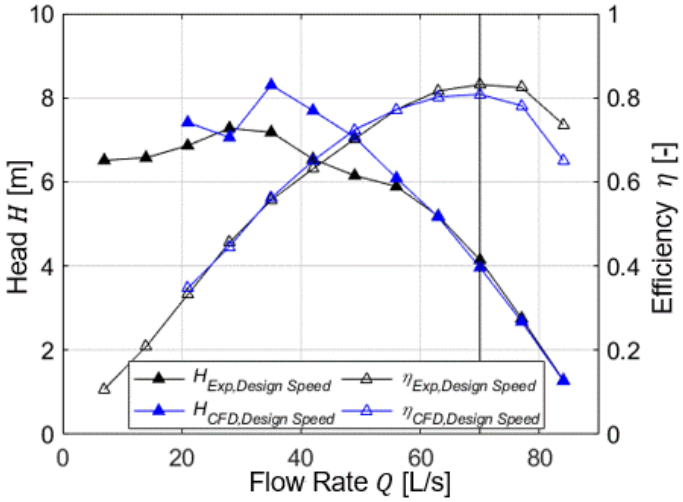

Fig. 4-5 Performances evaluated by experiments and CFD simulations for the original rotors RR3 under design rotational speed

4.2.4 Metamodel

In the design optimization of turbomachines, an optimization algorithm usually chooses one optimal solution from a large population of designs. Such algorithm could take unacceptable time if we conduct CFD simulations for every design in the population. Instead, the metamodel is well used to do the fast prediction. In the present study, the metamodel is employed and will be trained only on the basis of CFD simulations with shape parameters under the design rotational speed at near-design flow rates ($0.8Q_d, 0.9Q_d, 1.0Q_d, 1.1Q_d$), which shows more convincible numerical results and lower computational cost.

4.2.4.1 Design parameters

There are many design parameters for the rotors in contra-rotating axial flow pump, such as blade lengths, blade thicknesses, blade profiles, stagger angles, stacking positions and so on. Since the rotor has a three-dimensional (3D) shape, all the above factors need to be considered in many sections from hub to tip. In this study, we will only consider the design parameters in five radially distributed sections from hub to tip, which seems to be sufficient to represent a 3D blade shape.

Table 4-3 summarizes the blade profile of the RR3 rotors. As we can see, there are many design parameters for the blade. Actually, we are most interested in the blade twist, sweep, lean and length, which have significant influence on the performance of turbomachines [64][65]. Therefore, the functional forms for camber line and thickness distribution will be kept the same throughout the present study.

Table 4-3 Blade profile of the original rotors RR3

	Section	1(Hub)	2	3	4	5(Tip)
Front Rotor	Radius [m]	0.05	0.0625	0.0745	0.087	0.099
	Solidity σ [-]	1.29	1.056	0.897	0.782	0.7
	Stagger γ [°]	51.69	62.1	68.49	72.75	75.81
	Inlet Blade Angle β_{B1} [°]	63	73.41	79.8	84.06	87.12
	Outlet Blade Angle β_{B2} [°]	44.1	54.51	60.9	65.16	68.22
	Max Camber Location x_f/l [-]	0.4	0.4	0.4	0.4	0.4
	Max Thickness t/l [-]	0.1	0.09	0.08	0.07	0.06
Rear Rotor	Radius [m]	0.05	0.0625	0.075	0.0875	0.099
	Solidity σ [-]	1.008	0.936	0.864	0.792	0.72
	Stagger γ [°]	64.82	67.01	69.73	72.34	72.2
	Inlet Blade Angle β_{B1} [°]	69.63	70.88	72.31	73.67	80.17
	Outlet Blade Angle β_{B2} [°]	52.15	61.14	67.16	71.47	69.2
	Max Camber Location x_f/l [-]	0.6	0.55	0.5	0.45	0.4
	Max Thickness t/l [-]	0.08	0.07	0.06	0.05	0.04

The camber lines in front and rear rotors are both determined with:

$$\theta\left(\frac{x}{l}\right) = a\left(\frac{x}{l}\right)^2 + b\frac{x}{l} + c \tag{4-1}$$

where θ is the local gradient angle of the camber line, x means location from 0 to chord length l, and a, b and c represent constants. In the present study, the camber line formulation of the 5 sections from hub to tip stays same with that in the original rotors RR3. The constants a, b and c in camber line formulation of the 5 sections for front and rear rotors have been determined using the data of RR3 design (shown in Table 4-3) with the following equations.

$$\theta(0) = \beta_{B1} - \gamma$$

$$\theta(1) = \gamma - \beta_{B2}$$

$$\theta\left(x_f/l\right) = 0$$

For the design optimizations made in the present study, the obtained constants a, b and c are used for the both front and rear rotors. It should be noted that the front rotor camber line determined with Eq. (4-1) is a little different from that in RR3 front rotor whose blade profiles are NACA 44* series.

On the other hand, for the blade thickness distribution, that of NACA 4* series is employed to design the blade profile, and the expression is written as:

$$\frac{y_t(x)}{l} = 5\frac{t}{l}\left(a_0\left(\frac{x}{l}\right)^{0.5} + a_1\left(\frac{x}{l}\right)^1 + a_2\left(\frac{x}{l}\right)^2 + a_3\left(\frac{x}{l}\right)^3 + a_4\left(\frac{x}{l}\right)^4\right) \tag{4-2}$$

where $y_t(x)$ denotes thickness at position x, coefficients $a_0 \sim a_4$ are 0.2969, -0.126, -0.3516, 0.2843 and -0.1015 respectively. The maximum thickness ratio t/l is distributed as shown in Table 4-3, which are kept the same throughout the design optimization.

The sweep and lean of blade can be obtained by defining the tip stacking position in axial ($z_{tip,stack}$) and circumferential ($\theta_{tip,stack}$) directions, while the stacking position at hub is fixed and a linear change in the stacking position between the hub and tip is assumed. The twist of blade

can be realized by describing the inlet blade angle β_{B1} at the five sections from tip to hub. The blade length can be changed using the solidity at sections of hub σ_{hub} and tip σ_{tip}. Their changes are also assumed to be similar to those of the original rotors RR3. As a result, combining with Eqs. (4-1) and (4-2), there will be only 9 design parameters for each rotor to achieve the blade design with twist, sweep, lean and length changes.

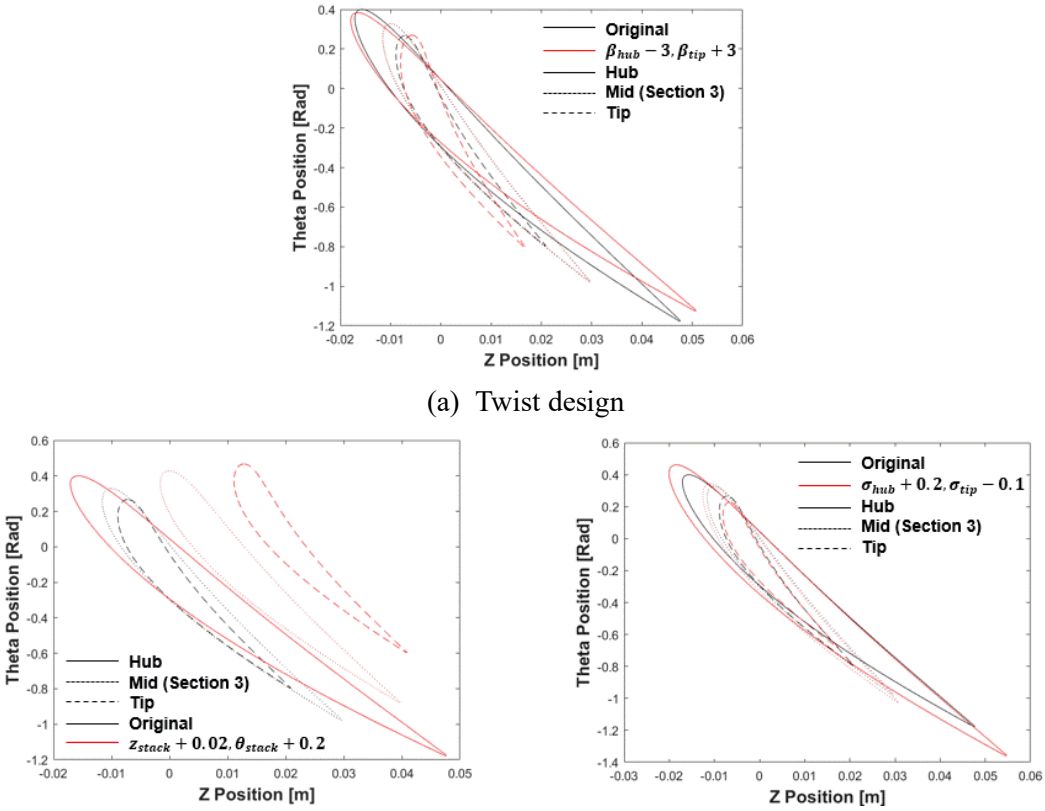

(a) Twist design

(b) Design of sweep and lean

(c) Length design

Fig. 4-6 Front rotor blade design considering twist, sweep, lean and length

Figure 4-6 shows the example designs considering twist, sweep, lean and length changes for the front rotor. In Fig. 4-6 (a), only the inlet blade angle β_{B1} at hub and tip are changed. It can be easily found that blade rotates related to the original blade only at hub and tip. In Fig. 4-6 (b) and (c), the tip stacking positions and solidities are also changed respectively. The profiles of the

shape are well reflected by our design parameters. According to the effect of the above design parameters (especially in the rear rotor) checked using analysis of variance (ANOVA) in the Sec. 4.3.2, all the design parameters show large influence on the general input power, which indicates the selection of these design parameters is appropriate.

4.2.4.2 Design of experiments (DOE)

The metamodel needs to be trained based on the CFD simulations, which are usually conducted according to the design of experiments (DOE). Usually, a good experimental design for CFD numerical simulations tends to fully distribute the parameters in the design space [66]. The Latin Hypercube Designs (LHD) is one of the most common space-filling design methods for computer experiments, which can deal with many design parameters with small sampling size. In many design optimizations of turbomachines, the LHD has been well employed to generate samples to construct metamodel [67][68]. Therefore, in the present study, the LHD method has also been employed to design the CFD experiments through a commercial code: MATLAB R2018a.

Table 4-4 illustrates the design variables for the original rotors RR3 and for the lower and upper bounds of design space. The initial data base to train the metamodel includes 45 samples designed with LHD method. In order to examine the predictions of the metamodel, 9 samples are selected using LHD method and CFD simulations are conducted for them. The new additional 9 samples will be added in the data base and the examination will be repeated if good enough agreement cannot be observed between the predictions of metamodel and CFD simulations. After the above procedures, for each rotor, total of 54 samples have been designed with LHD in the design space. The detailed information of DOE for front and rear rotors has been attached in the Appendix.

Table 4-4 Geometrical design parameters and their bounds for DOE

		Original	Lower Bound	Upper Bound
Front Rotor	Hub Inlet Blade Angle $\beta_{B1,hub}$ [°]	63	59	67
	Section 2 Inlet Blade Angle $\beta_{B1,S2}$ [°]	73.41	69.41	77.41
	Section 3 Inlet Blade Angle $\beta_{B1,S3}$ [°]	79.8	75.8	83.8
	Section 4 Inlet Blade Angle $\beta_{B1,S4}$ [°]	84.06	80.06	88.06
	Tip Inlet Blade Angle $\beta_{B1,tip}$ [°]	87.12	83.12	91.12
	Tip Axial Stacking Position $z_{tip,stack}$ [m]	0	-0.01	0.005
	Tip Circumferential Stacking Position $\theta_{tip,stack}$ [Rad]	0	-0.3	0.3
	Hub Solidity σ_{hub} [-]	1.29	0.99	1.34
	Tip Solidity σ_{tip} [-]	0.7	0.5	0.9
Rear Rotor	Hub Inlet Blade Angle $\beta_{B1,hub}$ [°]	69.63	65.63	73.63
	Section 2 Inlet Blade Angle $\beta_{B1,S2}$ [°]	70.88	66.88	74.88
	Section 3 Inlet Blade Angle $\beta_{B1,S3}$ [°]	72.31	68.31	76.31
	Section 4 Inlet Blade Angle $\beta_{B1,S4}$ [°]	73.67	69.67	77.67
	Tip Inlet Blade Angle $\beta_{B1,tip}$ [°]	80.17	76.17	84.17
	Tip Axial Stacking Position $z_{tip,stack}$ [m]	0	-0.005	0.01
	Tip Circumferential Stacking Position $\theta_{tip,stack}$ [Rad]	0	-0.5	0.5
	Hub Solidity σ_{hub} [-]	1.008	0.7	1.2
	Tip Solidity σ_{tip} [-]	0.72	0.5	1

4.2.4.3 Structure of artificial neural network (ANN)

As for the metamodel, the artificial neural network (ANN) has been widely used in the design optimization of turbomachinery [69][70]. In this study, the ANN has also been chosen for the metamodel for the prediction of the theoretical head and head loss of front and rear rotors at the design rotational speed. The MATLAB R2018a Neural Network Toolbox is employed for the ANN, and the ANN is trained using sample data with Levenberg-Marquardt backpropagation algorithm [71].

The ANN generally consists of an input layer, several hidden layers and an output layer. The

nodes in each layer are fully connected with each other. The input design parameters are connected to the neurons in the input layer, while the output objectives are assigned to the nodes in the output layer. Therefore, the numbers of neurons in the input and output layers are the number of design variables and that of objective function, which are 9 and 1 respectively in the present study. Even though one hidden layer and two hidden layers can cope with the non-linear problems in most cases [72], only the number of neurons in each hidden layer needs to be carefully selected.

In order to choose an appropriate number of neurons in the hidden layer, ANN is trained for 10 times with the same neurons, then the number of neurons is changed in a broad range. The root mean square (RMS) of theoretical head errors will be used to evaluate the performance of ANN with various number of neurons in each hidden layer, and it is written as:

$$\mathrm{RMS} = \sqrt{\frac{1}{N}\sum_{1}^{N}(H_{th,ANN,i} - H_{th,CFD})^2} \tag{4-3}$$

where RMS means the root mean square value for theoretical head errors, subscripts 'ANN' and 'CFD' denotes value evaluated by ANN and CFD respectively, and *i* represents the *i*th value in the total number of *N*, here *N*=10.

Figure 4-7 (a) illustrates the error of ANN prediction for theoretical head (Euler head) in the case with one hidden layer, where the RMS value is plotted against the number of neurons from 1 to 20. As we can see, the number of neurons below 11 shows large RMS value, while that over 12 shows relatively small RMS value (about 0.05m). Figure 4-7 (b) indicates similarly small RMS value (about 0.05m) at first hidden layer of 5 neurons and second hidden layer of over 30 neurons in the case of two hidden layers employed. Since the ANN prediction with two hidden layers shows similar performance to that with one hidden layer, the ANN with one hidden layer with 16 neurons will be chosen for the present metamodel.

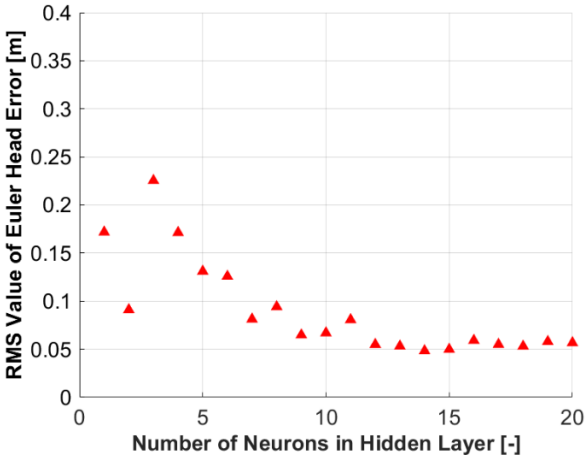

(a) Number of neurons in one hidden layer

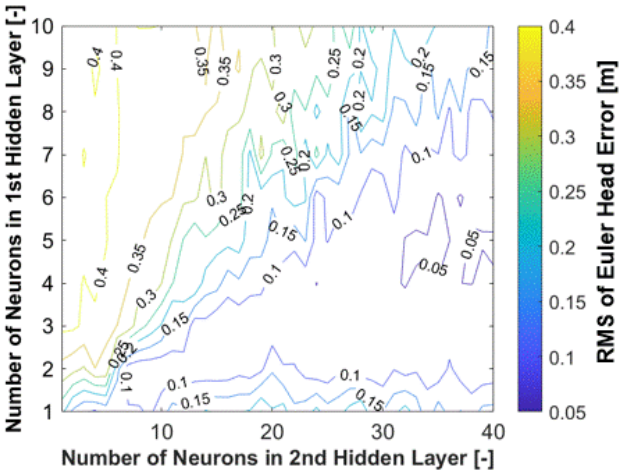

(b) Number of neurons in two hidden layers

Fig. 4-7 ANN training with one layer and two layers

4.2.4.4 Training and validations

CFD simulations with all 54 combinations of design parameters of blades selected by the LHD method have been conducted at near-design flow rates with the design rotational speed. As mentioned in Sec. 4.2.1, the metamodel will be used to determine the theoretical head modification and losses excluding the cascade loss. The metamodels will be trained for theoretical head and head loss for each front and rear rotor operated at the design rotational speed. It should be noted that theoretical head and head loss of CFD simulations are determined with flow velocities and total pressure on the near-rotor cross sections f1, f2 and r2 (shown in Fig. 4-11).

The 9 samples have been determined with the LHD method in the design space for front and rear rotors separately, and CFD simulations are operated for them to validate the prediction of the ANN. Figure 4-8 illustrates the validations of ANN for the rear rotor head loss and the theoretical head. As we can see, the ANN predictions agree well with the CFD value. There are two samples at flow rate of 56L/s ($0.8Q_d$) whose CFD validations is located at 0. This means that the CFD simulations cannot achieve convergence at these two samples.

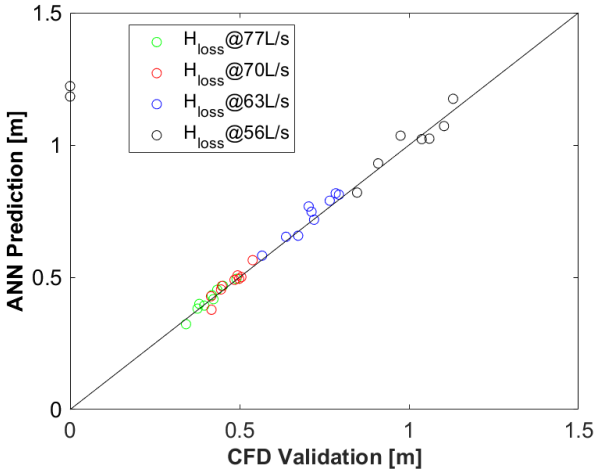

(a) Head loss

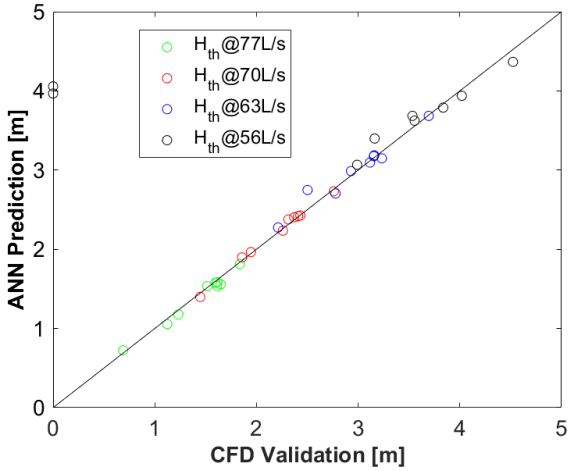

(b) Theoretical head

Fig. 4-8 Validations of ANN for rear rotor

Figure 4-9 also shows the validations of ANN for the front rotor. Good agreement can be observed in the theoretical head of ANN and CFD, while head loss predicted by ANN roughly agree with that evaluated by CFD. Since the amount of head loss in front rotor is small, such rough agreement in the head loss of front rotor could be still enough for the total performance calculation.

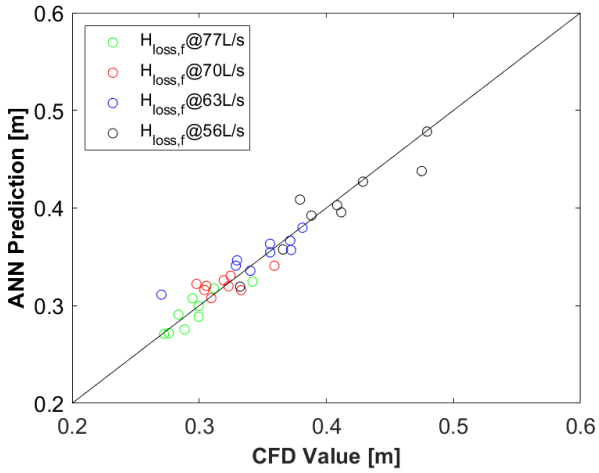

(a) Head loss

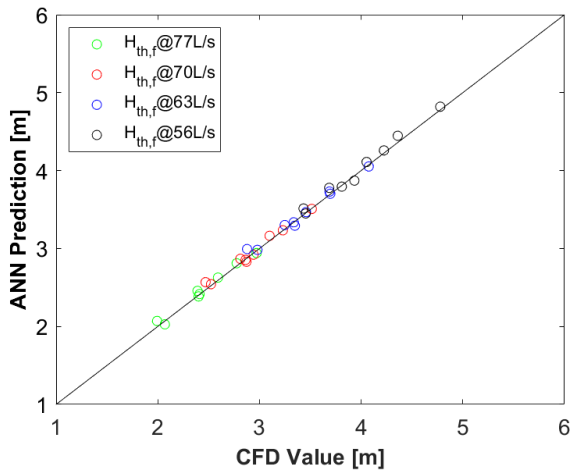

(b) Theoretical head

Fig. 4-9 Validations of ANN for front rotor

4.2.5 Theoretical head prediction

4.2.5.1 Basic equations

The basic equations employed in the present chapter are the basically same with those used in the previously proposed performance prediction model toward RSC in contra-rotating axial flow pump [62]. The metamodel provides the base data to construct the empirical formulae for the modification of theoretical head and the prediction of head loss. In order to simplify the flow in the performance prediction model, the following assumptions have been employed: steady flow, axisymmetric flow, no reverse flow, negligible viscous losses along the streamtube and uniform flow with no swirl at the front rotor inlet. Figure 4-10 shows a meridional sketch of contra-rotating axial flow pump.

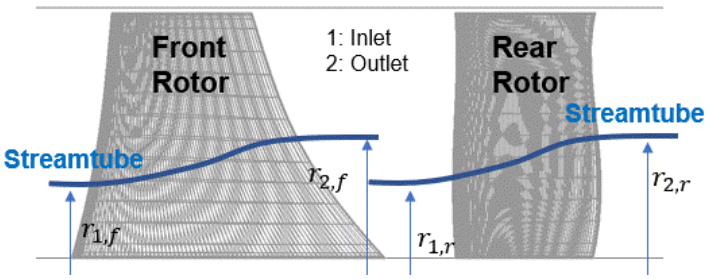

Fig. 4-10 Streamtubes assumed in contra-rotating axial flow rotors

Blue lines indicate the typical streamtubes. There are four basic equations in the performance prediction model to calculate the flow velocities: radial equilibrium equations [6] at the inlet and outlet of rotors, rothalpy conservation equation [23] along the streamtube, mass conservation equation in the streamtube and the empirical deviation angle equation [41]. The above 4 equations under the aforementioned assumptions can be written as follows:

$$\frac{dp}{dr} = \rho \frac{v_\theta^2}{r} \tag{4-4}$$

$$\frac{p_1}{\rho} + \frac{1}{2}w_1^2 - \frac{1}{2}(r_1\omega)^2 = \frac{p_2}{\rho} + \frac{1}{2}w_2^2 - \frac{1}{2}(r_2\omega)^2 \tag{4-5}$$

$$v_{a1} r_1 dr_1 = v_{a2} r_2 dr_2 \tag{4-6}$$

$$\delta = \delta_{ref} + k(i - i_{ref}) \tag{4-7}$$

Equation (4-4) shows the radial equilibrium equations, where *p* represents local static pressure, *r* is the local radius, ρ means flow density, and v_θ denotes the swirling velocity. Equation (4-5) demonstrates the rothalpy conservation equation along a streamtube, where *w* is the relative velocity, ω means the angular rotational speed of rotor, and subscripts 1 and 2 represent the inlet and outlet of rotors respectively. Equation (4-6) illustrates the mass conservation equation along a streamtube, where v_a means the axial velocity. Equation (4-7) shows the empirical deviation angle equation, where δ is the deviation angle, i represents the incidence angle, subscript "ref" means the reference angles determined with CFD simulation of the original rotors RR3 at the design flow rate with design rotational speed, and k denotes the empirical coefficient related to inlet flow angle β_1 and solidity σ. It should be noted that the front rotor reference angles for optimization of both of front and rear rotors are determined with CFD of front rotor designed with camber line formulation of Eq. (4-1) using the design parameters of RR3. More details of the empirical coefficient *k* can be found in Lieblein's research [41]. After the determination of deviation angle δ, the exit flow angle β_2 can be calculated with the blade exit angle $\beta_{b,2}$ using the following expression: $\beta_2 = \beta_{b,2} + \delta$.

By considering velocity triangles of front and rear rotors and the above 4 equations, the differential equation on axial velocity at rotor exit dv_{a2}/dr_2 is obtained as:

$$\begin{aligned}\frac{dv_{a2}}{dr_2} = \cos^2\beta_2 \Bigg\{ & 2\omega\tan\beta_2 - \frac{\tan\beta_2}{\cos^2\beta_2}\frac{d\beta_2}{dr_2} v_{a2} + \frac{1}{r_1}\frac{dv_{a1}}{dr_1} r_2 - \tan^2\beta_2 \frac{v_{a2}}{r_2} \\ & + \frac{r_2}{v_{a1} r_1}\left[\frac{dp_1}{\rho dr_1} + (v_{\theta 2} + \omega r_1)\frac{dv_{\theta 1}}{dr_1} + \omega v_{\theta 1}\right]\Bigg\}\end{aligned} \tag{4-8}$$

Equation (4-8) is a simple ordinary differential equation so that it can be numerically solved with sufficient accuracy. In the present study, the exit axial velocity v_{a2} is calculated in the 2nd

order precision using Taylor's series. Then the other velocities (swirling velocity v_θ, relative velocity w …) can be obtained with the velocity triangles of front and rear rotors. Finally, the theoretical head of each rotor can be determined with:

$$H_{th} = \frac{T\omega}{\rho g Q} = \frac{\omega}{gQ}\int (r_2 v_{\theta 2} - r_1 v_{\theta 1})\, dQ = \frac{\omega}{gQ}\int_{r_{hub}}^{r_{tip}} (r_2 v_{\theta 2} - r_1 v_{\theta 1}) 2\pi r_1 v_{a1} dr \qquad (4\text{-}9)$$

where T indicates the torque of rotors, g is the gravity, r_{tip} and r_{hub} represent radii at tip and hub of the blade respectively. The theoretical head of CFD simulations will also use Eq. (4-9) at the rotor-adjacent cross sections f1, f2 and r2 (shown in Fig. 4-11).

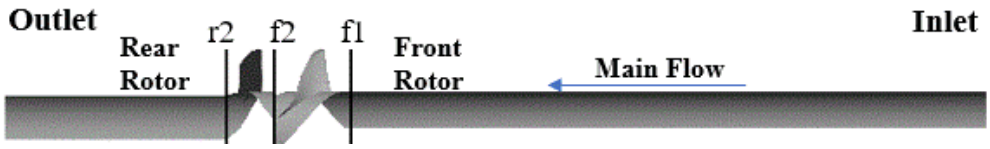

Fig. 4-11 Positions of performance evaluation

4.2.5.2 Empirical modification

The flow generated by the rear rotor may have significant influence on the flow around front rotor. Such influence could be more remarkable at low flow rates with design rotational speed [56], which may result in in-negligible error in the theoretical head prediction. In the previous study, Zhang et al. [62] have well correlated the lift coefficient of rear rotor blade at tip with the discrepancy of theoretical head prediction.

The lift coefficient C_L can be simply evaluated from the momentum and energy conservation laws of the flows in the cascade, considering the axial velocity change from the inlet to the outlet [59]:

$$C_L = \frac{2}{\sigma}\left\{\left(1 - \frac{\xi}{2}\right)\tan\beta_1 - \left(1 + \frac{\xi}{2}\right)\tan\beta_2\right\}\cos\beta_m - C_D \tan\beta_m \qquad (4\text{-}10)$$

where ξ denotes the axial velocity change ratio defined with the inlet and outlet axial velocities as $\xi = 2\,(v_{a2} - v_{a1})/(v_{a2} + v_{a1})$, β_m is the average flow angle determined from $2\tan\beta_m =$

$(1-\xi/2)\tan\beta_1 + (1+\xi/2)\tan\beta_2$, and C_D is the drag coefficient. The drag coefficient is expressed as follows, using the cascade loss coefficient ζ_c (introduced by Eq. (4-13) in Section 4.2.6.1).

$$C_D = \frac{1}{\sigma}(1-\frac{\xi}{2})^2\zeta_c\frac{\cos^3\beta_m}{\cos^2\beta_1}$$

In the previous study [62], it has been found that the discrepancy of predicted theoretical head is well correlated with the tip lift coefficient $C_{L,tip}$ and the normalized discrepancy *y* expressed by a function of $C_{L,tip}$ constructed using the design-speed data well holds even under conditions with off-design rotational speed. Here, this strategy is again employed by using the design-speed performance data obtained by the metamodel. The normalized discrepancy *y* is now defined by:

$$y = g\frac{H_{th,model} - H_{th}}{(\omega r_{tip})^2} = F_1(C_{L,tip}) \quad (4\text{-}11)$$

where $H_{th,model}$ is the theoretical head based on flow velocities calculated using basic equations in the performance prediction model, ω represents angular rotating speed of rotors, and r_{tip} denotes the blade tip radius. The function F_1 is discretely determined at the several flow rates near the design flow rate under the design rotational speed by using $H_{th,ANN}$ (theoretical head obtained by the metamodel) as H_{th} in Eq. (4-11), and the linear interpolation is introduced among the discrete points. As an example, Fig. 4-12 (a) shows the *y* vs $C_{L,tip}$ for the No. 3 shape in the DOE of rear rotor. Black symbols connected by lines show the F_1 curve for the No. 3 shape under the design rotational speed. Colored symbols show the normalized discrepancy of the theoretical head prediction under off-design rotational speeds. In order to compare with the previous study (black dashed line), the horizontal axis represents tip lift coefficient $C_{L,tip} - C_{L,tip,ref}$, where $C_{L,tip,ref}$ is the tip lift coefficient at the design flow rate with design rotational speed. Since the F_1 curve seems well coincide with the normalized discrepancy under the off-design rotational speed, it is possible to use the F_1 curve for the modification of theoretical head

prediction under the condition with off-design rotational speed.

In the front rotor, because of the complex 3D flow caused by twist, sweep and lean of blade [64], it could be insufficient to predict the theoretical head only using the basic equations in the performance model. Therefore, empirical modifications on the theoretical head become necessary. Figure 4-12 (b) also shows the y vs $C_{L,tip}$ in the No. 11 shape of DOE for front rotor. The black line represents ANN results (basically same with CFD results) under conditions with design rotational speed. The CFD results under conditions with off-design rotational speed distribute near the black line. Therefore, it seems to be still possible to modify the theoretical head of front rotor using similar method with rear rotor.

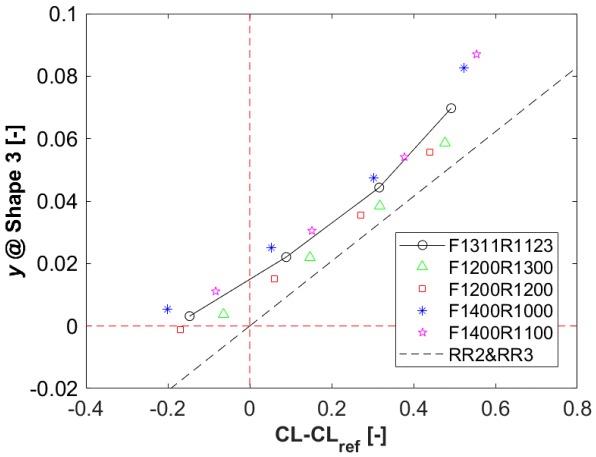

(a) Modification in rear rotor

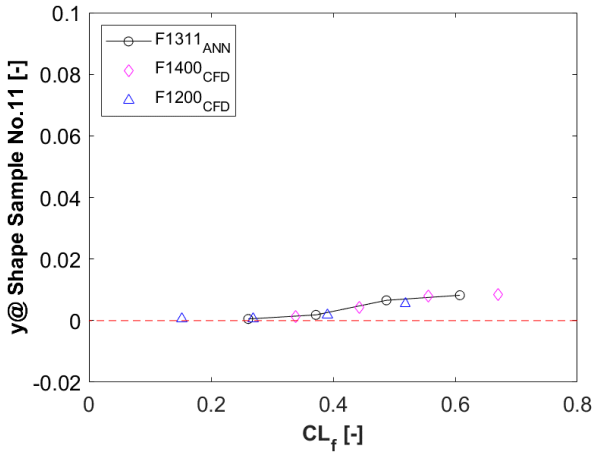

(b) Modification in front rotor

Fig. 4-12 Empirical modification of theoretical head

Finally, by using the function F_1, the theoretical head under the off-design rotational speed can be modified by the following equation.

$$H_{th} = H_{th,model} - F_1(C_{L,tip})\frac{(r_{tip}\omega)^2}{g} \tag{4-12}$$

4.2.6 Loss head evaluation

The flow losses are classified into the following three parts in the performance prediction model: cascade loss, other losses and mixing loss. The cascade loss has been directly determined with an empirical cascade loss model [42]. The other losses are modelled according to the blade tip lift coefficient. The mixing loss is calculated using flow velocities at the outlet of rear rotor.

4.2.6.1 Empirical cascade loss

According to Lieblein's paper [42], the empirical cascade loss coefficient ζ_c is given by:

$$\zeta_c = 2(\frac{\delta_{m2}}{l})\sigma\frac{\cos^2\beta_1}{\cos^3\beta_2}\left\{\frac{2.16}{2.24}/[1-(\frac{\delta_{m2}}{l})\frac{1.08\sigma}{\cos\beta_2}]^3\right\} \tag{4-13}$$

where the loss coefficient ζ_c is defined with total pressure loss $p_{t,loss}$ and inlet relative velocity w_1 as $\zeta_c = 2p_{t,loss}/(\rho w_1^2)$. (δ_{m2}/l) denotes the momentum thickness coefficient which is calculated by

$$\left(\frac{\delta_{m2}}{l}\right) = \begin{cases} 0.004/\left(1-1.17lnD_{eq}\right) & D_{eq} \le 2 \\ 0.004/(1-1.17ln2) + 0.11\left(D_{eq}-2\right) & D_{eq} > 2 \end{cases}$$

where D_{eq} is the equivalent diffusion factor. It should be noted that the equation with $D_{eq} > 2$ has been added to well achieve loss calculation convergence.

The cascade loss can be locally calculated at every radial location, and then the mass-averaged cascade loss head $H_{loss,cascade}$ is determined by:

$$H_{loss,cascade} = \frac{1}{2gQ}\int w_1^2\zeta_c dQ = \frac{1}{2gQ}\int_{r_{hub}}^{r_{tip}} w_1^2\zeta_c 2\pi r_1 v_{a1} dr \tag{4-14}$$

4.2.6.2 Empirical other losses

The cascade loss model shows large discrepancy with losses calculated by CFD at the tip region, which may be the results of tip clearance effect. In order to quantify the losses excluding cascade loss, Zhang et al. [62] have modelled such losses using blade tip lift coefficient.

The other loss coefficient $\psi_{loss,other}$ is defined as

$$\psi_{loss,other} = \frac{2g}{w_{m,tip}^2}\left(H_{loss} - H_{loss,cascade}\right) = F_2(C_{L,tip}) \tag{4-15}$$

where the tip average relative velocity $w_{m,tip}$ is determined with the relative velocities at inlet $w_{1,tip}$ and outlet $w_{2,tip}$ of the blade tip by $w_{m,tip} = (w_{1,tip} + w_{2,tip})/2$. The function of F_2 is discretely determined at the several flow rates near the design flow rate under the design rotational speed by using $H_{loss,ANN}$ (head loss obtained by the metamodel) as H_{loss} in Eq. (4-15), and the linear interpolation is introduced among the discrete points.

As an example, Fig. 4-13 (a) illustrates the other losses for the No. 3 shape in DOE of rear rotor. Black symbols connected by lines show the F_2 curve for the No. 3 shape under the design rotational speed. Colored symbols show the other loss coefficient under the off-design rotational speed. For the reference, the dashed blue line represents the following equation for the original rotors RR3.

$$F_{2,original}(C_{L,tip}) = \begin{cases} 0.0176C_{L,tip} + 0.0152 & C_{L,tip} \leq 0.45 \\ 0.16C_{L,tip} - 0.0489 & C_{L,tip} > 0.45 \end{cases} \tag{4-16}$$

Since the F_2 curve seems to well coincide with the other loss coefficient under the off-design rotational speed, it is possible to use the F_2 curve for the prediction of other losses under the condition with off-design rotational speed.

Figure 4-13 (b) shows the other losses for the No. 11 shape in DOE of front rotor. We can also observe that $\psi_{loss,other}$ at conditions with off-design rotational speed distributes nearly along the black line consisted with $\psi_{loss,other}$ under design rotational speed.

Finally, the other loss head $H_{loss,other}$ can be determined by:

$$H_{loss,other} = \begin{cases} \frac{w_{m,tip}^2}{2g} F_2\left(C_{L,tip}\right) & \text{for general case} \\ \frac{w_{m,tip}^2}{2g} F_{2,origianl}\left(C_{L,tip}\right) & \text{for original rotors} \end{cases} \quad (4\text{-}17)$$

It should be noted that, for only the rear rotor optimization where the original front rotor is used, the latter equation in Eq. (4-17) is used for the prediction of other losses in the front rotor. In the all other cases, the former one is used.

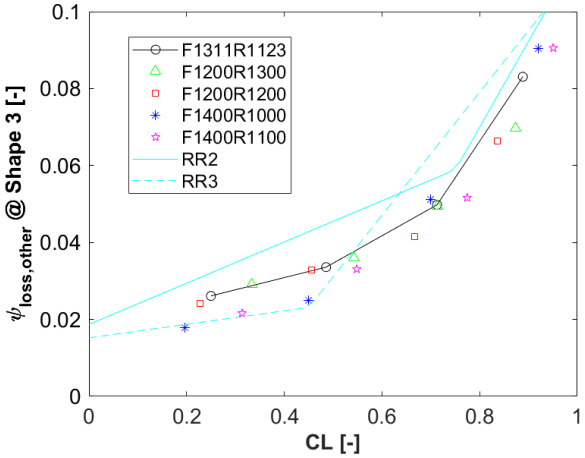

(a) Other losses in rear rotor

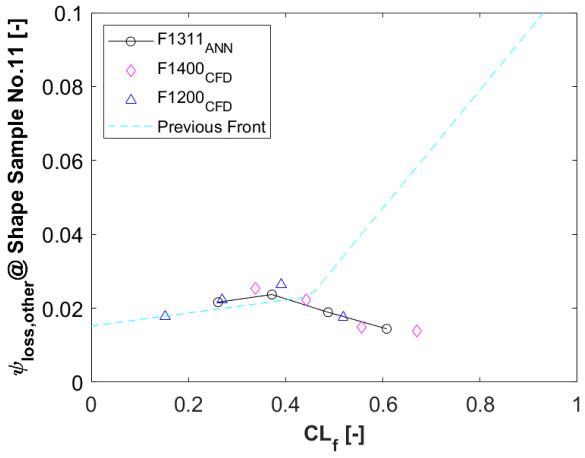

(b) Other losses in front rotor

Fig. 4-13 Empirical other losses

4.2.6.3 Mixing loss

Mixing loss occurs when non-uniform velocities exist in the flow, which might contribute significantly to the total losses in turbomachines [53][73]. In the rotational speed control (RSC) of contra-rotating axial flow pump, swirling velocity component may remain downstream of rear rotor, and the mixing loss could become in-negligible. It is demonstrated in Fig. 4-14 for the following four designs of rotors;

- $Rear_{S1}$; combination of original front rotor and No. 1 shape of DOE in rear rotor
- $Rear_{S2}$: combination of original front rotor and No. 2 shape of DOE in rear rotor
- $Front_{S0}Rear_{S0}$: combination of original front and rear rotors
- $Front_{S11}Rear_{S1}$: No. 11 shape of DOE for front rotor and No. 1 shape of DOE for rear rotor

for which CFD simulations have been conducted at various flow rates with various rotational speeds. As we can see, the mixing loss head (calculated with Eq. (4-18) which will be shown later) could contribute over 30% of the rear rotor head loss in many cases, which cannot be ignored.

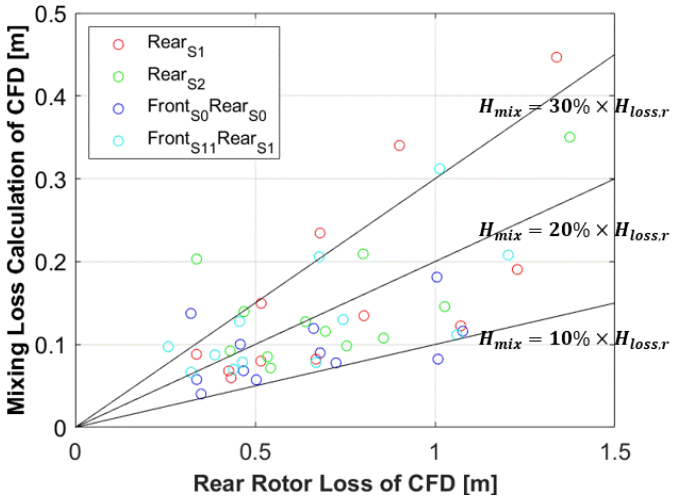

Fig. 4-14 Contribution of mixing loss

In order to evaluate the mixing loss downstream of rear rotor, steady flow is assumed in a

control volume (shown in Fig. 4-15) surrounded by the boundaries of hub, casing, rear rotor outlet and cross section far downstream. The friction is ignored at the boundary of hub and casing. At far downstream of rear rotor, the total pressure $p_{t,far}$, static pressure p_{far} and axial velocity $v_{a,far}$ will become uniform, and there will not exit swirling velocity component due to the viscous dissipation. The axial velocity far downstream $v_{a,far}$ can be determined with the flow rate Q and sectional area A by $v_{a,far} = Q/A$.

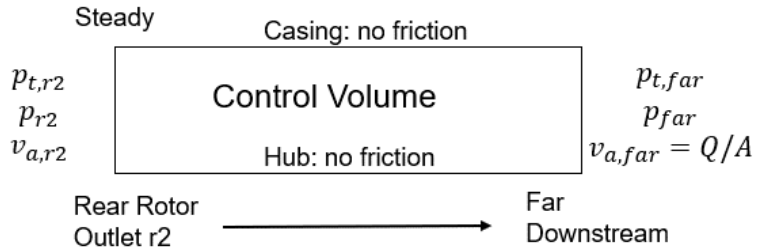

Fig. 4-15 Consideration of mixing loss calculation

By considering conservation equations of energy and momentum in the axial direction of the assumed control volume, the head of mixing loss H_{mix} can be written as:

$$H_{mix} = \frac{1}{\rho g Q}\left\{\int p_{t,r2}\, dQ - \frac{Q}{A}\int \left(p_{r2} + \frac{1}{2}\rho v_{a,r2}^2\right) dA\right\} \tag{4-18}$$

where $p_{t,r2}$, p_{r2} and $v_{a,r2}$ denote total pressure, static pressure and axial velocity at outlet of rear rotor (r2 position in Fig. 4-11), respectively.

Head of total pressure loss $H_{loss,r2,down}$ is also calculated from CFD using total pressure between the rear rotor outlet $p_{t,r2}$ and the outlet boundary $p_{t,outlet}$ of rear rotor domain to compare with the mixing loss head H_{mix}. It is calculated by:

$$H_{loss,r2,down} = \frac{1}{\rho g Q}\left(\int p_{t,r2}\, dQ - \int p_{t,outlet}\, dQ\right) \tag{4-19}$$

Figure 4-16 shows the mixing loss head H_{mix} against total pressure loss head $H_{loss,r2,down}$ in CFD simulations for various blade shapes. Good agreement can be observed between the mixing loss head and total pressure loss head in most cases, which indicates the calculation of

mixing loss using Eq. (4-18) is appropriate. Large discrepancy at two samples should be the result of significant swirling velocity remaining at the outlet boundary of the rear rotor domain.

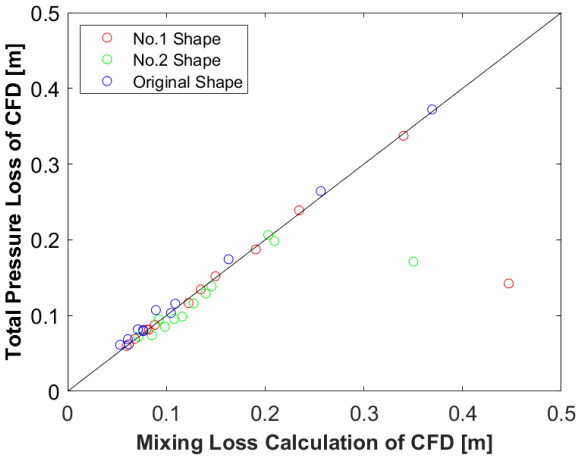

Fig. 4-16 Mixing loss check using CFD

Mixing loss head has also been calculated with the performance prediction model, which directly uses the flow velocities at the rear rotor outlet. Figure 4-17 shows mixing loss head based on CFD against mixing loss head predicted by the model for various rotor shapes under various conditions. Basically, mixing loss determined by the performance prediction model is over evaluated. The over-evaluation of mixing loss in the model may be the result of limitation of flow angle determination using the empirical deviation angle equation. The empirical deviation angle can predict well at conditions with very small swirling velocity. But it is also found that the sensitivity of the empirical deviation angle is low, this makes that the square of swirling velocity which is included in the total pressure in Eq. (4-18) is usually over evaluated. This may be the main reason causing the over-evaluation of mixing loss in the model. Even though the mixing loss based on model is over evaluated, the change tendency of model mixing loss agrees well with that of CFD mixing loss. Furthermore, the discrepancy of mixing losses could be small enough (about 2% of the total theoretical head) to calculate the total performance.

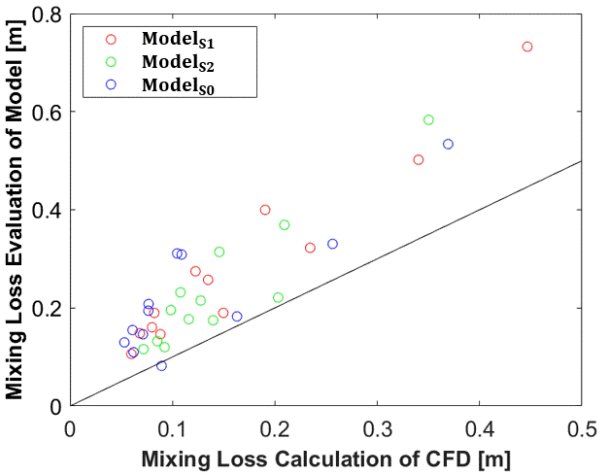

(a) Model for rear rotor optimization

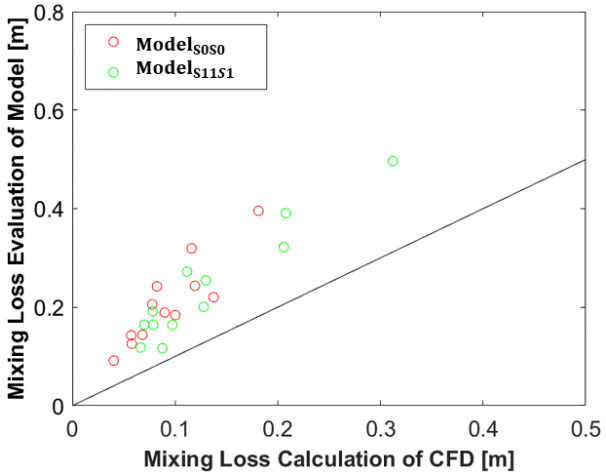

(b) Model for optimization of front and rear rotors

Fig. 4-17 Mixing loss head evaluated by models and CFD

4.2.7 Performance prediction and their validations

After the calculations of theoretical head H_{th}, loss heads including cascade loss head $H_{loss,cascade}$, other losses head $H_{loss,other}$ and mixing loss head H_{mix}, it will be possible to calculate the head H and efficiency η for each rotor:

$$H = H_{th} - H_{loss,cascade} - H_{loss,other} - H_{mix} \tag{4-20}$$

$$\eta = H/H_{th} \tag{4-21}$$

It should be noted that the mixing loss is only included in the rear rotor, and the mixing loss in front rotor is ignored since the distance between the front rotor exit and the rear rotor inlet is small.

CFD simulations have also been conducted for the various designs of front and rear rotors in contra-rotating axial flow pump at various flow rates with various rotational speeds to check the validity of performance prediction model. Figure 4-18 shows the performances of CFD and the performance prediction models. The red circles ($Rear\_{Opt}$) represent the result of performance prediction model for rear rotor optimization while blue circles (FR_{Opt}) mean that of performance prediction model for optimization of front and rear rotors. As we can see, most predictions are between 90% and 110% of CFD results. As for the prediction of total efficiency, smaller discrepancy can be observed at higher-efficiency region. This may indicate good enough accuracy of performance prediction model for determining the designs with higher performance.

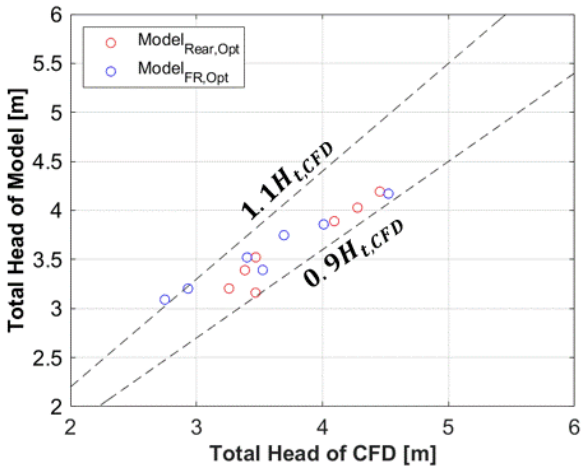

(a) Total head

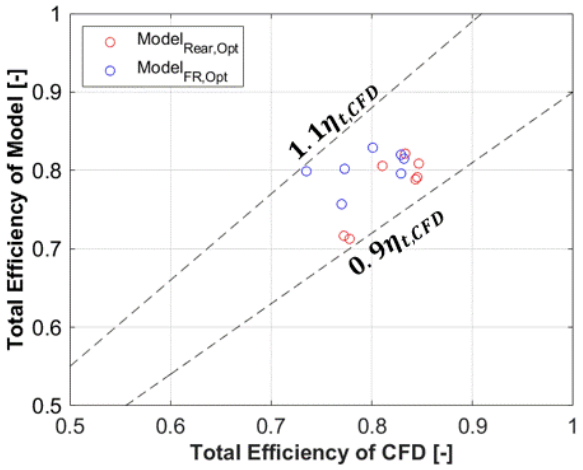

(b) Total efficiency

Fig. 4-18 Performances of CFD and performance prediction models

4.3 Genetic algorithm (GA) method

The genetic algorithm (GA) can usually capture the global optimal solution, which makes GA be the most popular optimization method in the design optimization of many turbomachines [45][47][48][70][74]. In this study, GA is also employed to find a design with the best energy saving performance using RSC in contra-rotating axial flow pump.

4.3.1 Objective functions and constraints

As illustrated in Fig. 4-19 (a), two optimization processes are required in this study: Loop 1 and Loop 2. In the main optimization of outer loop, Loop 1, overall energy saving performance at the design flow rate with design rotational speed and at off-design flow rates with rotational speed control (RSC) is considered. Furthermore, the total head $H_{Qd,Nd}$ of the design should also satisfy the design total head $H_{t,d}$. Therefore, as shown in Fig. 4-19 (b), the objective function *OF1* with a constraint in Loop 1 will be:

$$Minimize \quad OF1 = \rho g\{\sum w_Q \, QH_{th,Q,RSC} + Q_d H_{th,Qd,Nd}\}$$

$$Subject\ to \quad H_{Qd,Nd} \geq H_{t,d}$$

where Q denotes the flow rate, w_Q is the weighting function. $H_{th,Q,RSC}$ means the theoretical head at flow rate Q with rotational speed control (RSC), and $H_{th,Qd,Nd}$ represents theoretical head at the design flow rate with the design rotational speed. Minimizing *OF*1 means minimizing total input work during the long operation of the pump. Since the pump should be operated in the wide flow rate range, the weighting function should be carefully determined by referring to the expected operation scheme in the actual application of the pump. In the present study, assuming that the pump will be operated mainly at deep part loads ($0.5Q_d$~$0.7Q_d$) while sometimes operated at in $0.8Q_d$~$1.0Q_d$ and over loads ($1.1Q_d$~$1.2Q_d$) conditions, the examined flow rates of $0.5Q_d, 0.8Q_d \; and \; 1.2Q_d$ are chosen, and the weighting function is set as $w_{0.5Qd} = 0.5$ and

$w_{0.8Qd} = w_{1.2Qd} = 0.25$.

It should be noted that a kind of penalty will be added to the objective function when the total head $H_{Qd,Nd}$ is below the design requirement $H_{t,d}$. This has been demonstrated in Fig. 4-19 (b).

In the inner loop, Loop 2, the objective is to make the head $H_{Q,RSC}$ satisfy the system resistance $H_{Q,R}$ with the least theoretical head $H_{th,Q,RSC}$ by RSC at each flow rate Q (shown in Fig. 4-19 (c)), which realizes the minimum input power at each flow rate. The problem can be described as:

$$Minimize \quad OF2 = H_{th,Q,RSC}$$

$$Subject\ to \quad H_{Q,RSC} \geq H_{Q,R}$$

A penalty is also considered when the total head $H_{Q,RSC}$ is below the system resistance $H_{Q,R}$, which is illustrated in Fig. 4-19 (c).

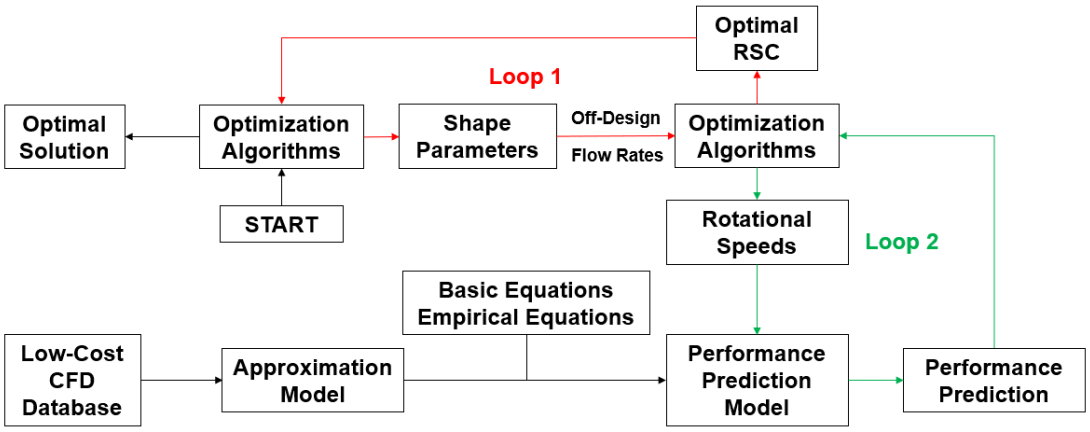

(a) Overall framework of design optimization

Fig. 4-19 Flowchart of design optimization

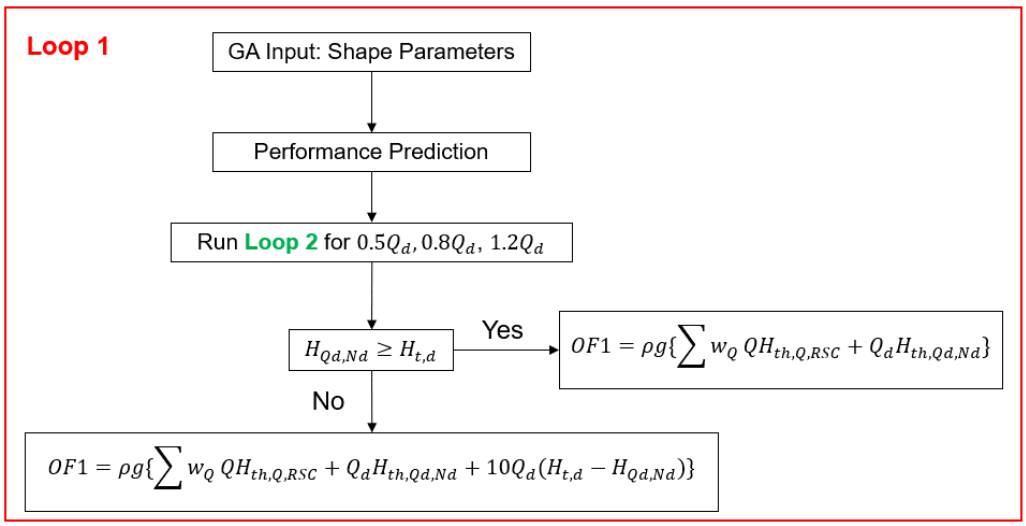

(b) Constraints and objective function in Loop 1

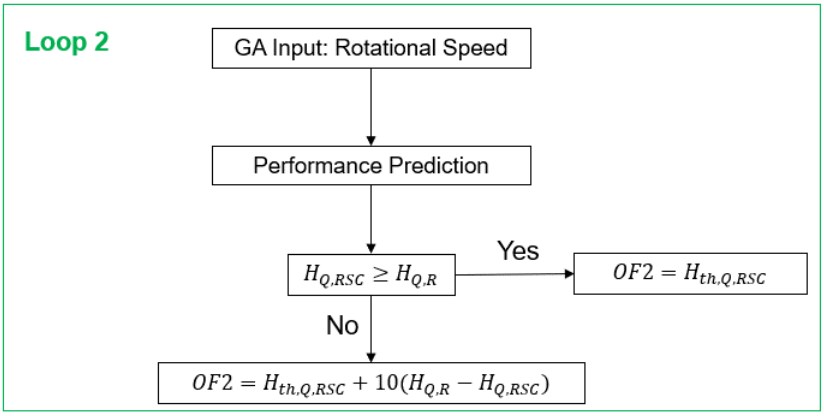

(c) Constraints and objective function in Loop 2

Fig. 4-19 Flowchart of design optimization (continued)

4.3.2 Effect of design parameters on the averaged input power

The analysis of variance (ANOVA) is well employed to recognize the effect of each design parameter on the objective functions in multi-objective problems [75][76], which could help the designers to select the optimal design from many non-dominated Pareto-front solutions. Even though only one objective is used in each loop for the design optimization in the present study, it is still necessary to check the significance of each design parameter. It is believed that the change of design parameters in front rotor usually has influence on the performances of both of front and

rear rotors, while the change of design variables in rear rotor could only affect on the rear rotor's performance. Therefore, the ANOVA will only be performed for the design parameters in rear rotor.

Since there are two optimization loops (one includes shape parameters, and another includes rotational speed) in the present study, the design parameters in rear rotor will be combined with the rotational speed of front and rear rotors. Then, by using a commercial code: MATLAB R2018a Statistics and Machine Learning Toolbox, the ANOVA is operated with 11 design variables (9 design parameters in rear rotor, and the rotational speeds of front and rear rotors) for an averaged input power $P_{input,averaged}$:

$$P_{input,averaged} = \frac{\rho g}{4}(0.8Q_d H_{th,0.8Q_d} + 0.9Q_d H_{th,0.9Q_d} + 1.0Q_d H_{th,Q_d} + 1.1Q_d H_{th,1.1Q_d})$$

Table 4-5 Analysis of variance (ANOVA)

Design variables for ANOVA	p-value
Hub Inlet Blade Angle $\beta_{B1,hub}$	0.36
Section 2 Inlet Blade Angle $\beta_{B1,S2}$	0.00
Section 3 Inlet Blade Angle $\beta_{B1,S3}$	0.00
Section 4 Inlet Blade Angle $\beta_{B1,S4}$	0.00
Tip Inlet Blade Angle $\beta_{B1,tip}$	0.00
Tip Axial Stacking Position $z_{tip,stack}$	0.00
Tip Circumferential Stacking Position $\theta_{tip,stack}$	0.00
Hub Solidity σ_{hub}	0.00
Tip Solidity σ_{tip}	0.00
Rotational Speed of Front Rotor N_f	0.00
Rotational Speed of Rear Rotor N_r	0.00

Table 4-5 summarizes the ANOVA results based on the predictions of the proposed model. The p-value [77] indicates the probability that the averaged input power $P_{input,averaged}$ keeps constant with the change of the corresponding design variable. Small p-value means the

significant effect while large p-value shows little significance. As illustrated in Table 4-5, almost all the parameters (excluding the hub inlet blade angle $\beta_{B1,hub}$) show significant effect on the averaged input power $P_{input,averaged}$. Compared with other design parameters, the hub inlet blade angle $\beta_{B1,hub}$ seems to have less (but not small enough) impact on $P_{input,averaged}$, this basically corresponds to our knowledge related to the hydrodynamics in pumps. Since significant effect can be observed in most design parameters, the design variables selected in the present study could not be removed.

4.3.3 Description of GA

In the present study, MATLAB R2020a Global Optimization Toolbox has been employed to run the genetic algorithm (GA) with penalty [78] to generate the populations and select the solutions. According to the MathWorks's Documentation [79], a brief flowchart of the GA is shown in Fig. 4-20. The GA firstly generates a random initial population, in which each design parameter is distributed randomly within the corresponding design space shown in Table 4-4. Performance of each individual will be predicted to evaluate the objective function (OF). According to their OF, the individuals with better OF will be selected as parents. Then, those parents can create children using Elite (population with top OF), Crossover (combination of design variable vectors of a pair of parents), and Mutation (random change to a single parent). In the Crossover, at each coordinate of the child vector, the algorithm randomly selects gene at the same coordinate from one of the two parents and combines it to a child. In the Mutation, the algorithm generates a child by randomly changing (stays in the design bounds) the genes of one parent. After evaluating population of the children, the iteration of the above sections will be continued until reaching the convergence criteria.

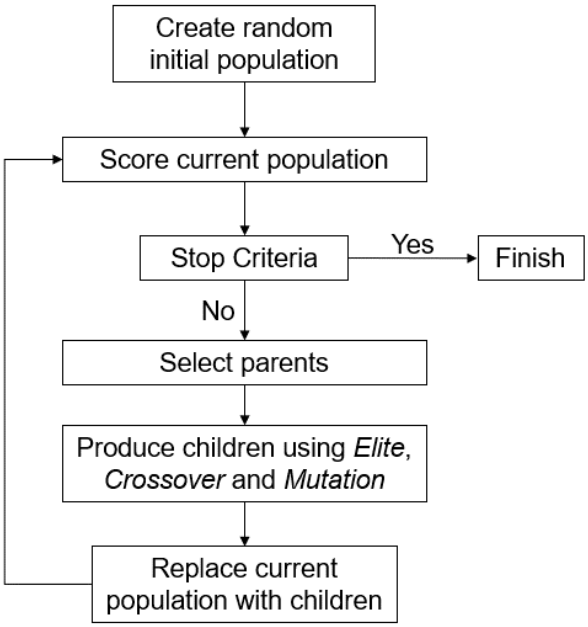

Fig. 4-20 Workflow of GA

Table 4-6 Independency check of population size and tolerance in Loop 2

Tolerance	0.01			0.001			0.0001		
	OF2 [m]	N_f [min^{-1}]	N_r [min^{-1}]	OF2 [m]	N_f [min^{-1}]	N_r [min^{-1}]	OF2 [m]	N_f [min^{-1}]	N_r [min^{-1}]
Population Size=40	4.4	1204.1	837.5	4.4	1213.1	817.9	4.6	1148.0	983.4
Population Size=100	4.3	1244.6	739.2	4.4	1270.9	682.6	4.3	1165.2	908.0
Population Size=160	4.3	1165.8	907.2	4.3	1202.2	829.0	4.3	1209.0	813.8

4.3.4 GA settings

In order to find appropriate settings for GA in Loop 1 and 2, optimization of rotational speeds for the existing rotors is firstly conducted with various population size and tolerance. The tolerance means a relative change of best value between adjacent generations. The optimized results of objective function OF2, rotational speeds of front N_f and rear N_r rotors for the various settings in Loop 2 are summarized in Table 4-6. It can be easily found that population size of 160 can obtain more stable results in the OF2. Since the tolerance of 0.001 and population size of 160 can achieve the similarly optimal solutions with less time, this setting will be employed in the Loop 2. Even though the population size is chosen as 160 for only two parameters in Loop 2, it should be noted that the GA searches an optimal solution in a very broad design space (from about $0.4N_d$ to nearly $1.3N_d$). On the other hand, for Loop 1, the population sizes in optimization of rear rotor and in optimization of front and rear rotors are set as 180 and 360 respectively, where the design space (same with DOE space shown in Table 4-4) is relatively small.

Some main settings of GA in this study are summarized in Table 4-7. It should be noted that the maximum number of generation is set to 10 for the both Loops 1 and 2 for the sake of time-saving; in some cases, the convergence referring the criteria (tolerance against the best design) is not perfectly obtained, meaning that there is still some possibility to find more optimized solution. However, even with such imperfect optimization, it is believed that the effectiveness of the present optimization strategy in terms of the energy saving pump design would be presented, as will be shown in the next section.

Table 4-7 Main settings of the GA

	Optimization of Rear Rotor		Optimization of Front and Rear Rotor	
	Loop 1	Loop 2	Loop 1	Loop 2
Number of Parameters	9	2	18	2
Population Size	180	160	360	160
Tolerance	0.0005	0.001	0.0005	0.001
Crossover Rate	0.8			
Mutation Rate	0.01			

4.4 Optimization of rotors in contra-rotating axial flow pump

Combining with the performance prediction models and the genetic algorithm (GA), design optimizations are now conducted for the rear rotor and for the both of front and rear rotors separately to achieve the optimal solution of energy saving with RSC in contra-rotating axial flow pump.

4.4.1 Problem setting: system resistance

The pump operation point is determined at the intersection between the pump head curve and system resistance curve. Therefore, in the practical application of rotational speed control (RSC), it is necessary to consider the system resistance. Generally, the system resistance H_R is defined as follows:

$$H_R = H_0 + \zeta_s Q^2 \tag{4-22}$$

where H_0 is the necessary head of pump which should depend upon the application, ζ_s denotes the system resistance coefficient with fully opened valve, and Q means the volumetric flow rate

in $[m^3/s]$.

In the present study, a system resistance H_R for the pressurized liquid is considered, where the necessary head H_0 and system resistance coefficient ζ_s are assumed as 3m and $166 s^2/m^5$ respectively. It should be noted that this is identical to the System resistance 2 used in Chapter 3.

4.4.2 Optimal designs and performance predictions

Based on the assumed system resistance, through the proposed performance prediction models and the GA, the design optimization is operated firstly for only the rear rotor ($\mathrm{Rear_{Opt}}$), and then for the both of front and rear rotors ($\mathrm{FR_{Opt}}$). Figure 4-21 shows the convergence histories of objective function OF1 in $\mathrm{Rear_{Opt}}$. In Fig. 4-21 (a), the population averaged OF1 is plotted against with generation for $\mathrm{Rear_{Opt}}$. The averaged OF1 is significantly reduced at the early stage of optimization, and the relatively small change can be observed before the optimization stopped. However, as displayed in Fig. 4-21 (b), the best OF1 in the rear rotor optimization has not achieved sufficient convergence, which indicates that the result with the rear rotor optimization may be close but not to the optimal solution. However, it is the best solution in a total population with 1980 designs selected by the genetic algorithm (GA); it apparently shows the less input power solution.

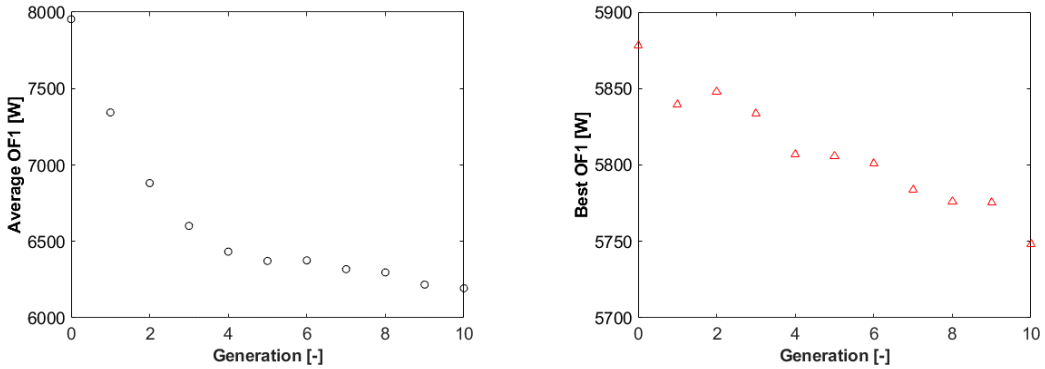

(a) Averaged OF1 (b) Best OF1

Fig. 4-21 Convergence of objective function OF1 in rear rotor optimization

Figure 4-22 demonstrates the convergence histories of objective function OF1 in optimization for both of front and rear rotors. Both of the population averaged OF1 (shown in Fig. 4-22 (a)) and the best OF1 (shown in Fig. 4-22 (b)) have obtained convergence before optimization stopped. Compared with the best value of the initial population in Fig. 4-22 (b), only about 60W is decreased in the objective function OF1 of FR_{Opt}. Such relatively small improvements may be the result of large population (population size=360) in a limited design space for the single objective function.

The optimal designs and the original design (RR3) are summarized in Table 4-8 and their shapes are illustrated in Fig. 4-23.

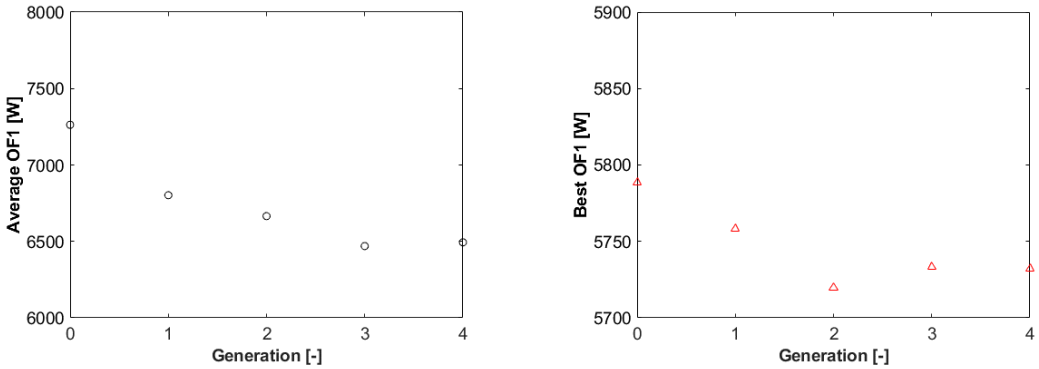

(a) Averaged OF1 (b) Best OF1

Fig. 4-22 Convergence of objective function OF1 in optimization for both of front and rear rotors

Table 4-8 Design parameters of RR3-type and optimal designs

		RR3	Rear_{Opt}	FR_{Opt}
Front Rotor	Hub Inlet Blade Angle $\beta_{B1,hub}$ [°]	63		65.553
	Section 2 Inlet Blade Angle $\beta_{B1,S2}$ [°]	73.41		72.895
	Section 3 Inlet Blade Angle $\beta_{B1,S3}$ [°]	79.8		81.476
	Section 4 Inlet Blade Angle $\beta_{B1,S4}$ [°]	84.06		80.573
	Tip Inlet Blade Angle $\beta_{B1,tip}$ [°]	87.12		90.754
	Tip Axial Stacking Position $z_{tip,stack}$ [m]	0		0.001
	Tip Circumferential Stacking Position $\theta_{tip,stack}$ [Rad]	0		0.131
	Hub Solidity σ_{hub} [-]	1.29		1.006
	Tip Solidity σ_{tip} [-]	0.7		0.756
Rear Rotor	Hub Inlet Blade Angle $\beta_{B1,hub}$ [°]	69.63	65.696	70.630
	Section 2 Inlet Blade Angle $\beta_{B1,S2}$ [°]	70.88	73.072	74.471
	Section 3 Inlet Blade Angle $\beta_{B1,S3}$ [°]	72.31	71.747	71.646
	Section 4 Inlet Blade Angle $\beta_{B1,S4}$ [°]	73.67	72.775	73.411
	Tip Inlet Blade Angle $\beta_{B1,tip}$ [°]	80.17	76.275	76.650
	Tip Axial Stacking Position $z_{tip,stack}$ [m]	0	0.009	0.008
	Tip Circumferential Stacking Position $\theta_{tip,stack}$ [Rad]	0	0.193	-0.020
	Hub Solidity σ_{hub} [-]	1.008	1.137	0.905
	Tip Solidity σ_{tip} [-]	0.72	0.537	0.585

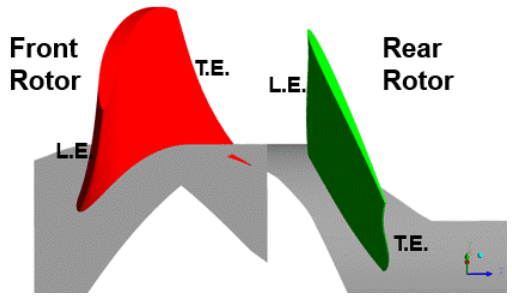

(a) RR3 rotors

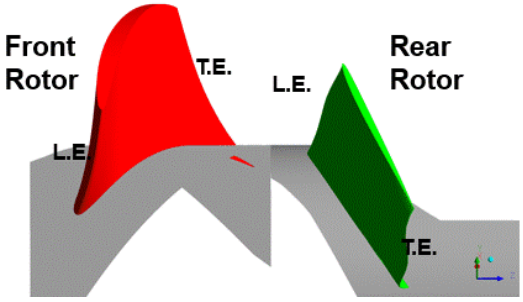

(b) $\mathrm{Rear}_{\mathrm{Opt}}$ rotors

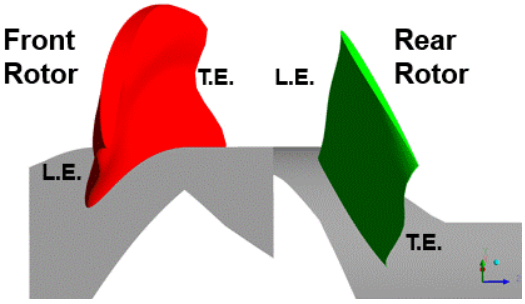

(c) $\mathrm{FR}_{\mathrm{Opt}}$ rotors

Fig. 4-23 Shapes of rotors

In order to compare with the optimal designs, the performance prediction of original RR3 rotors with rotational speed control (RSC) has been obtained at various flow rates (from $0.5Q_d$ to $1.2Q_d$). Figure 4-24 illustrates (a) the rotational speed information of RSC, (b) performances, (c) total theoretical head and the mixing loss head evaluated by the performance prediction model (Model). In (b) and (c), the results of CFD are also plotted to check the validity of the performance prediction model.

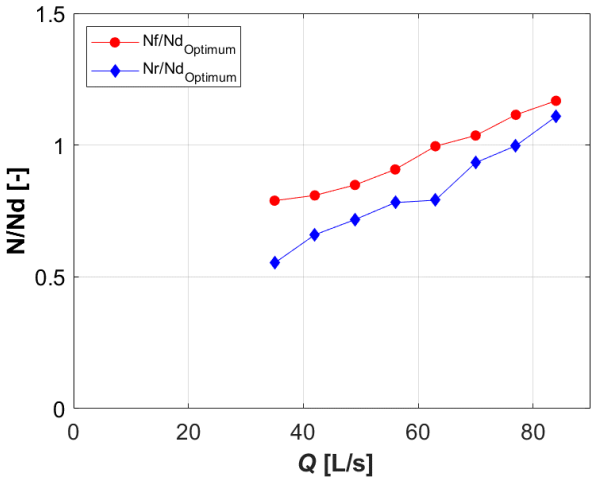

(a) Rotational speed of front and rear rotors

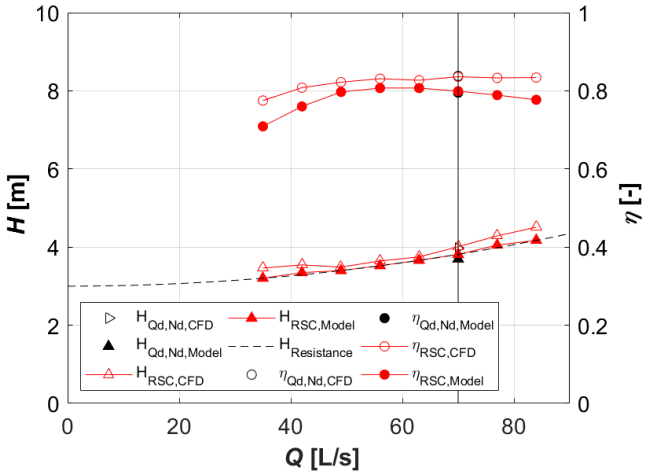

(b) Total head and total efficiency

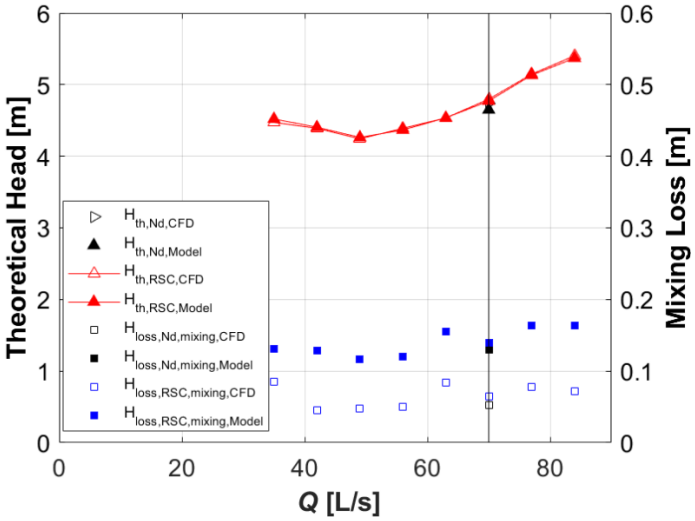

(c) Total theoretical head and mixing loss head

Fig. 4-24 Performances of original RR3-type rotors

As shown in Fig. 4-24 (b), very small discrepancies can be observed in the head and efficiency curves calculated by CFD and the Model. Basically, the Model slightly overestimates the head and slightly underestimates the efficiency. In Fig. 4-24 (c), very good agreement can be found in the theoretical head curve predicted by CFD and the Model, while mixing loss head evaluated by the Model is larger than that of CFD. It seems that the good prediction of theoretical head and over-evaluation of mixing loss head make the Model under-evaluate the efficiency and over-predict the head.

It can also be easily found that the head curve with RSC can well satisfy the assumed system resistance in a broad range of flow rate. At the same time, the efficiency is also kept in a very high region (similar efficiency with the design point). This implies the effectiveness of the rotational speed control method (RSC) in terms of the energy saving.

Next, the results of design optimization of rear rotor using the performance prediction model and the genetic algorithm (GA) are shown in Fig. 4-25. The performances evaluated by CFD are also plotted in the figures. As shown in Fig. 4-25 (b), the head predicted by the Model agrees well with that of CFD, while the Model's efficiency is slightly underestimated compared with CFD's efficiency. From Fig. 4-25 (c), a little overestimation of theoretical head can be found in the Model, which may be the main reason for underestimation of efficiency in the Model. It is still observed that the RSC can modify the head to meet the system resistance with high efficiency in a wide range of flow rate.

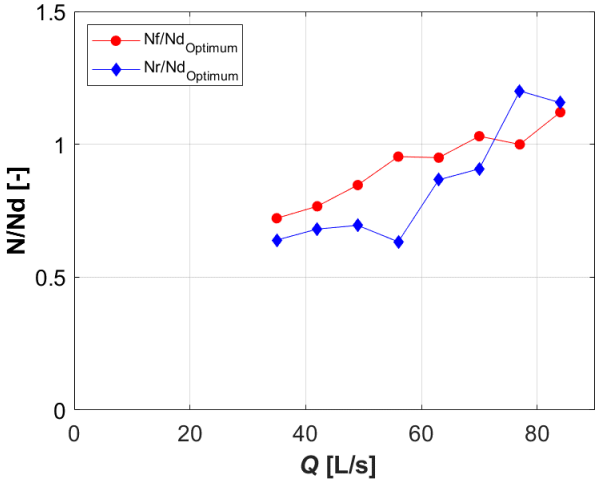

(a) Rotational speed of front and rear rotors

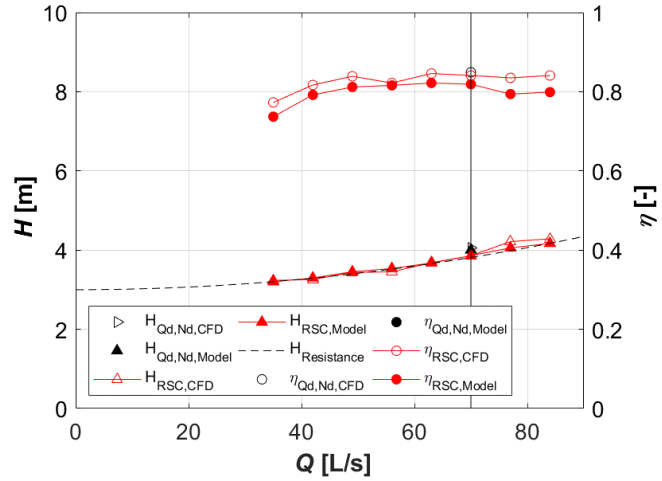

(b) Total head and total efficiency

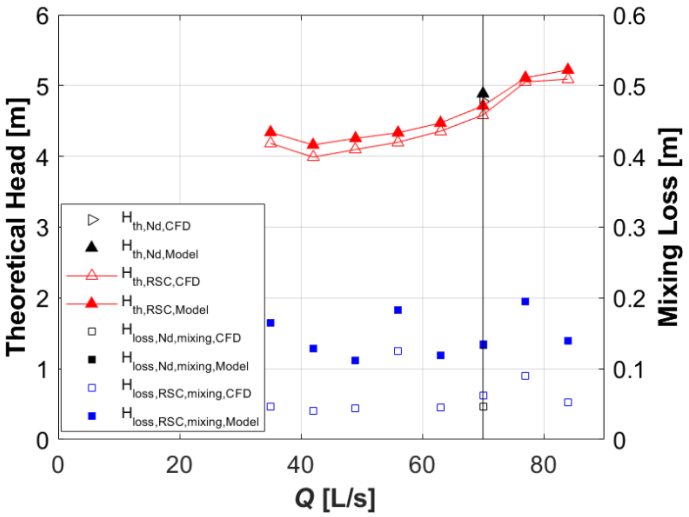

(c) Total theoretical head and mixing loss head

Fig. 4-25 Performance of optimal design for rear rotor

In order to understand the reason why the Model overestimates the theoretical head, the normalized discrepancy y in the rear rotor is checked using the CFD results. In Fig. 4-26, the black open circles represent y determined by ANN, while the red open circles mean y re-calculated by CFD simulations with design rotational speed. The red solid circles denote y calculated by CFD simulations at various flow rates with RSC. As we can see, the red solid circles are located around the red open circles, indicating the effectiveness of our strategy using results under conditions with design rotational speed to predict results under conditions with off-design rotational speed. Since the y is underestimated by the ANN, the Model tends to over evaluate the theoretical head.

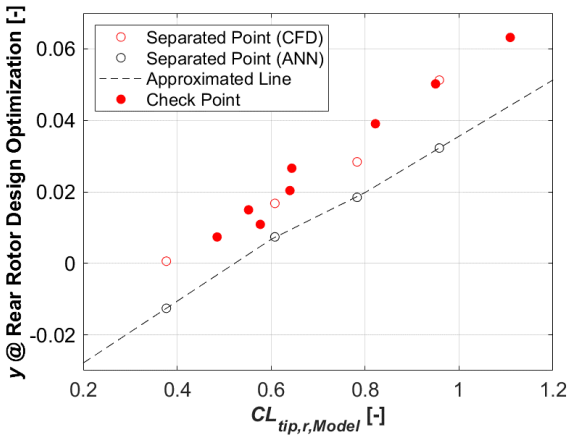

Fig. 4-26 Normalized discrepancy y in performance prediction model for rear rotor optimization

Figure 4-27 shows the performances and RSC information of the optimal design for both front and rear rotors determined by the performance prediction model and the GA. As demonstrated in Fig. 4-27 (b), relatively large discrepancies (about 10%) exist in the head and efficiency evaluated by CFD and the Model at the extreme off-design flow rates ($0.5Q_d$, $1.2Q_d$). It can also be observed that the Model underestimates the head at higher flow rates while over evaluates the head at lower flow rates. Similar tendency can also be observed in the theoretical head predictions of the Model shown in Fig. 4-27 (c). Therefore, it seems that the rough prediction of theoretical head in the Model could be main reason for the similarly rough evaluation of Model's head.

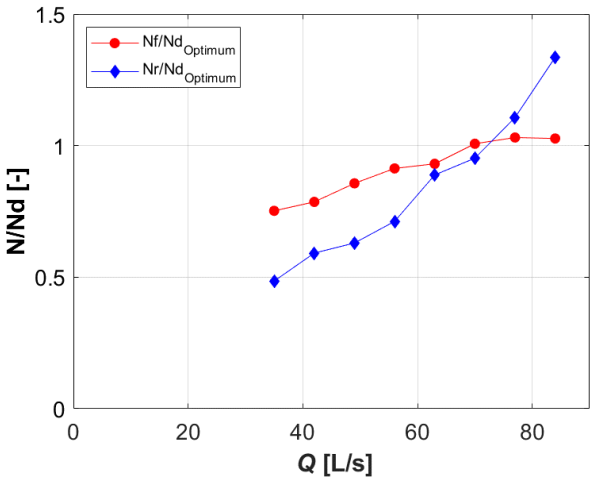

(a) Rotational speed of front and rear rotors

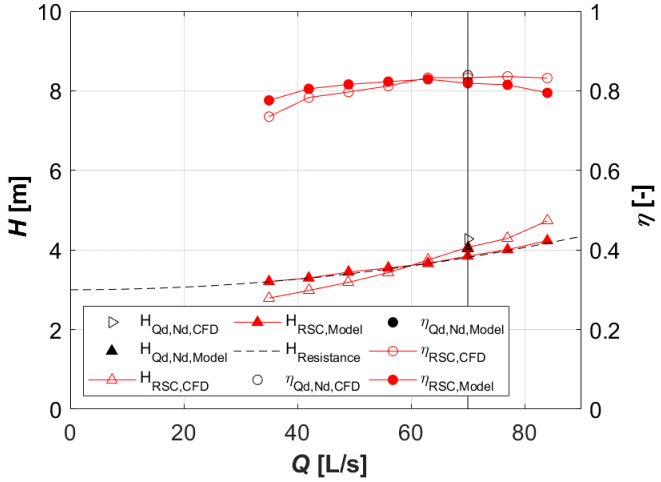

(b) Total head and total efficiency

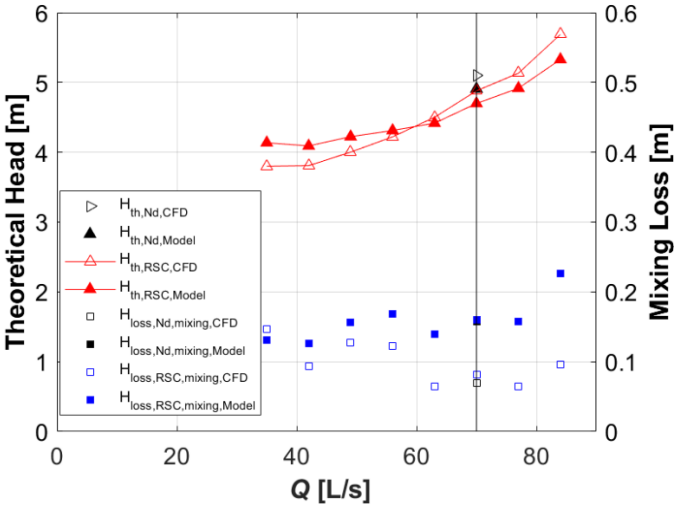

(c) Total theoretical head and mixing loss head

Fig. 4-27 Performance of optimal design for front and rear rotors

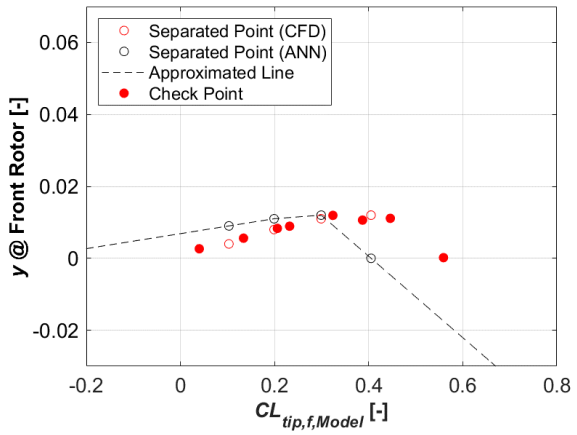

(a) Front rotor

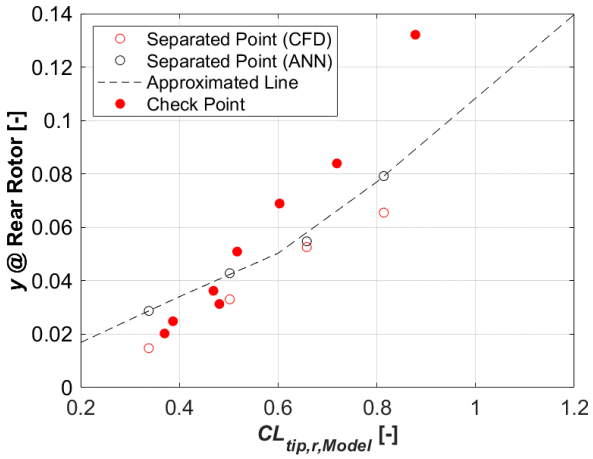

(b) Rear rotor

Fig. 4-28 Normalized discrepancy y in performance prediction model for optimization of front and rear rotors

In Fig. 4-28, the normalized discrepancies y of front and rear rotors are plotted with CFD results to compare with the y based on ANN. As we can see, at the range of low tip lift coefficient (results at large flow rates), in both of front and rear rotors, the y of ANN (black dash line) is a little larger than the y of CFD (red solid circles). Both ANN's overestimation of y could result in the underestimation of theoretical head at large flow rates. It is also found that, at the range of high tip lift coefficient (results at low flow rates), the y of ANN (black dash line) is lower than the y of CFD (red solid circles) in both of rotors. However, it should be noted that the theoretical head $H_{th,f}$ of front rotor contributes dominantly to the total theoretical head $H_{th,t}$ at low flow rates.

Therefore, the underestimation of y based on ANN in front rotor seems to be the possible factor causing the over-evaluated total theoretical head at low flow rates.

However, it should also be noted that the normalized discrepancy y is a result of ANN as well as flow velocities calculated by basic equations in the Model. At the small flow rates, the blade-rows interactions are usually strengthened [56], which is not considered in the prediction model in the ANN's prediction. Furthermore, reverse flows may also occur in the hub and tip region between front and rear rotors at low flow rates [58]. This may significantly affect the flow prediction of the Model, since it is constructed assuming no-reverse flows.

In order to identify the blade-rows interaction and reverse flow, CFD simulations for only front rotor (F) have been conducted to compare with simulations for front and rear rotors (FR) at various flow rates with different rotational speed. Figure 4-29 shows the area-averaged axial velocity and mass-averaged swirling velocity at five sample positions from hub to tip along the trailing edge (T.E.) of front rotor in the CFD simulations. Open circles show the results with only the front rotor (F), while the closed circles represent those of front and rear rotors simulation (FR). As we can see, at large flow rates (70L/s with RSC, 77L/s with design rotational speed N_d), nearly the same velocities can be observed at all 5 positions in the two simulations, which indicates negligible blade-rows interaction. At low flow rates (35L/s with RSC, 42L/s with RSC, 56L/s with N_d), large discrepancies of velocities are observed in the hub region, where the reverse flow exists. The existence of reverse flow in the hub region at T.E. of front rotor changes the meridional shape of streamtube, which may be the main reason for the error in the theoretical head prediction at very low flow rates.

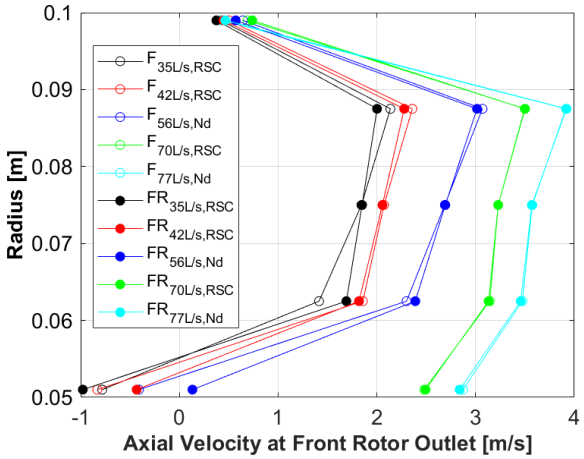

(a) Axial velocity

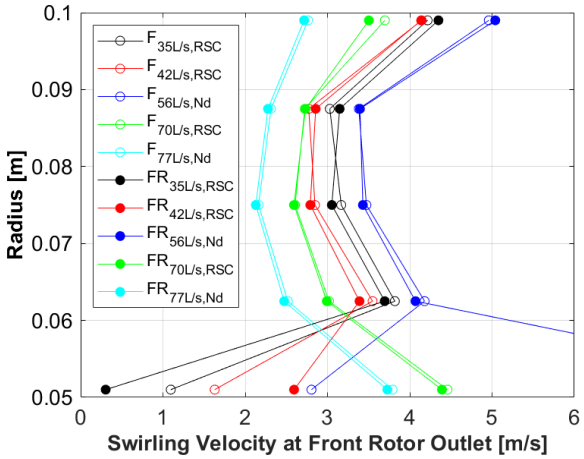

(b) Circumferential velocity

Fig. 4-29 Velocities at front rotor outlet

4.4.3 Energy saving performances

The input power P_{Input} is employed to reflect the energy consumption at each flow rate for the three designs of rotors: original rotors RR3 ($\mathrm{Rotor_{RR3}}$), optimal design of rear rotor ($\mathrm{Rotor_{Rear,Opt}}$), optimal design of front and rear rotors ($\mathrm{Rotor_{FR,Opt}}$). The input power P_{Input} is written as:

$$P_{Input} = \rho g Q H_{th,t} \tag{4-23}$$

where ρ denotes the flow density in $[\mathrm{kg/m^3}]$, g represents the gravity in $[\mathrm{m/s^2}]$, Q means the volumetric flow rate in $[\mathrm{m^3/s}]$, and $H_{th,t}$ is the total theoretical head in [m].

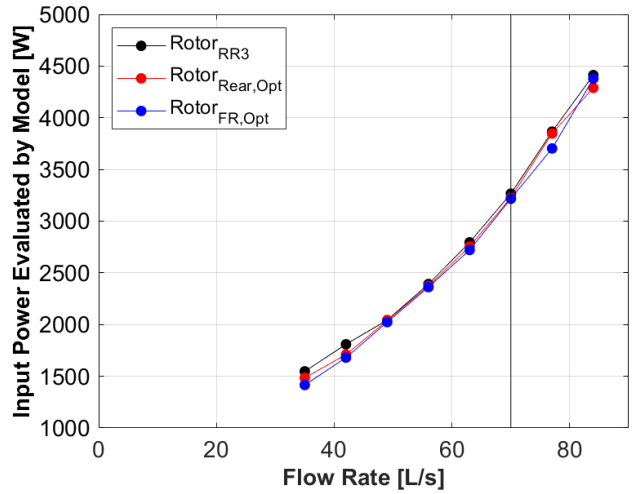

(a) Input power predicted by performance prediction model

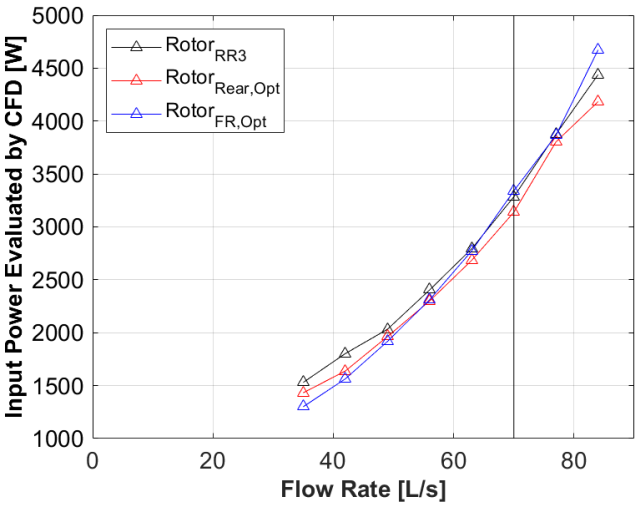

(b) Input power predicted by CFD

Fig. 4-30 Energy saving performance

Figure 4-30 (a) shows the input power of the three designs predicted by the Model. It can be found that the original design of RR3 rotors (black circle) consumes the most amount of power at all the calculated flow rates, while the optimal design of front and rear rotors (blue circle) generally consumes the least energy, and the optimal design of only rear rotor (red circle) can achieve a medium energy-saving performance. However, it should be noted that the optimal

design of each rotor may not be the optimal solution due to the limited number of generations in optimization process as mentioned before. This indicates that the energy saving performance may be further improved by conducting optimization with more generations. Even considering this fact, these results can still indicate that, by considering the simultaneous rotational speed controls of front and rear rotors at the design stage, the rotors with better energy saving performance can be designed. The effectiveness of our optimal designs using the performance prediction model and the GA is also shown to realize the fast optimal design.

Figure 4-30 (b) illustrates the energy consumption of the three designs evaluated by CFD. We can still find that, compared with optimal design of rear rotor (red triangle), the original design of RR3 (black triangle) needs more input power. This agree well with the result of performance prediction model. However, at large flow rates, the optimal design of front and rear rotors (blue triangle) shows higher input power, which is in contrast to the result of the Model. As mentioned before, the discrepancy of energy consumption for the optimal design of front and rear rotors evaluated by CFD and the Model may be the result of the following factors: a little errors in both ANN's prediction at large flow rates, and the Model calculation error in flows caused by the existence of reverse flow.

4.5 Summary

In the present chapter, performance prediction models have been constructed for the design optimization of rotors in contra-rotating axial flow pump for energy saving with rotational speed control (RSC). By using the proposed models and the genetic algorithm (GA), design optimizations have been conducted for only the rear rotor and for the both of front and rear rotors separately. Then, CFD simulations have also been performed for three designs (the original rotors

RR3, optimal design of rear rotor, optimal design of front and rear rotors) to compare with the performance prediction model. Main findings are summarized as follows:

1) Metamodels have been established only using CFD simulations at near-design flow rates with design rotational speed for various blade parameters, which requires less computational cost with good enough accuracy.
2) By using the radial equilibrium equation, conservation equations of mass and rothalpy, empirical deviation angle equation, empirical equation including metamodel, empirical cascade loss equation, mixing loss equation and empirical other loss including metamodel, effective performance prediction models have been established toward energy saving with RSC in contra-rotating axial flow pump. In fact, by using the proposed performance prediction models and GA, design optimizations of only rear rotors, both of front and rear rotors have been separately performed to satisfy a system resistance for energy saving with RSC in contra-rotating axial flow pump. According to the performance prediction model, the optimal design of both front and rear rotors shows the best performance in the energy saving at wide range of flow rate, optimal design of only rear rotor achieve a medium energy-saving performance, while the original design of RR3 rotors consumes the most amount of power. This indicates that, by considering the simultaneous rotational speed controls of front and rear rotors at the design stage, the energy saving design of the rotors can be obtained. The effectiveness of our optimal designs using the performance prediction model and the GA is also shown to realize the fast optimal design.
3) Compared with the CFD simulations, the performance prediction model for rear rotor optimization shows good enough agreement in the results of total head, total efficiency and total theoretical head, while the performance prediction model for the optimization of front and rear rotors has about 10% discrepancies in the results of total head and total

theoretical head at the extreme off-design flow rates. Such discrepancy may be the result of errors in both ANN's prediction at large flow rates and Model calculation error at low flow rates. The latter seems to be due to the occurrence of reverse flow.

Chapter 5

Conclusions

Compared with conventional high-specific-speed axial flow pumps, the contra-rotating axial flow pump can achieve better cavitation performance and compact size. In the development of contra-rotating axial flow pump, the following issues have not been well solved: loss generation mechanism in rear rotor, simultaneous rotational speed control (RSC) and optimal design of rotors for energy saving with RSC. Therefore, the aim of the present study has been to solve above problems to achieve more energy-saving design with rotational speed control (RSC) method for contra-rotating axial flow pump.

In Chapter 1, the objective of the present study has been introduced by describing the problems in the design and operation of contra-rotating axial flow pump.

In Chapter 2, the main objective is to investigate the loss generation mechanism in rear rotors of contra-rotating axial flow pump, which could be meaningful in designing a pump with better performance at the design point as well as the off-design conditions. Three models with different specific-speed (low, medium and high) rear rotors are designed with the conventional method, and the flow fields are simulated by unsteady RANS simulation. According to the unsteady RANS simulations, it is shown that better efficiency of rear rotor is achieved in the low specific speed design and total efficiency takes the maximum value with the medium specific speed of rear rotor. It is also found that the corner separation at the root of rear rotor blade becomes significant with the decrease of specific speed despite the increase of rear rotor efficiency. So the loss generation

mechanism in rear rotor needs to be investigated. Two loss evaluation methods based on the entropy production rate and the material-derivative of rothalpy are employed. Although the both methods qualitatively estimate the total loss through the rear rotor, the material-derivative of rothalpy gives much better quantitative prediction of the losses in the examined cases. Two distinct flow features are observed in the rear rotor, the corner separation at the hub corner of blades and the tip leakage vortex (TLV), both of which are responsible for the loss generation. With the evaluation of local loss generation based on the material-derivative of rothalpy, the loss contribution of corner separation is found to be very small compared with that due to the TLV. The TLV structure in high specific speed rear rotor shows the strong interaction with the leading edge of adjacent blade, which seems to strengthen the blockage effect in the tip region. This is relieved in the lower specific speed rear rotor, resulting in the achievement of higher efficiency with it.

In Chapter 3, the main objective is to establish and validate the performance prediction model for contra-rotating axial flow pump to determine the optimum rotational speeds of rotors under rotational speed control (RSC). The established model is expected to be applied for the energy saving operations of contra-rotating axial flow pump at off-design flow rates. In order to construct an effective performance prediction model, the flow in the contra-rotating axial flow rotors has been assumed as steady, non-viscous, axisymmetric, non-reverse and uniform with no swirl at front rotor inlet. Then, by considering radial equilibrium condition, conservation of rothalpy and mass, empirical deviation angle, flow velocities could be determined. Since blade-rows interaction exists between the front and rear rotors, an empirical modification is also included in the calculation of rear rotor theoretical head using the lift coefficient at rear rotor blade tip. In the evaluation of losses, two types of losses have been considered: cascade loss and other losses. The

cascade loss is directly evaluated by employing an empirical cascade loss model while the other losses are modelled according to the blade tip lift coefficient. Finally, performance could be determined. Experimental and CFD results are employed to validate the proposed prediction model. It is found that the proposed model shows good enough accuracy in predicting performances of contra-rotating axial flow pump under RSC in broad flow rate range. On the other hand, the proposed model also shows limitations in the conditions with high-pressure rise at very low flow rates. The occurrence of reverse flow may be unavoidable at such flow rates even with RSC. Furthermore, an energy saving application of the proposed model is also illustrated for two typical system resistances. Compared with the traditional valve control method, the RSC method optimized by the proposed performance prediction model can well adjust the pump head to satisfy the system resistance curves at wide flow rate range with significantly improved efficiency. Good agreements are obtained between the proposed model and the CFD simulations, showing the effectiveness of the proposed performance prediction model.

In Chapter 4, the main objective is to re-construct performance prediction model and to conduct the design optimization of rotors using the proposed models for energy saving with RSC in contra-rotating axial flow pump. The strategy of the performance prediction models is to use results under conditions with design rotational speed to predict results under conditions with off-design rotational speeds. Therefore, the metamodel is established only using CFD simulations at near-design flow rates with design rotational speed for various blade design parameters, which requires less computational cost while provides good enough accuracy. Then, flow velocities are calculated with previously described four basic equations: radial equilibrium equation, conservation equations of mass and rothalpy, and empirical deviation angle equation. Because of the complex 3D flows in the rotors and blade-rows interactions, modification in the theoretical

head need to be performed, which is made by introducing the result of the metamodel. The losses in the present models include cascade loss, other losses and mixing loss downstream the rear rotor. The cascade loss is calculated using the empirical cascade loss model, the other losses are determined with an equation derived from the result of metamodel for total losses in each rotor, and the mixing loss is evaluated by considering the non-uniform flow velocities at the rear rotor outlet. After the above all, performance prediction becomes available. Using the proposed performance prediction models and the genetic algorithm (GA), design optimizations have been conducted for only rear rotor and for both of front and rear rotors in contra-rotating axial flow pump separately. Compared with the CFD simulations, the performance prediction model for rear rotor optimization shows good enough agreement in the results of total head, total efficiency and total theoretical head, while the performance prediction model for the optimization of front and rear rotors has shown about 10% discrepancies in the results of total head and total theoretical head at the extreme off-design flow rates. Such a large discrepancy may be the result of errors in both ANN's prediction at large flow rates and Model calculation error in flows caused by the occurrence of reverse flow appears on the hub surface in the gap between front and rear rotors. It should be also noted that mixing loss determined by the performance prediction model is usually overestimated, which may be the result of limitation of flow angle determination using the empirical deviation angle equation. As for the energy saving performance, according to the performance prediction model, the optimal design of both front and rear rotors shows the best performance in the energy saving at wide range of flow rate, optimal design of only rear rotor achieve a medium energy-saving performance, while the original design of RR3 rotors consumes the most amount of power. This indicates that, by considering the simultaneous rotational speed controls of front and rear rotors at the design stage, the energy saving performance can be enhanced. Both of the CFD and the performance prediction model indicates that, compared with

the original RR3 rotors, the optimal design of rear rotor can consume less power to satisfy the systems resistance in a wide range of flow rate, where higher efficiency is kept. Even though, because of the accuracy of the performance prediction model, non-negligible discrepancy can be observed in energy saving evaluated by the model and CFD for the optimal design of front and rear rotors at the extreme off-design flow rates, the effectiveness of our optimal designs using the performance prediction model and the GA is still shown; the fast optimal design will be realized by utilizing the proposed method.

Through the above researches, some issues are remained and need to be solved as the future topics: improvement of accuracy of performance prediction model, optimal solutions with more design parameters in wider space, and so on.

As mentioned in Chapter 3, the performance prediction model toward rotational speed control (RSC) of rotors in contra-rotating axial flow pump shows limitations in the conditions with high-pressure rise at the very low flow rates, where reverse flows exist. In Chapter 4, large discrepancies can be observed in the performances at the very low flow rate between CFD and the performance prediction model, in which reverse flows also occur. These limitations in the performance prediction models may be the result of too simplified flow assumption in the models. Actually, in the conditions with partial loads even with RSC, reverse flow could also occur in many regions: the hub at outlet of front rotor, tip regions at inlet of front and rear rotors. Therefore, it seems to be necessary to include the effect of reverse flows in the performance prediction model to improve its prediction accuracy. Furthermore, it has been known that the flow in the tip region has significant impact on the performance of contra-rotating axial flow pump. Therefore, prediction accuracy could also be improved when the flow in tip region is more appropriately determined. As an example, considering the casing wall blockage effect seems to improve the

flow condition near the tip, which may be effectively included in the metamodel. For the above two reasons, to consider the reverse flow and the casing wall blockage effect may be the future topic for the construction of more reliable performance prediction model toward energy saving with RSC in contra-rotating axial flow pump.

In the present design optimizations, to simplify the problem of optimization, the design space of design parameters is not taken to be very wide, which may be insufficient for the genetic algorithm (GA) to search solutions for more global optimal design. Furthermore, only the design parameters related to blade twist, sweep, lean and length are considered in the present study, while many other design variables are kept constant, such as camber line profile, thickness distribution, the ratio of hub and casing, and so on. These parameters are believed to have significant effect on the performances. Therefore, it could be possible to further improve the energy-saving performance of contra-rotating axial flow pump with conducting design optimization by considering more design variables in a wider design space. On the other hand, in the present optimization, a single objective function is defined by assuming that the pump will be operated mainly at low flow rates. The optimal design will not be good enough when the operation condition is changed. Such a problem could be solved by employing multi-objective optimization, in which reasonable solutions can be selected from a set of Pareto optimal solutions according to the design requirement. Then, multi-objective optimization with more design variables in a wider design space may be also conducted in future study.

Acknowledgement

Throughout the study for the doctoral thesis, I have received a great deal of support.

Firstly, I would like to express my sincere gratitude to my supervisor Professor Satoshi Watanabe for his invaluable advice, kindly guidance and infinite patience. He gave me the chance to study in Kyushu University and helped me open the door to the research. Many problems in my study have been solved with his immense knowledge and plenty of experience, without which this thesis would not be achievable.

I would like to acknowledge the rest of my thesis committee: Professor Masato Furukawa and Professor Jun Ando, for their insightful comments and suggestions, which prompted me to expand my research from various perspectives.

My sincere thanks also go to Professor Shinichi Tsuda and Professor Yusuke Katayama, who discussed many issues with me and provided me further support in my research and my living in Japan.

I would also like to thank all members and staffs in the Flow Control Systems Laboratory of Kyushu University. They are very kind to me and often play softball with me.

Last but not the least, I would like to say thank you to my parents, wife and daughter for supporting and encouraging me.

De Zhang

2020-1-12

Nomenclature

Chapter 1		
A	Sectional area	$[\mathrm{m}^2]$
B	Height of blade	[m]
e	Specific internal energy	$[\mathrm{m}^2/\mathrm{s}^2]$
g	Gravity	$[\mathrm{m}/\mathrm{s}^2]$
H	Head	[m]
H_d	Design head	[m]
I	Rothalpy	$[\mathrm{m}^2/\mathrm{s}^2]$
N	Rotational speed	$[\mathrm{min}^{-1}]$
N_D	Nondimensional specific speed	
N_S	Dimensional specific speed	$[\mathrm{min}^{-1}, \mathrm{m}^3/\mathrm{min}, \mathrm{m}]$
p	Static pressure at inlet	[Pa]
p_v	Vapor pressure	[Pa]
Q_d	Design flow rate	$[\mathrm{m}^3/\mathrm{s}]$ or $[\mathrm{m}^3/\mathrm{min}]$
U	Reference velocity	[m/s]
R	Radius	[m]
W	Relative velocity	[m/s]
Greeks		
ϑ	Angle between exit flow passage and rotating axis	[º]
ρ	Density of fluid	$[\mathrm{kg}/\mathrm{m}^3]$
σ	Cavitation number	
ϕ	Flow coefficient	
ψ	Head coefficient	
ω	Angular rotational speed	[Rad/s]
Subscripts		
1	At inlet of rotor	
2	At outlet of rotor	
H	At blade hub	
T	At blade tip	
Chapter 2		
C_R	Loss coefficient based on material derivative of rothalpy	
D	Diameter	[m]
D_h	Hub diameter	[m]
D_t	Tip diameter	[m]

e	Specific internal energy	[m^2/s^2]
g	Gravity	[m/s^2]
H	Head	[m]
H_{loss}	Hydraulic loss	[m]
I	Rothalpy	[m^2/s^2]
$\vec{n}$	Unit normal vector	
Δn	Distance between first and second mesh points near the wall	[m]
N	Rotational speed	[min^{-1}]
N_s	Dimensional specific speed	[min^{-1},m^3/min, m]
p	Static pressure	[Pa]
p_t	Total pressure	[Pa]
P	Power	[W]
$\vec{q}$	Heat flux density vector	$[W/m^2]$
Q	Volumetric flow rate	[L/s]
r	Radius or meridional radius	[m]
s	Entropy per unit mass	[J/(kg K)]
S	Surface	[m^2]
$\dot{S}$	Entropy production rate	[W/(K·m^3)]
$\dot{S}_D$	Entropy production by direct dissipation	[W/(K·m^3)]
$\dot{S}_T$	Entropy production by turbulent dissipation	[W/(K·m^3)]
t	Time	[s]
T	Torque or temperature	[N·m] or [K]
Δt	Time-step in simulations	[s]
u, v, w	Velocity components	[m/s]
$\bar{u}$, $\bar{v}$, $\bar{w}$	Mean velocity components	[m/s]
u', v', w	Fluctuating velocity components	[m/s]
U	Peripheral velocity (U=$r\cdot\omega$)	[m/s]
v_θ	Swirling velocity at front rotor outlet	[m/s]
W	Relative velocity	[m/s]
W_i, W_j	Relative velocity tensor	[m/s]
x', y'	Coordinates in rotor-fixed frame	[m]
y^+	Dimensionless distance from the wall	
y^+_{min}	Minimum y^+ on blades	
$\overline{y^+}$	Area averaged y^+ on blades	

Greeks		
γ	Blade stagger angle	[º]
σ	Cascade solidity	
ε	Dissipation rate of turbulent kinetic energy	[m^2/s^3]
η	Efficiency	
η_{loss}	Loss contribution	
μ	Dynamic viscosity of fluid	[kg/(m·s)]
ν	Kinematic viscosity of fluid	[m^2/s]
ξ_W	Normalized relative velocity	
ρ	Density of fluid	[kg/m^3]
τ	Tip clearance	[mm]
τ_w	Wall shear stress	[N/m^2]
Φ	Viscous dissipation	[W/m^3]
Φ/T	Entropy production by viscous dissipation	[$W/(K \cdot m^3)$]
Φ_E	Local dissipation by entropy production	[W/m^3]
Φ_R	Local dissipation by rothalpy change	[W/m^3]
Φ_Θ	Entropy production term	[$W\ K/m^3$]
Φ_Θ/T^2	Entropy production by heat transfer	[$W/(K \cdot m^3)$]
ω	Angular rotational speed of rotor	[rad/s]
Subscripts		
c	At casing	
d	At design point	
f	Front rotor	
r	Rear rotor	
t	Total of front and rear rotor	
Chapter 3		
C_L	Lift coefficient	
C_D	Drag coefficient	
D_c	Casing diameter	[m]
D_{eq}	Equivalent diffusion factor	
D_h	Hub diameter	[m]
g	Gravity	[m/s^2]
H	Head	[m]
H_0	Necessary head	[m]
H_{loss}	Mass-averaged loss head	[m]

H_R	System resistance head	[m]
$H_{t,d}$	Design total head	[m]
H_{th}	Theoretical head	[m]
i	Incidence angle	[°]
k	Empirical coefficient for deviation angle	
L	Shaft power	[W]
N	Rotational speed of rotors	$[\mathrm{min}^{-1}]$
N_d	Design rotational speed	$[\mathrm{min}^{-1}]$
N_s	Dimensional specific speed	$[\mathrm{min}^{-1}, \mathrm{m}^3/\mathrm{min}, \mathrm{m}]$
p	Static pressure	[Pa]
p_t	Total pressure	[Pa]
Q	Volumetric flow rate	$[\mathrm{m}^3/\mathrm{s}]$
Q_d	Design flow rate	[L/s]
r	Local radius	[m]
T	Torque of rotors	$[\mathrm{N} \cdot \mathrm{m}]$
v_a	Axial component of velocity	[m/s]
v_θ	Swirling component of absolute velocity	[m/s]
w	Relative velocity	[m/s]
y	Normalized discrepancy between theoretical heads evaluated by CFD and the model	
$y+$	Dimensionless distance from the wall	
Greeks		
β	Flow angle	[°]
β_b	Blade angle	[°]
γ	Blade stagger angle	[°]
δ	Deviation angle	[°]
δ_{m2}/l	Momentum thickness coefficient	
ζ_c	Cascade loss coefficient	
ζ_s	System resistance coefficient	$[\mathrm{s}^2/\mathrm{m}^5]$
η	Efficiency	
η_S	System efficiency	
ξ	Axial velocity change ratio	
ρ	Fluid density	$[\mathrm{kg}/\mathrm{m}^3]$
σ	Solidity	
$\psi_{loss,other}$	Coefficient of the other losses	
ω	Angular rotational speed of rotor	[rad/s]

Subscripts		
1	At inlet of rotor	
2	At outlet of rotor	
cascade	Related to cascade	
f	Front rotor	
FR	Only controlling front rotor speed	
hub	At blade hub	
m	Average of the variables	
opt	At the optimum condition	
r	Rear rotor	
ref	Reference variables	
RR	Only controlling rear rotor speed	
t	Total of front and rear rotors	
tip	At blade tip	
Chapter 4		
a, b, c	Constants in camber line formulation	
A	Sectional area	$[\mathrm{m}^2]$
C_D	Draft coefficient	
C_L	Lift coefficient	
D	Diameter	[m]
D_c	Casing diameter	[m]
D_{eq}	Equivalent diffusion factor	
D_h	Hub diameter	[m]
F_1	Function to determine the normalized discrepancy y	
F_2	Function to determine the other loss coefficient	
g	Gravity	$[\mathrm{m/s}^2]$
H	Head	[m]
H_0	Necessary head	[m]
H_{th}	Theoretical head	[m]
H_{loss}	Head loss evaluated by total pressure at the near-rotor cross sections	[m]
$H_{loss,r2,down}$	Loss head between downstream of rear rotor and outlet boundary	[m]
H_R	System resistance head	[m]
i	Incidence angle	[°]

k	Empirical coefficient for deviation angle	
l	Chord length	[m]
N	Rotational speed	$[\mathrm{min}^{-1}]$
N_s	Dimensional specific speed	$[\mathrm{min}^{-1}, \mathrm{m}^3/\mathrm{min}, \mathrm{m}]$
p	Static pressure	[Pa]
P_{Input}	Input power	[W]
$P_{Input,averaged}$	Averaged input power	[W]
Q	Volumetric flow rate	[L/s] or $[\mathrm{m}^3/s]$
r	Radius	[m]
RMS	Root mean square of theoretical head errors	[m]
t/l	Max thickness in hydrofoil	
T	Torque of rotor	[N·m]
v_a	Axial velocity	[m/s]
v_θ	Swirling velocity	[m/s]
w	Relative velocity or weight in objective function	[m/s] or [-]
x	Position in a chord	[m]
x_f/l	Max camber location in hydrofoil	
y	Normalized discrepancy between theoretical heads evaluated by CFD or ANN and the model	
$y+$	Dimensionless distance from the wall	
y_t	Thickness of blade	[m]
$z_{tip,stack}$	Tip stacking position in axial direction	[m]
Greeks		
β	Flow angle	[°]
β_B	Blade angle	[°]
β_m	Average flow angle	[°]
γ	Blade stagger angle	[°]
δ	Deviation angle	[°]
δ_{m2}/l	Momentum thickness coefficient	
ζ_c	Cascade loss coefficient	
ζ_s	System resistance coefficient	$[\mathrm{s}^2/\mathrm{m}^5]$
η	Efficiency	
θ	Local gradient angle of camber line	[°]
$\theta_{tip,stack}$	Tip stacking position in circumferential direction	[Rad]
ρ	Fluid density	$[\mathrm{kg}/\mathrm{m}^3]$
ξ	Axial velocity change ratio	

σ	Solidity	
$\psi_{loss,other}$	The other loss coefficient	
ω	Angular rotational speed of rotor	[Rad/s]

Subscripts	
1	At rotor inlet
2	At rotor outlet
ANN	Using metamodel ANN
c	At casing
cascade	Using cascade loss model
CFD	Using CFD
d	At design point
f	Front rotor
far	At far downstream of rear rotor
hub	At hub
model	Using model
mix	For mixing loss
Nd	With design rotational speed
original	Original rotors RR3
other	For the other losses
outlet	Outlet boundary of rear rotor domain in CFD
r	Rear rotor
ref	For reference
RSC	With rotational speed control
S2, S3, S4	At section 2, 3 and 4 respectively
t	Total of front and rear rotor
tip	At blade tip

Reference

[1] 一般社団法人　ターボ機械協会，ターボ機械を知ろう : https://www.turbo-so.jp/turbo-kids2.html

[2] De Almeida, A. T., Fonseca, P. and Bertoldi, P., Energy-efficient motor systems in the industrial and in the services sectors in the European Union: characterisation, potentials, barriers and polices, Energy, Vol. 28, No. 7 (2003), pp. 673-690.

[3] 松村　正夫，　國友　新太，ポンプの省エネルギーの動向，エバラ時報，No. 225, pp. 3-6 (2009).

[4] Frenning, L., Pump life cycle costs: a guide to LCC analysis for pumping systems, Hydraulic Institite & Europump (2001).

[5] IEA, World Energy Balances (2019 edition).

[6] Brennen, C. E., Hydrodynamics of Pumps, Concepts ETI and Oxford Science Publications (1994).

[7] Sabersky, R. H., Acosta, A. J. and Hauptmann, E. G., Fluid Flow (3rd edition), Macmillan Publ. Co. (1989)

[8] Stepanoff, A. J., Centrifugal and Axial Flow Pump, John Wiley and Sons, INC (1957).

[9] Shi, L., Zhang, D., Zhao, R. and Shi, W., Visualized observations of trajectory and dynamics of unsteady tip cloud cavitating vortices in axial flow pump, Journal of Fluid Science and Technology, Vol. 12, No. 1 (2017).

[10] 鶴　若菜，液中の気泡核特性を考慮した均質媒体モデルによるキャビテーション流れの数値解析，博士学位論文，九州大学 (2018).

[11] Franz, R., Acosta, A. J., Brennen, C. E. and Caughey, T. K., The rotordynamic forces on a centrifugal pump impeller in the presence of cavitation, ASME Journal of Fluids Engineering, Vol.112, pp. 264-271 (1990).

[12] Morii, T., Tanaka, Y., Watanabe, S., Ohashi, S. and Matsunaga, Y., Suction performance and cavitation instabilities of turbopumps with three different inducer design, International Journal of Fluid Machinery and Systems, Vol. 12, No. 2, pp.128-135 (2019).

[13] Denton, J. D. Entropy generation in turbomachinery flows, Aerospace Technology Conference and Exposition (1990).

[14] Praisner, T. J. and Clark, J. P., Predicting transition in turbomachinery-part I: a review and new model development, ASME Journal of Turbomachinery, Vol.129, pp.1-13 (2007).

[15] Shim, H. S. and Kim, K. Y, Numerical investigation on hydrodynamic characteristics of a centrifugal pump with a double volute at off-design conditions, International Journal of Fluid Machinery and Systems, Vol. 10, No. 3, pp. 218-226 (2017).

[16] Kock, F. and Herwig, H., Local entropy production in turbulent shear flows: a high-Reynolds

number model with wall functions, International Journal of Heat and Mass Transfer, Vol. 47, pp. 2205-2215 (2004).

[17] Schmandt, B. and Herwig, H., Internal flow losses: a fresh look at old concepts, ASME Journal of Fluids Engineering, Vol. 133, 051201 (2011).

[18] Bohle, M., Fleder, A. and Mohr, M., Study of the losses in fluid machinery with the help of entropy, International Symposium on Transport Phenomena and Dynamics of Rotating Machinery, Hawaii, Honolulu (2016).

[19] Gong, R. Z., Wang, H. J., Chen, L. X., Li, D. Y., Zhang, H. C. and Wei, X. Z., Application of entropy production theory to hydro-turbine hydraulic analysis, Science China Technological Sciences, Vol. 56, No. 7, pp. 1636-1643 (2013).

[20] Zhang, D., Tsuneda, T., Katayama, Y., Watanabe, S., Tsuda, S. and Furukawa, A., Loss mechanism in rear rotor of contra-rotating axial flow pump, 14th Asian International Conference on Fluid Machinery, Zhenjiang, China, AICFM-232 (2017).

[21] Hou, H., Zhang, Y., Li, Z., Jiang, T., Zhang, J. and Xu, C., Numerical analysis of entropy production on a LNG cryogenic submerged pump, Journal of Natural Gas Science and Engineering, Vol. 36, pp. 87-96 (2016).

[22] Li, D., Wang, H., Qin, Y., Han, L., Wei, X. and Qin, D., Entropy production analysis of hysteresis characteristic of a pump-turbine model, Energy Conversion and Management, Vol. 149, pp. 175-191 (2017).

[23] 井上　雅弘，鎌田　好久，流体機械の基礎，コロナ社 (1989).

[24] Cai, W., Li, Y., Li, X. and Liu, C., Numerical investigation of fluid flow and performance prediction in a fluid coupling using large eddy simulation, International Journal of Rotating Machinery, Volume 2017, Article ID 3718671 (2017).

[25] Ejiri, E. and Kubo, M., Influence of the core geometry of a flat torque converter on internal flow and loss, JSME International Journal Series B Fluids and Thermal Engineering, Vol. 42, No.3, pp. 467-475 (1999).

[26] Sehra, A. K. and Kerrebrock, J. L., Blade-to-blade flow effects on mean flow in transonic compressors, AIAA Journal, Vol. 19, No. 4, pp. 476-483 (1981).

[27] Lyman, F. A., On the conservation of rothalpy in turbomachines, International Gas Turbine and Aeroengine Congress and Exposition, Cologne, Germany, 92-GT-217 (1992).

[28] 新潟県農地部，用排水機場設備設計の手引 (2015).

[29] Saidur, R., Mekhilef, S., Ali, M.B., Safari, A. and Mohammed, H.A., Applications of variable speed drive (VSD) in electrical motors energy savings, Renewable and Sustainable Energy Reviews, Vol. 16, No. 1, pp. 543-550 (2012).

[30] Wan, H., Daniel, C. and Paul, K., An aging world: 2015, International Population Reports (2016).

[31] 和田　章弘，　内田　幸雄, 高比速度軸流ポンプの性能の改善, とりしまレビュー, Vol. 12, pp. 32-35 (1999).

[32] Kanemoto, T., Komaki, K., Katayama, M. and Fujimura, M., Counter-rotating type pumping unit (impeller speeds in smart control), International Journal of Fluid Machinery and Systems, Vol. 4, No. 3, pp. 334-340 (2011).

[33] Tosin, S., Friedrichs, J. and Dreiss, A., Pumping unit power-density improvement by application of counter-rotating impellers design, ASME Journal of Turbomachinery, Vol. 138, No. 11, 111004 (2016).

[34] Liang, Y. S., Wang, W., Li, H., Shen, X., Xu, Y. and Dai, J., The south-to-north water diversion project: effect of the water diversion pattern on transmission of oncomelania hupensis, Parasites & Vectors, Vol. 5 (2012).

[35] Lan, C., Yi, X., Duan, G. and Wang, L., Study on selection of water pump-unit on the eastern route of south-north water diversion project, Journal of Drainage and Irrigation Machinery Engineering, Vol. 22 pp.1-7 (2004) (in Chinese).

[36] Furukawa, A., Shigemitsu, T. and Watanabe, S., Performance test and flow measurement of contra-rotating axial flow pump, Journal of Thermal Science, Vol. 16, No. 1, pp. 7-13 (2007).

[37] Cao, L. L., High performance design of a contra-rotating axial flow pump with different rotor-speed combination, Doctor Thesis, Kyushu University (2014).

[38] Cao, L. L., Watanabe, S., Momosaki, S., Imanishi, T. and Furukawa, A., Low speed design of rear rotor in contra-rotating axial flow pump, International Journal of Fluid Machinery and Systems, Vol. 6, No. 2, pp. 105-112 (2013).

[39] 重光　亨，古川　明徳，大熊　九州男，渡邉　聡，二重反転形軸流ポンプの後段翼車設計に関する実験的考察，ターボ機械，Vol.31, No.2 (2003).

[40] 百崎　晋平，宇佐見　聡，渡邉　聡，古川　明徳，大熊　九州男，二重反転形軸流ポンプの回転数制御に関する実験的考察，ターボ機械，Vol. 39, No. 2 (2010).

[41] Lieblein, S., Aerodynamic design of axial flow compressors, Chapter 6, NASA SP36 (1965).

[42] Lieblein, S., Loss and stall analysis of compressor cascades, ASME Journal of Basic Engineering, Vol. 81, No. 3, pp. 387-397 (1959).

[43] Lakshminarayana, B., Methods of predicting the tip clearance effects in axial flow turbomachinery, ASME Journal of Basic Engineering, Vol. 92, No. 3, pp. 467-480 (1970).

[44] Oyama, A. and Liou, M. S., Multiobjective optimization of rocket engine pumps using evolutionary algorithm, Journal of Propulsion and Power, Vol. 18, No. 3 (2002).

[45] Wahba, W. and Tourlidakis, A., A genetic algorithm applied to the design of blade profiles for centrifugal pump impellers, 15th AIAA Computational Fluid Dynamics Conference, Anaheim, CA (2001).

[46] Bashiri, M., Derakhshan, S. and Shahrabi, J., Design optimization of a centrifugal pump

using particle swarm optimization algorithm, International Journal of Fluid Machinery and Systems, Vol. 12, No. 4, pp.322-331 (2019).

[47] Li, Z. and Zheng, X., Review of design optimization methods for turbomachinery aerodynamics, Progress in Aerospace Sciences, Vol. 93, pp. 1-23 (2017).

[48] Wang, X. D., Hirsch, C., Kang, S. and Lacor, C., Multi-objective optimization of turbomachinery using improved NSGA-II and approximation model, Computer Methods in Applied Mechanics and Engineering., Vol. 200, pp. 883-895 (2011).

[49] Maral, H., Senel, C. B., Deveci, K., Alpman, E., Kavurmacioglu, L. and Camci, C., A genetic algorithm based multi-objective optimization of squealer tip geometry in axial flow turbines: a constant tip gap approach, ASME Journal of Fluids Engineering, Vol. 142, No. 2 (2020).

[50] Honda, H., Cao, L. L., Watanabe, S., Tsuda, S. and Furukawa, A., Numerical investigation on performance of contra-rotating axial flow pump with different rear rotor design, Proceedings of the ASME/JSME/KSME 2015 Joint Fluids Engineering Conference, Seoul, South Korea, AJKFluids2015-33490 (2015).

[51] Denton, J. D., Some limitations of turbomachinery CFD, Proceedings of ASME Turbo Expo 2010: Power for Land, Sea and Air, Glasgow, UK, GT2010-22540 (2010).

[52] Momosaki, S., Usami, S., Watanabe, S. and Furukawa, A., Numerical simulation of internal flow in a contra-rotating axial flow pump, IOP Conference Series: Earth and Environmental Science, Vol.12, 012046 (2010).

[53] Denton, J. D., The 1993 IGTI scholar lecture: loss mechanism in turbomachines, ASME Journal of Turbomachinery, Vol. 115, pp. 621-656 (1993).

[54] Wilson, R. V., Stern, F., Coleman, H. W. and Paterson, E. G., Comprehensive approach to verification and validation of CFD simulations-part 2: application for RANS simulation of a cargo/container ship, ASME Journal of Fluids Engineering, Vol. 123, No. 4, pp. 803-810 (2001).

[55] Hirano, T., Yoshimura, M., Shimoyama, K. and Komiya, A., Thermo-fluid dynamic design optimization of a concentric tube heat exchanger, Journal of Fluid Science and Technology, Vol. 14, No. 2, Paper No. 19-00302 (2019).

[56] Cao, L. L, Watanabe, S., Imanishi, T., Yoshimura, H. and Furukawa, A., Blade rows interaction in contra-rotating axial flow pump designed with different rotational speed concept, IOP Conference Series: Material Science and Engineering, Vol. 52, 022004 (2013).

[57] Shigemitsu, T., Furukawa, A., Watanabe, S., Okuma, K. and Fukutomi, J., Internal flow measurement with LDV at design point of contra-rotating axial flow pump, Journal of Fluid Science and Technology, Vol. 4, No. 3, pp. 723-734 (2009).

[58] Zhang, D., Tsuneda, T., Katayama, Y., Watanabe, S., Tsuda, S. and Furukawa, A., Backflow vortex behaviors in contra-rotating axial flow pump at low flow rates, IOP Conference

Series: Earth and Environmental Science, Vol. 163, 012036 (2018).

[59] 生井　武文，井上　雅弘，ターボ送風機と圧縮機，コロナ社（1988).

[60] Zhang, D., Katayama, Y., Watanabe, S., Tsuda, S. and Furukawa, A., Numerical study on loss mechanism in rear rotor of contra-rotating axial flow pump, International Journal of Fluid Machinery and Systems, Vol. 13. No. 1, pp. 241-252 (2020).

[61] ターボ機械協会，ターボポンプ，日本工業出版（1991).

[62] Zhang, D., Katayama, Y., Watanabe, S., Tsuda, S. and Furukawa, A., Performance prediction model of contra-rotating axial flow pump with separate rotational speed of front and rear rotors and its application for energy saving operation, JSME Journal of Fluid Science and Technology, Vol. 15, No. 3 (2020).

[63] Menter, F., Zonal two equation kw turbulence models for aerodynamic flows, 23rd Fluid Dynamics, Plasmadynamics, and Lasers Conference (1993).

[64] Denton, J. D. and Xu, L., The exploitation of three-dimensional flow in turbomachinery design, Proceedings of the Institution of Mechanical Engineers, Part C: Journal of Mechanical Engineering Science. Vol. 213, No. 2, pp. 125-137 (1998).

[65] Wang, D. X., He, L., Li, Y. S. and Wells, R. G., Adjoint aerodynamic design optimization for blades in multistage turbomachines-part II: validation and application, ASME Journal of Turbomachinery, Vol. 132, No. 2: 021012 (2010).

[66] Sacks, J., Welch, W. J. Mitchell, T. J. and Wynn, H. P., Design and analysis of computer experiments, Statistical Science, Vol. 4, No. 4, pp. 409-423 (1989).

[67] Guo, J., Zhang, Y., Chen, Z. and Feng, Y., CFD-based multi-objective optimization of a waterjet-propelled trimaran, Ocean Engineering, Vol. 195, 106755 (2020).

[68] Kim, J. H., Kim, J. W. and Kim, K. Y., Axial-flow ventilation fan design through multi-objective optimization to enhance aerodynamic performance, ASME Journal of Fluids Engineering, Vol. 133, 101101 (2011).

[69] Tun, M. T. and Sakaguchi, D., Multi-point optimization of recirculation flow type casing treatment in centrifugal compressors, Turbo Expo: Power for Land, Sea, and Air, Vol. 49729 (2016).

[70] Demeulenaere, A., Ligout, A. and Hirsch, C., Application of multipoint optimization to the design of turbomachinery blades, Turbo Expo: Power for Land, Sea, and Air, Vol. 41707, pp. 1481-1489 (2004).

[71] Marquardt, D. W., An algorithm for least-squares estimation of nonlinear parameters, Journal of the society for Industrial and Applied Mathematics, Vol. 11, No. 2, pp. 431-441 (1963).

[72] Panchal, G., Ganatra, A., Kosta, Y. P. and Panchal, D., Behaviour analysis of multilayer perceptrons with multiple hidden neurons and hidden layers, International Journal of Computer Theory and Engineering, Vol. 3, No. 2, pp. 332-337 (2011).

[73] Praisner, T. J., Clark, J. P., Nash, T. C., Rice, M. J. and Grover, E. A., Performance impacts due to wake mixing in axial-flow turbomachinery, Proceedings of the ASME Turbo Expo 2006: Power for Land, Sea, and Air, Vol. : Turbomachinery, Parts A and B (2006).

[74] Gu, Y., Pei, J., Yuan, S., Zhang, J. and Wang, W., Multi-objective optimization of centrifugal pump impeller based on kriging model and multi-island genetic algorithm, 16th International Symposium on Transport Phenomenon and Dynamics of Rotating Machinery, hal-01887483 (2016).

[75] Chiba, K., Data mining for multidisciplinary design space of regional-jet wing, Journal of Aerospace Computing, Information, and Communication, Vol. 4, No. 11 (2007).

[76] Jeong, S., Chiba, K. and Obayashi, S., Data mining for aerodynamic design space, Journal of Aerospace Computing, Information, and Communication, Vol. 2, pp.452-469 (2005).

[77] MathWorks, Statistics and Machine Learning Toolbox: User's Guide (R2018a).

[78] Deb, K. An efficient constraint handling method for genetic algorithms, Computer Methods in Applied Mechanics and Engineering, Vol. 186, No. 2-4, pp. 311-338 (2000).

[79] MathWorks, Global Optimization Toolbox: User's Guide (R2020b), Retrieved from https://jp.mathworks.com/help/pdf_doc/gads/gads.pdf.

Appendix

Note: number of digits after decimal point is reduced in the following tables.

Design parameters in DOE for ANN training of rear rotor (Part 1)

No.	$\beta_{B1,hub}$	$\beta_{B1,S2}$	$\beta_{B1,S3}$	$\beta_{B1,S4}$	$\beta_{B1,tip}$	σ_{hub}	σ_{tip}	$z_{tip,stack}$	$\theta_{tip,stack}$
1	68.12	67.68	74.63	71.13	79.32	1.085	0.731	0.0095	0.065
2	70.02	69.89	69.59	75.30	82.98	1.198	0.817	-0.0016	-0.478
3	70.67	74.22	74.92	74.10	78.46	0.809	0.512	0.0050	-0.132
4	68.49	68.13	74.28	76.12	80.89	0.842	0.532	0.0097	-0.004
5	66.34	73.33	73.01	73.49	79.07	0.830	0.839	-0.0025	0.462
6	70.11	71.21	70.79	76.64	83.45	0.752	0.862	0.0007	-0.318
7	68.57	74.12	71.95	75.94	76.26	0.811	0.664	0.0052	0.117
8	73.24	70.14	71.92	76.15	81.56	1.004	0.554	-0.0014	-0.310
9	71.08	70.56	73.15	71.04	76.30	1.181	0.653	0.0082	-0.071
10	67.78	73.19	71.18	70.82	83.79	0.702	0.736	0.0044	0.217
11	73.43	72.87	72.10	76.50	76.68	0.881	0.814	-0.0024	-0.170
12	72.98	67.22	69.98	75.70	78.56	0.976	0.711	0.0049	0.389
13	67.73	73.28	68.85	75.66	81.25	0.883	0.989	-0.0026	0.028
14	71.91	72.60	75.53	69.68	78.00	0.951	0.826	-0.0018	-0.099
15	69.58	68.73	68.37	76.05	77.78	1.178	0.672	0.0058	0.117
16	69.82	67.22	73.48	71.51	81.76	0.765	0.972	0.0067	-0.149
17	69.97	67.83	73.03	75.62	83.40	0.870	0.907	-0.0009	-0.406
18	65.64	73.27	73.72	71.73	77.68	0.993	0.707	0.0090	0.023
19	68.72	68.00	70.32	74.64	76.92	1.199	0.772	0.0051	0.320
20	69.51	74.87	73.45	72.26	82.25	0.750	0.604	0.0082	-0.085
21	66.48	74.22	71.03	75.70	80.97	0.842	0.935	0.0030	-0.299
22	71.91	68.22	70.27	70.39	80.41	0.986	0.695	0.0050	0.481
23	68.34	73.65	73.25	72.02	82.26	1.155	0.545	-0.0031	0.010
24	72.37	74.41	69.71	72.33	76.47	1.075	0.800	0.0027	-0.116
25	67.60	74.38	73.38	72.82	81.57	0.706	0.729	0.0067	-0.361
26	70.95	74.00	69.68	73.65	78.76	1.101	0.516	0.0058	-0.138
27	71.24	74.34	73.57	72.89	82.92	0.940	0.589	-0.0043	-0.235
28	69.70	73.24	69.60	69.84	78.56	1.152	0.710	0.0065	0.157
29	69.05	67.06	72.79	71.27	83.48	0.976	0.883	-0.0003	0.286
30	68.70	74.85	71.98	75.05	81.07	1.120	0.521	-0.0021	-0.245
31	66.54	69.40	68.64	73.54	82.72	0.867	0.867	0.0046	0.449
32	66.42	68.34	74.72	75.62	83.52	0.942	0.787	0.0008	-0.209

33	71.30	70.79	71.39	76.13	77.61	0.860	0.980	0.0036	-0.489
34	67.99	67.75	76.28	76.03	80.67	1.047	0.557	0.0008	-0.006
35	71.27	70.46	70.17	76.76	79.22	0.715	0.825	0.0099	-0.337
36	67.37	69.10	69.01	76.36	81.81	0.975	0.675	0.0049	0.429
37	71.40	67.26	71.08	74.84	77.77	1.137	0.732	0.0088	-0.266
38	68.15	73.62	68.64	70.92	83.91	0.934	0.701	0.0050	0.144
39	71.16	71.46	72.34	70.84	82.57	0.909	0.625	0.0085	-0.499
40	65.73	69.10	73.64	77.66	80.53	1.045	0.914	-0.0029	-0.081
41	71.84	70.33	68.64	71.43	80.67	0.922	0.979	-0.0015	0.323
42	67.55	73.56	76.26	71.04	81.22	0.705	0.728	0.0056	-0.083
43	69.87	69.06	75.96	75.22	82.93	1.019	0.703	-0.0049	-0.319
44	68.76	69.33	73.17	73.93	83.91	0.726	0.861	-0.0025	0.288
45	71.20	70.52	69.37	71.94	79.52	0.752	0.984	0.0076	0.116

Design parameters in DOE for ANN training of rear rotor (Part 2)

No.	$\beta_{B1,hub}$	$\beta_{B1,S2}$	$\beta_{B1,S3}$	$\beta_{B1,S4}$	$\beta_{B1,tip}$	σ_{hub}	σ_{tip}	$z_{tip,stack}$	$\theta_{tip,stack}$
1	72.05	71.43	69.44	72.86	78.30	1.053	0.771	0.0092	-0.423
2	69.56	71.37	71.49	70.53	83.34	1.093	0.647	-0.0021	0.190
3	68.73	68.16	72.15	72.25	82.51	1.148	0.550	0.0036	0.177
4	68.29	74.41	71.29	70.22	77.37	1.102	0.801	0.0056	0.025
5	71.99	68.28	72.19	71.60	81.26	1.178	0.691	0.0059	-0.399
6	66.75	74.85	70.59	76.75	78.86	1.004	0.505	0.0060	-0.043
7	72.51	68.74	71.07	71.09	83.61	0.946	0.506	0.0063	0.166
8	67.51	72.89	75.20	70.88	80.34	0.876	0.506	0.0034	0.457
9	65.81	74.74	74.87	73.49	77.87	0.837	0.784	0.0062	-0.082

Design parameters for ANN validation in rear rotor

No.	$\beta_{B1,hub}$	$\beta_{B1,S2}$	$\beta_{B1,S3}$	$\beta_{B1,S4}$	$\beta_{B1,tip}$	σ_{hub}	σ_{tip}	$z_{tip,stack}$	$\theta_{tip,stack}$
1	70.85	68.19	73.80	76.51	78.14	1.176	0.525	0.0017	-0.132
2	69.21	70.35	69.29	70.51	81.39	1.109	0.868	-0.0005	0.412
3	68.92	67.23	72.34	72.08	81.65	1.168	0.607	0.0079	0.148
4	66.91	69.37	75.87	72.58	82.43	1.047	0.551	0.0034	-0.053
5	73.09	72.25	75.13	70.65	78.84	0.729	0.825	0.0028	-0.075
6	68.66	68.96	75.11	77.62	80.57	0.752	0.885	0.0050	-0.386
7	72.98	67.99	75.39	72.23	81.27	0.873	0.724	-0.0050	0.239
8	66.26	69.38	72.09	72.59	82.22	1.176	0.942	0.0039	-0.365
9	65.75	67.96	73.26	75.58	80.57	1.099	0.994	0.0000	-0.086

Design parameters in DOE for ANN training of front rotor (Part 1)

No.	$\beta_{B1,hub}$	$\beta_{B1,S2}$	$\beta_{B1,S3}$	$\beta_{B1,S4}$	$\beta_{B1,tip}$	σ_{hub}	σ_{tip}	$z_{tip,stack}$	$\theta_{tip,stack}$
1	66.31	76.01	76.24	82.83	88.10	1.097	0.576	0.0002	-0.014
2	66.24	74.41	82.35	84.48	84.08	1.011	0.610	-0.0046	0.144
3	60.22	71.79	81.75	83.04	87.18	1.025	0.756	0.0034	0.187
4	62.86	76.23	78.45	87.55	89.31	1.057	0.536	-0.0007	-0.085
5	60.22	71.80	76.43	85.32	89.19	1.273	0.674	0.0035	0.005
6	59.82	71.57	79.51	85.08	85.98	1.235	0.563	0.0044	0.207
7	62.17	74.37	77.38	80.51	87.53	1.279	0.809	0.0035	-0.157
8	63.14	70.32	78.51	86.29	89.20	1.107	0.533	-0.0006	0.284
9	60.11	73.65	76.29	86.94	89.03	1.188	0.633	-0.0036	0.274
10	65.36	71.89	78.52	87.20	87.23	1.224	0.761	-0.0079	-0.272
11	62.89	70.75	78.27	87.93	83.44	1.231	0.648	-0.0008	0.170
12	61.14	70.10	81.41	83.33	86.90	1.262	0.577	0.0034	0.054
13	65.14	72.75	76.75	80.52	89.45	1.076	0.721	0.0037	0.054
14	65.34	73.34	83.24	83.52	84.71	1.222	0.525	0.0011	-0.119
15	63.89	76.36	81.19	83.67	84.37	1.146	0.860	-0.0061	-0.238
16	61.67	76.24	80.41	85.87	84.38	1.010	0.698	-0.0053	0.261
17	66.86	69.90	80.66	81.43	85.93	1.146	0.812	0.0004	-0.113
18	66.97	75.46	79.73	86.61	85.46	1.043	0.727	-0.0088	-0.052
19	61.56	75.16	80.40	84.24	90.42	1.284	0.653	-0.0100	-0.213
20	61.69	76.44	80.34	86.23	91.01	1.082	0.572	-0.0022	-0.286
21	66.73	75.98	78.06	81.58	86.82	1.201	0.808	-0.0038	-0.245
22	62.06	70.12	83.36	84.75	86.72	1.038	0.808	0.0018	-0.165
23	59.35	75.67	80.84	81.93	87.56	1.243	0.582	0.0045	-0.045
24	62.03	71.49	81.71	84.46	83.97	1.299	0.763	0.0050	-0.232
25	66.35	71.41	81.99	80.84	88.22	1.266	0.635	-0.0083	0.010
26	59.63	76.35	78.69	85.64	88.29	1.168	0.898	-0.0078	-0.152
27	65.34	73.16	81.64	82.42	88.40	1.308	0.584	-0.0033	-0.252
28	59.94	74.14	81.68	82.85	83.41	1.277	0.703	0.0034	-0.155
29	65.21	70.17	79.82	81.32	86.42	1.323	0.838	-0.0052	0.036
30	62.24	73.11	83.76	85.02	84.83	1.289	0.769	-0.0098	-0.112
31	62.08	73.59	80.33	82.65	90.42	1.294	0.557	0.0013	-0.247
32	65.03	71.21	80.79	81.27	90.19	1.175	0.639	-0.0091	0.300
33	64.81	76.68	79.47	80.68	88.24	1.035	0.614	0.0025	-0.046

34	66.87	71.27	81.14	85.05	84.16	1.147	0.816	-0.0097	-0.079
35	60.63	70.09	78.97	87.15	88.21	1.224	0.619	-0.0026	0.259
36	60.87	69.95	82.30	87.88	84.84	1.199	0.647	0.0012	-0.005
37	59.61	75.80	83.48	83.88	86.11	1.030	0.624	-0.0010	0.161
38	61.18	75.77	76.65	87.77	84.27	1.112	0.789	-0.0033	0.071
39	62.32	74.32	77.43	84.36	90.88	1.077	0.828	0.0001	-0.285
40	61.16	72.57	81.77	83.84	88.37	1.025	0.556	0.0027	0.261
41	64.07	76.78	82.59	80.31	84.01	1.259	0.613	-0.0018	-0.082
42	65.30	70.22	79.78	81.35	85.18	1.251	0.873	-0.0037	0.056
43	59.27	70.78	80.10	85.02	85.26	1.133	0.819	0.0015	0.283
44	64.39	70.61	76.02	83.78	86.63	1.285	0.868	-0.0052	0.058
45	59.67	75.77	78.61	82.32	84.55	1.303	0.766	0.0010	0.001

Design parameters in DOE for ANN training of front rotor (Part 2)

No.	$\beta_{B1,hub}$	$\beta_{B1,S2}$	$\beta_{B1,S3}$	$\beta_{B1,S4}$	$\beta_{B1,tip}$	σ_{hub}	σ_{tip}	$z_{tip,stack}$	$\theta_{tip,stack}$
1	63.42	73.92	76.93	82.29	89.72	1.331	0.791	-0.0099	-0.070
2	62.09	77.20	76.25	81.28	85.18	1.247	0.839	-0.0016	0.031
3	62.66	71.26	82.20	81.75	89.11	1.016	0.648	-0.0002	0.252
4	59.79	76.83	82.47	83.81	85.15	1.110	0.549	-0.0006	0.120
5	65.05	73.83	78.69	81.39	88.03	1.071	0.517	0.0040	0.176
6	63.62	76.01	81.86	81.62	85.89	1.183	0.612	0.0047	-0.299
7	61.03	69.85	78.94	86.23	86.96	1.338	0.763	-0.0075	0.227
8	66.27	73.13	76.05	81.70	86.09	1.203	0.590	0.0006	0.180
9	61.26	70.80	79.51	85.32	89.22	1.294	0.527	-0.0047	0.246

Design parameters for ANN validation in front rotor

No.	$\beta_{B1,hub}$	$\beta_{B1,S2}$	$\beta_{B1,S3}$	$\beta_{B1,S4}$	$\beta_{B1,tip}$	σ_{hub}	σ_{tip}	$z_{tip,stack}$	$\theta_{tip,stack}$
1	64.46	70.32	79.74	80.06	85.29	1.203	0.885	0.0026	-0.066
2	63.38	71.29	82.85	87.67	88.61	1.052	0.651	-0.0097	0.041
3	63.51	77.24	79.13	83.71	83.48	1.282	0.606	-0.0080	0.131
4	65.93	77.01	78.09	84.53	87.01	1.002	0.646	-0.0072	0.132
5	59.39	77.27	81.52	81.22	85.41	1.191	0.823	-0.0023	-0.064
6	60.43	73.17	81.37	87.68	89.61	0.992	0.732	-0.0045	-0.107
7	59.54	76.88	78.06	81.79	86.47	1.152	0.810	0.0019	0.095
8	61.07	73.41	80.94	87.55	89.23	1.119	0.829	-0.0068	-0.237
9	60.64	73.84	81.64	84.65	83.46	1.281	0.595	-0.0035	0.239